Coulomb Dissociation of ^{31}Cl and ^{32}Ar - constraining the rp process

Dissertation

zur Erlangung des Doktorgrades

der Naturwissenschaften

vorgelegt beim Fachbereich Physik

der Johann Wolfgang Goethe-Universität

in Frankfurt am Main

von

Christoph Langer

aus Darmstadt (Germany)

Frankfurt am Main 2012

(D 30)

vom Fachbereich Physik der

Johann Wolfgang Goethe-Universität als Dissertation angenommen.

Dekan: Prof. Dr. Michael Huth

Gutachter: Prof. Dr. René Reifarth
Prof. Dr. Thomas Aumann

Tag der Disputation: 02. Mai 2012

A B S T R A C T

The subject of this thesis aimed at a better understanding of the spectacular X-ray burst. The most likely astrophysical site is a very dense neutron star, which accretes H/He-rich matter from a close companion. While falling towards the neutron star, the matter is heated up and a thermonuclear runaway is ignited. The exact description of this process is dominated by the properties of a few proton-rich radioactive isotopes, which have a low interaction probability, hence a high abundance.

The topic of this thesis was therefore an investigation of the short-lived, proton-rich isotopes ^{31}Cl and ^{32}Ar. The Coulomb dissociation method is the modern technique of choice. Excitations with energies up to 20 MeV can be induced by the Lorentz contracted Coulomb field of a lead target. At the GSI Helmholtzzentrum für Schwerionenforschung GmbH in Darmstadt, Germany, a ^{36}Ar beam was accelerated to an energy of 825 AMeV and fragmented in a beryllium target. The fragment separator was used to select the desired isotopes with a remaining energy of 650 AMeV. They were subsequently directed onto a ^{208}Pb target in the ALAND/LAND setup. The measurement was performed in inverse kinematics. All reaction products were detected and inclusive and exclusive measurements of the respective Coulomb dissociation cross sections were possible.

During the analysis of the experiment, it was possible to extract the energy-differential excitation spectrum of ^{31}Cl, and to constrain astrophysically important parameters for the time-reversed ^{30}S(p,γ)^{31}Cl reaction. A single resonance at 0.443(37) MeV dominates the stellar reaction rate, which was also deduced and compared to previous calculations. The integrated Coulomb dissociation cross section of this resonance was determined to 15(6) mb. The astrophysically important one- and two-proton emission channels were analyzed for ^{32}Ar and energy-differential excitation spectra could be derived. The integrated Coulomb dissociation cross section for two proton emission were determined with two different techniques. The inclusive measurement yields a cross section of 214(29$^{\text{stat}}$)(20$^{\text{sys}}$) mb, whereas the exclusive reconstruction results in a cross section of 226(14$^{\text{stat}}$)(23$^{\text{sys}}$) mb. Both results are in very good agreement. The Coulomb dissociation cross section for the one-proton emission channel is extracted solely from the exclusive measurement and is 54(8$^{\text{stat}}$)(6$^{\text{sys}}$) mb.

Furthermore, the development of the Low Energy Neutron detector Array (LENA) for the upcoming R^{3}B setup is described. The detector will be utilized in charge-exchange reactions to detect the low-energy recoil neutrons from (p,n)-type reactions. These reaction studies are of particular importance in the astrophysical context and can be used to constrain half lifes under stellar conditions. In the frame of this work, prototypes of the detector were built and successfully commissioned in several international laboratories. The analysis was supported by detailed simulations of the detection characteristics.

ZUSAMMENFASSUNG

Das Ziel dieser Arbeit war das bessere Verständnis einer Klasse spektakulärer stellarer Ereignisse, den sogenannten Röntgenausbrüchen. Diese geschehen vermutlich, wenn auf der Oberfläche eines Neutronensterns die von einem Begleitstern zugeflossene Masse in einer thermonuklearen Explosion zu schwereren Elementen synthetisiert wird. Der genaue Verlauf dieses Prozesses wird durch radioaktive Isotope bestimmt, die aufgrund ihrer kernphysikalischen Eigenschaften während der Explosion eine geringe Wechselwirkungswahrscheinlichkeit haben und sich deshalb stark anhäufen.

Der Gegenstand der vorliegenden Arbeit war deshalb die Untersuchung der kurzlebigen, protonenreichen Kerne ^{31}Cl und ^{32}Ar. Die heutige Methode der Wahl ist die Coulombaufbruchmethode. Am GSI Helmholtzzentrum für Schwerionenforschung GmbH wurde deshalb zunächst ^{36}Ar auf etwa 825 AMeV beschleunigt und in einer Berylliumfolie fragmentiert. Aus der Vielfalt von produzierten radioaktiven Isotopen wurden dann mithilfe des Fragmentseparators FRS die gewünschten exotischen ^{31}Cl und ^{32}Ar Kerne ausgewählt und schließlich die Wechselwirkung mit einem ^{208}Pb-Target am ALADIN/LAND Aufbau bei einer verbleibenden Strahlenergie von etwa 650 AMeV untersucht. Der experimentelle Aufbau ermöglicht den vollständigen Nachweis aller Reaktionsprodukte und somit die inklusive wie exklusive Messung der beteiligten Reaktionsquerschnitte als Funktion der Anregungsenergie im Coulombfeld der Bleikerne.

Im Rahmen der Experimentanalyse der Reaktionen des ^{31}Cl konnte nicht nur der wichtige ^{31}Cl$(\gamma,p)^{30}$S-Querschnitt als Funktion der Energie bestimmt werden, sondern auch die Parameter einer astrophysikalisch äußerst wichtigen Resonanz bei 0.443(37) MeV in der umgekehrten Richtung, ^{30}S$(p,\gamma)^{31}$Cl, genauer festgelegt werden. Der integrale Coulombaufbruchquerschnitt für den ersten angeregten Zustand von ^{31}Cl wurde zu 15(6) mb bestimmt. Zudem konnte die stellare Reaktionsrate extrahiert und mit vorherigen Berechnungen verglichen werden.
Bei der Coulombwechselwirkung von ^{32}Ar können ein oder zwei Protonen emittiert werden. Dieser, aus astrophysikalischer Sicht wichtige Unterschied, wurde in der vorliegenden Arbeit genau untersucht. Es konnten die energieabhängigen Querschnitte der Reaktionen ^{32}Ar(γ,p) und ^{32}Ar$(\gamma,2p)$ abgeleitet werden. Der integrale Coulombaufbruchquerschnitt von ^{32}Ar unter Emission von zwei Protonen wurde mithilfe zwei unterschiedlicher Methoden extrahiert. Die inklusive Messung ergibt dabei einen Querschnitt von 214(29$^{\text{stat}}$)(20$^{\text{sys}}$) mb. Durch die exklusive Messung wurde ein Querschnitt von 226(14$^{\text{stat}}$)(23$^{\text{sys}}$) mb bestimmt. Beide Methoden zeigen gute Übereinstimmung. Im Fall nur eines emittierten Protons wurde ausschließlich die exklusive Methode angewendet und ein Wirkungsquerschnitt von 54(8$^{\text{stat}}$)(6$^{\text{sys}}$) mb extrahiert.

Des Weiteren wird die Entwicklung eines Neutronendektorsystems (LENA) beschrieben, das eine wichtige Rolle in zukünftigen Messungen am R^{3}B-Aufbau spielt. LENA ist für die Detektion von Neutronen im Energiebereich von etwa 50 keV bis zu einigen

MeV optimiert und ist essenziell für die Untersuchung von Ladungstransferreaktionen des Typs (p,n) mit radioaktiven Kernen in umgekehrter Kinematik. Diese Messungen erlauben z.B. die Untersuchung von Halbwertszeiten unter stellaren Bedingungen. Im Rahmen dieser Arbeit wurden Prototypen dieses Detektors gebaut, in verschiedenen internationalen Laboratorien systematisch untersucht und, begleitet von detaillierten Simulationen, charakterisiert.

Contents

1
Motivation

Trying to understand the surrounding environment, and developing theories and models, which are able to reproduce and predict observations, are a fundamental part of the human nature. Especially the evolution of the elements is of highest interest, and is also connected to our existence. The understanding of the basic mechanisms, which form the elements heavier than hydrogen and helium, is strongly related to the modeling of the structure of an atomic nucleus. In order to verify and constrain nuclear models, it is necessary to explore even the most exotic nuclei in the nuclear landscape with modern accelerators, using different reaction types and a variety of experimental setups.

The scope of this thesis is to describe an experimental investigation of the proton-rich isotopes ^{32}Ar and ^{31}Cl, which are important for the astrophysical rapid proton-capture process (rp process). Therefore, the basic motivation and the experimental method is presented in this chapter. It is followed in chapter 2 with a description of the ALADIN/LAND setup. Chapter 3 comprises an instrumentation part, focused on the first measurements and simulations of the Low Energy Neutron detector Array (LENA), which will be used in (p,n)-type reactions in upcoming R^{3}B experiments[1]. The analysis of the performed experiment is described and discussed in chapter 4, and the results are presented in chapter 5. A summary and outlook is given in chapter 6.

1.1 The rapid proton-capture process

The observation of the X-ray sky reveals hundreds of sources with a constant flux of X-rays. Some of them show an additional feature in the observed X-ray spectrum. These are called X-ray bursters. On top of their continuously emitted X-rays, they show bright peaks on a regular or irregular basis. These break-outs usually have a duration of 10 - 100 seconds, and their frequency of occurrence can be in the order of hours up to a few days.

The stellar site of the bright X-ray bursts are neutron stars, which assemble matter from a close companion star, see Fig. 1.1. Here, high temperatures (several 10^9 K) and high densities (up to 10^6 g/cm^3) are reached. The hydrogen-rich and helium-rich matter is accreted onto the surface of the neutron star.

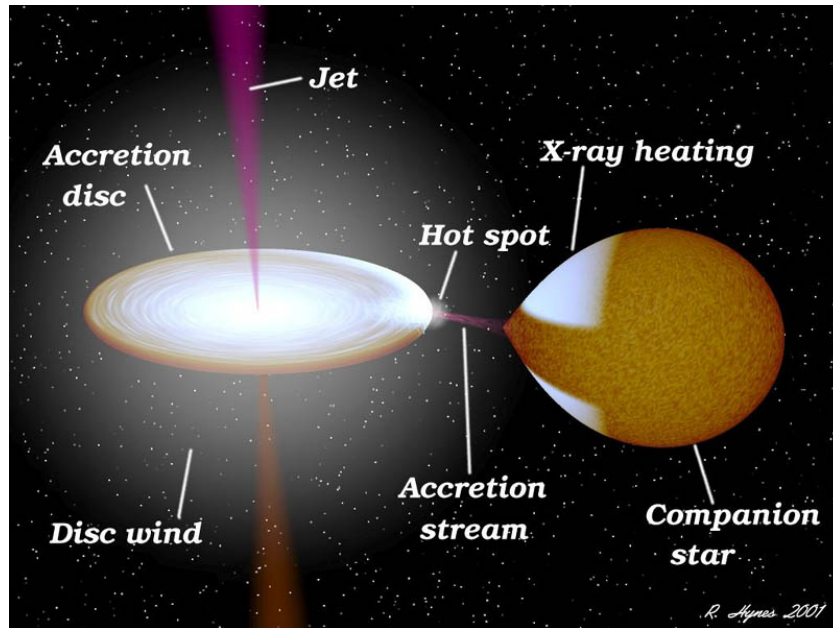[1]Reactions with Relativistic Radioactive Beams

Figure 1.1: An illustrative sketch of a X-ray binary system, consisting of a dense, fast rotating neutron star, and a companion star. Due to the high gravitational forces on the surface of the neutron star, it accretes H/He-rich matter from the companion star. The matter heats up and ignites a thermonuclear runaway, which can be observed as a peak in the X-ray luminosity spectrum with space based telescopes. The figure is taken from [1].

While falling towards the neutron star, gravitational energy is released and can be detected as the persistent X-ray flux. However, the constantly accreting neutron star forms a layer of H/He-rich material, which is heated up to temperatures of 10^8 K. In this scenario, the layer becomes thermonuclear instable. As the temperature still increases, nuclear reactions occur, which in turn increase the temperature even more. This leads to a dramatic situation and results in a thermonuclear runaway. In the full layer, nuclear fusion reactions are ignited in a short moment and they result in a thermonuclear explosion. This powers a peak in the X-ray spectrum, which are in turn produced by the optically thick layer of the neutron star material under extreme density, gravitational, and temperature conditions.

Depending on the depth of the ignition, the duration of the burst, and the burst profile, the dominant source of energy can be identified. If the burst lasts for around 100 s, the main mechanism is the burning of accreted hydrogen and helium in the rapid proton-capture process (rp process), whereas very short bursts might occur from pure helium burning. Under the chaotic conditions in a neutron star, the burst time is mainly dominated by the weak interaction and their long β^+-decay time scales of up to a few seconds,

since capture reactions proceed very fast.

The rp process consists of a sequence of proton and α-particle captures, and subsequent β^+-decays. Possible reaction types are (p,γ), (α,γ), and (α,p). Modeling the energy generation during the rp process is an important task involving many different details. For X-ray bursts, the aim is to model the time structure of the luminosity (i.e. the light curve), and to compare the result directly with the observation.

In order to simulate the X-ray burst, a detailed network of all involved reactions is required. Ignition conditions influence the light curve and are therefore crucial ingredients for the network calculations. Moreover, reaction rates, masses, and β^+-decay times have dominant impact on the final reaction sequence, and they need to be known as precise as possible. Besides the understanding of the reaction network, the nuclear data input also influences the hydrodynamical model of the neutron star, like mixing of ashes, crust temperatures, and the composition of the accreted material. Interestingly, the models developed so far predict, that no, or at least only very little, amount of the produced ashes is ejected into the interstellar medium. This means, that elements, produced during the rp process, are not reflected in the observed elemental or isotopic abundance distributions. Still, this is an unsolved question, which depends very much on the convection and transport models, used in the simulation of an X-ray burst.

The rp process usually ignites with the triple-α process, proceeds via ^{12}C(p,γ)^{13}N to heavier elements up to scandium with α captures in the αp process. Simultaneously, (α,p) reactions occur, in which the protons serve as a catalyst. However, the limit for α captures is set by the strongly increasing Coulomb barrier, when fusioning towards heavier elements. During the αp process, the seed nuclei for the rp process are produced. Once the αp process is stopped, the rp process proceeds via fast (p,γ) reactions, and subsequently decays back to the line of stability via β^+-decay. Usually, the proton-capture rates are in the order of milliseconds, and thus, very fast compared to other reactions. Fig. 1.2 shows an rp-process network calculation for a certain density and temperature profile.

The rp process ends in a closed Sn-Sb-Te cycle, which was shown in earlier one-zone models by Schatz et al., cf [3], [4]. There, (γ, α) reactions dominate the cycle and block the way towards heavier isotopes. Newer one-zone and multi-zone calculations also predict the closed Sn-Sb-Te cycle, but, depending on the model, it is not always reached, because the ashes from previous rp processes influence the reaction path.

However, nuclear physics input is essential to develop a good and accurate model. Of special interest are the waiting points along the rp-process path. The properties of those nuclei have great impact on the light curve and determine, for example, the shape of the decaying tail of the light curve. Even double peak structures in the observed light curves could emerge from waiting points [5].

A waiting point is defined as a nucleus on the path of the rp process, at which the proton-capture flow is hindered to proceed, and where alternative reactions are still slower. At these points, mass abundances are assembled and they directly influence the final abundance distributions. However, certain conditions have to be fulfilled to define
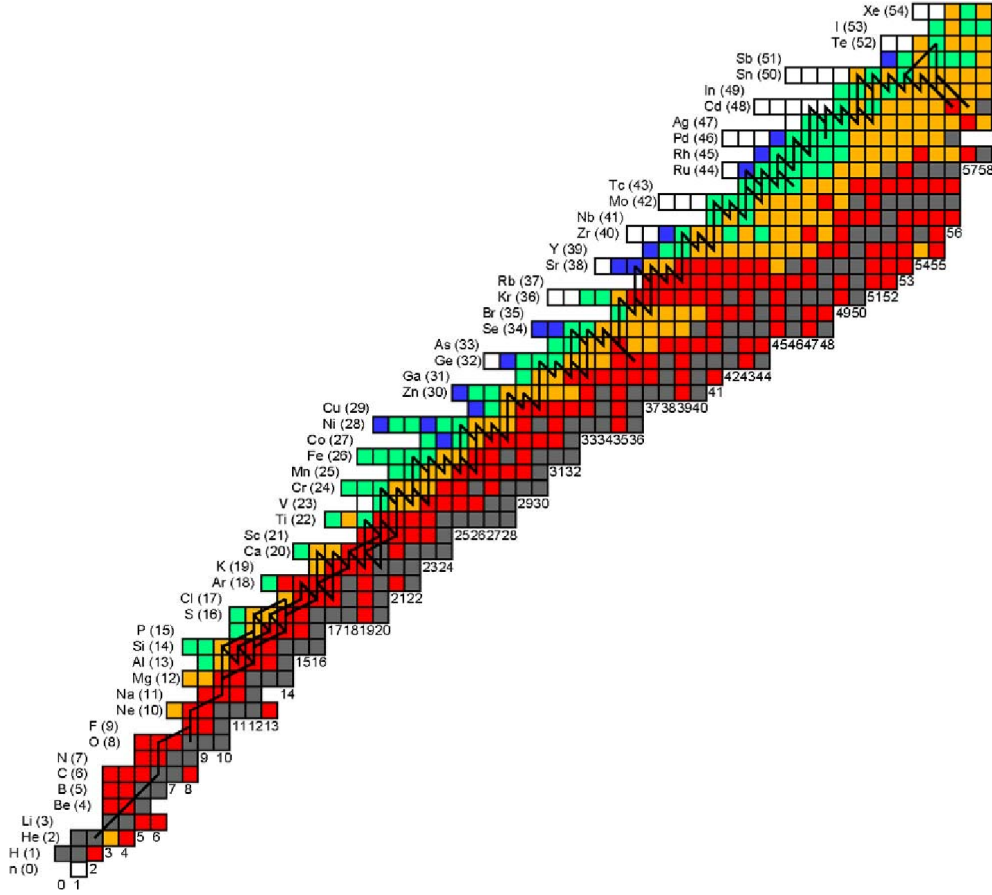
Figure 1.2: A full rp-process network calculation within an one-zone X-ray burst model. The color code indicates different known and unknown masses, stable and unstable nuclei. The closed Sn-Sb-Te cycle is visible. Figure is taken from [2].

a waiting point. Typically, the proton-capture reaction rate is slow compared to the one of neighboring isotopes and isotones. Usually, a low one-proton emission Q-value is the main reason for a slow reaction rate. In a few cases, the next isotone is unbound, which cancels a possible one-proton capture (like in the case of ^{15}O). Moreover, the β^+-decay half life can be in the range of seconds, and thus, it also can not precede the proton capture. In the low-mass region (below the scandium isotopes with $Z = 21$), the αp process is still active and could also circumvent the waiting point via (α, γ) or (α, p) reactions. However, these rates are very dependent on the Coulomb barrier, which steeply increases while proceeding towards heavier isotopes.

The most important heavy waiting points are the $N = Z$ isotopes, like ^{56}Ni, ^{64}Ge, ^{68}Se, ^{72}Kr, up to ^{92}Ru, ^{96}Pd, and ^{100}Sn, see for example [6]. The isotopes have even (Z, N)

and are usually referred to as $\alpha-$nuclei.

In the low-mass region of the reaction flow, important waiting point nuclei are ^{22}Mg, ^{26}Si, ^{30}S, and ^{34}Ar, see [5]. Especially here, statistical Hauser-Feshbach calculations might be misleading, since already single resonances contribute significantly to the stellar reaction rates, and the statistical model, which averages over a series of close resonances, is not applicable anymore.

1.2 The waiting point ^{30}S

Of special interest is the low-mass region of the rp-process flow. Here, the αp process is still active, and could circumvent possible waiting points.

In the explosive environment of an X-ray burst, the reaction flow is believed to pass through ^{30}S towards heavier isotopes, see Fig. 1.3. The reaction ^{30}S(p,γ)^{31}Cl is therefore an important part of the rp process. Moreover, the ^{30}S isotope was identified as a possible waiting point for the following reasons. First, the reaction Q-value for one-proton capture is very low. The tabulated Q-value is 293(50) keV [7]. This results in an abundance equilibrium of proton dissociation and proton capture between ^{30}S and ^{31}Cl at high temperatures. Second, the β^+-decay half lives of ^{31}Cl and ^{30}S are long compared to the typical capture times. The terrestrial half life of ^{30}S is $t_{1/2}$=1.178(5) s, whereas ^{31}Cl has a half life of $t_{1/2}$=150(25) ms, which scales already with the usual burst times. Third, as mentioned above, the αp process is still active. An α capture would supposedly be possible to circumvent the waiting point. However, in this mass region, the Coulomb barrier is already so high, that the corresponding reaction rate is slower than the proton-capture rate. The temperatures are not high enough anymore, when the rp-process flow reaches these nuclei, which again supports the assumption, that the α-capture channel is blocked.

In a publication from 2004, the authors describe the observation of a double peak structure in the bolometric luminosity of X-ray bursts, cf. [5]. They consider the waiting points along the path as a possible explanation of this observation. Especially in the case of ^{30}S and ^{31}Cl, the accumulated abundance in the (p, γ) (γ, p)-equilibrium is shifted towards the ^{30}S isotope over time, since the proton-capture Q-value is low.

However, except a measurement of β-delayed proton decay, there is no direct data of the level structure of ^{31}Cl available, which finally determines the ^{30}S(p,γ) reaction. This is of special importance, since, from an evaluation of the isospin $\mathcal{T} = 3/2$ mirror nuclei of ^{31}Cl, it can be concluded, that a state just above the proton-separation threshold exists, which dominates the ^{30}S(p,γ) reaction rate. Therefore, it is of highest interest to measure the nuclear level parameters of the different states in ^{31}Cl to finally constrain the rp-process flow in this mass region.
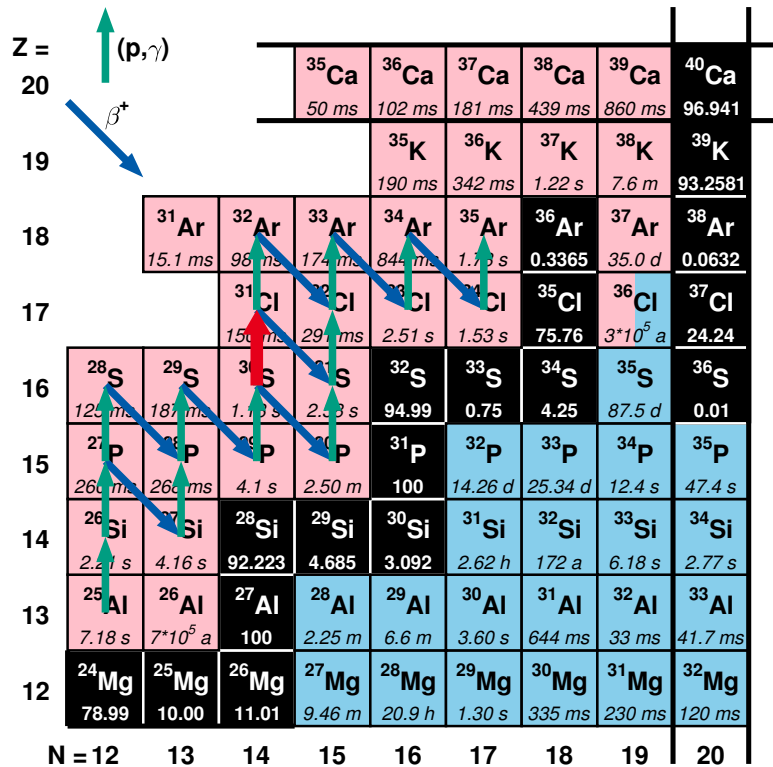
Figure 1.3: Part of the low-mass region of the rp-process flow for a certain temperature and density profile. The green arrows indicate proton-capture reactions and the blue arrows the β^+-decay. The (α,p) reaction is not shown. The assumed waiting point is situated at the $^{30}S(p,\gamma)^{31}Cl$ reaction.

1.3 Electromagnetic excitation

Electromagnetic excitation can be viewed as an inelastic excitation process, induced by electromagnetic radiation. In particular in nuclear reactions, it is possible to make use of the long-range electric or magnetic interactions of the reacting particles. A basic assumption of these types of reactions is, that the distance of the colliding nuclei is long compared to their radii. Otherwise, if they penetrate each other, the strong interaction reveals a much stronger reaction amplitude, and overwhelms the reaction.

The theoretical description of the collision process can be significantly simplified by assuming the nuclei moving along modified Rutherford trajectories. This situation is displayed in Fig. 1.4.
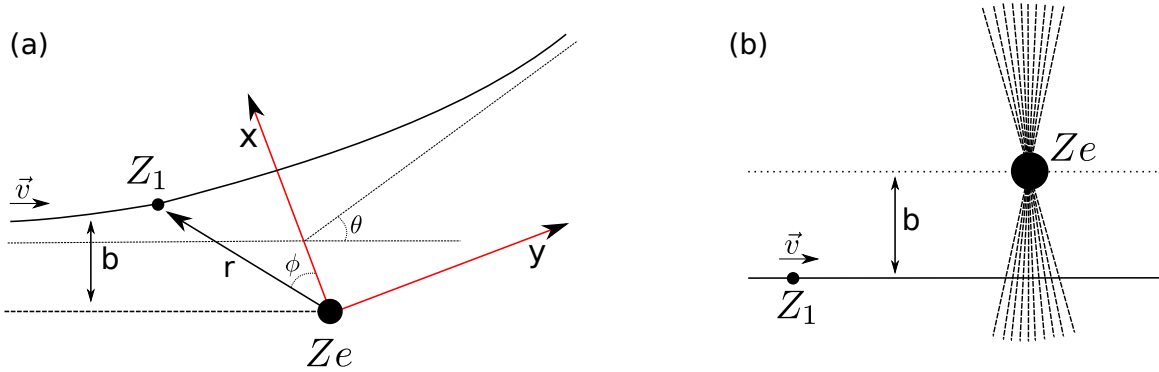
Figure 1.4: A target nucleus with charge Ze excites a projectile with charge Z_1, which moves along (a) a modified Rutherford trajectory in the non-relativistic case, and (b) straight lines, with very short interaction times, in the relativistic treatment, where $\theta \rightarrow 0$. In both cases, the impact parameter b is larger than the strong interaction radius.

A dimensionless quantity, which describes the strength of the interaction, is given by

$$\eta = \frac{Z_1 Z e^2}{\hbar v},$$

with Z being the corresponding charge of the target and the projectile, while v stands for the velocity of the incident beam. In the case of $\eta \gg 1$, the non-relativistic description can be used, and the trajectories of the particles are treated as Rutherford trajectories, shown in the left part of Fig. 1.4. Then, the classical Rutherford theory is employed to extract experimental cross sections and to compare those with theory.

However, in rare isotope beam facilities, relativistic ion-velocities are reached, and thus, the relativistic treatment has to be used, which corresponds to $\eta \ll 1$. In this case, the angle θ is approximately zero, and the trajectories can be treated as straight lines, as shown in the right part of Fig. 1.4.

The nuclear excitation of the projectile results from a short interaction of the projectile with the time-dependent electromagnetic field of the target. In order to describe this rapidly changing field in the relativistic case, different theories exist. The aim of the theories is to connect the measured differential cross sections with the corresponding matrix elements, being responsible for electromagnetic transitions in the nucleus from an initial state $|i\rangle$ to a final excited state $|f\rangle$.

The most intuitive theory originates from the idea of the *equivalent photons*, and was formulated by Weizsaecker [8] and Williams [9]. Originally, the theory is based on ideas from Fermi [10], but was continued by the two latter authors in more detail.

If a projectile moves with the velocity $v \simeq c$, the electric and magnetic fields of a

charge are Lorentz contracted perpendicular to its motion. They can be decomposed and written as [11]

$$
\begin{aligned}
E_{\perp} &= -\frac{Z_1 e \gamma v t}{(b^2 + (\gamma v t)^2)^{3/2}} \\
\vec{E}_{\parallel} &= -\frac{Z_1 e \gamma v \vec{b}}{(b^2 + (\gamma v t)^2)^{3/2}} \\
\vec{B}_{\perp} &= \frac{\vec{v}}{c} \times \vec{E}_{\perp} \\
B_{\parallel} &= 0.
\end{aligned}
$$

The relativistic Lorentz factor is given by $\gamma = (1 - v^2/c^2)^{-1/2}$.

In a relativistic collision with $\gamma \gg 1$, the electromagnetic field acts on a very short time scale. With the help of certain approximations and the standard electromagnetic field theory, the energy incident per unit area and per frequency interval can be written as

$$
I(\omega, b) = \frac{c}{4\pi} |\vec{E}(\omega) \times \vec{B}(\omega)|, \tag{1.1}
$$

where the fields are Fourier transformed to the frequency space. The major step is now to associate the virtual photons of the electromagnetic field with a pulse of radiation, consisting of real photons. The probability, that real photons interact with the projectile, is written as

$$
P(b) = \int I(\omega, b) \sigma_\gamma(\hbar\omega) d(\hbar\omega) = \int N(\omega, b) \sigma_\gamma(\omega) \frac{d\omega}{\omega}. \tag{1.2}
$$

Here, the photo cross section σ_γ is introduced, as well as the number of photons per unit area $N(\omega, b)$. Using the probability function P(b) and the integrated virtual photon numbers $n(\omega) = \int 2\pi b N(\omega, b) db$, and integrate this, it can be found that

$$
\sigma = \int 2\pi b P(b) db = \int n(\omega) \sigma_\gamma(\omega) \frac{d\omega}{\omega}. \tag{1.3}
$$

The number of virtual photons per unit area is a function, which decreases towards higher excitation energies, described by an adiabatic cutoff energy. This energy is calculated by

$$
E_\gamma^{max} = \frac{\gamma \hbar c}{b}. \tag{1.4}
$$

However, the calculation of the virtual photon spectra is not subject of this introduction, and can be found in excellent reviews, like e.g. [11], [12], and the references therein. Fig. 1.5 shows the calculated number of virtual photons for a certain beam energy and a ^{208}Pb target. The details are described in the caption of the figure.
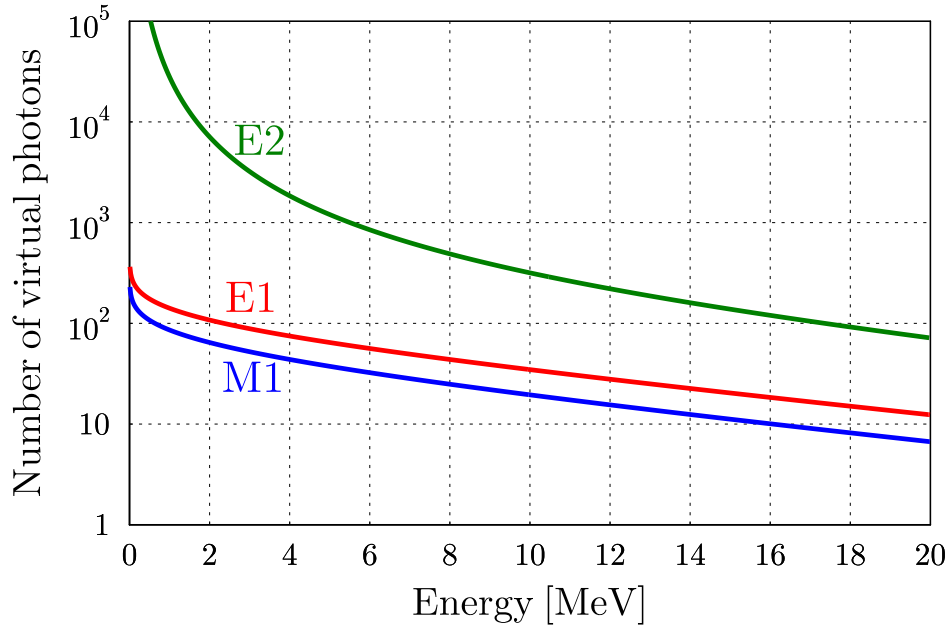
Figure 1.5: Number of virtual photons per unit area, decomposed in different Fourier components. The calculation is done for a ^{32}Ar beam at an energy of $E = 650$ AMeV. The field is produced by a heavy-Z ^{208}Pb target. The minimum impact parameter is chosen to be $b_{min} = 11.7$ fm.

Still, it is an open question, how the measured excitation cross section in an electromagnetic process at relativistic energies can be used to constrain the corresponding matrix elements. To do so, it is first of all important, that the time-dependent electromagnetic field interacts on very short times, while the projectile traverses the contracted field. It can be treated as a small perturbation in first-order time-dependent perturbation theory. Here, the excitation amplitude is connected with the matrix element and a potential $V[\vec{r}(t)]$, which can be derived from typical electromagnetic field theory (Lienard-Wiechert potential),

$$a_{fi} \propto \langle I_f M_f | V[\vec{r}(t)] | I_i M_i \rangle \,, \tag{1.5}$$

with $|IM\rangle$ being the corresponding eigenstates of the initial and final wave functions. Similarly to the classical electromagnetic theory, the field can be decomposed in a multipole expansion. This results in different matrix elements for electric and magnetic excitation modes, again subdivided into different multipoles λ. They are denoted by $\vec{M}(\pi \lambda m)$, where π could be E (electric) or M (magnetic), λ is the multipole characteristics ($\lambda = 1$ for dipole, $\lambda = 2$ for quadrupole etc.), and m is the conserved angular momentum number.

Usually, the matrix elements are incorporated into a more adequate quantity, which is

9

called the *reduced transition probability*, and is written as

$$B(\pi\lambda, I_i \to I_f) = \frac{1}{2I_i + 1} \sum_{M_i M_f} |\langle I_f M_f | \vec{M}(\pi\lambda m) | I_i M_i \rangle|^2. \qquad \boxed{1.6}$$

However, the relation between the involved matrix elements, or reduced transition strength, and the measured cross section can be performed by neglecting the orientation of the spin of the initial states, and taking

$$\sigma_{i \to f} = 2\pi \int \frac{b\,db}{(2I_i + 1)} \sum_{M_i M_f} |a_{fi}|^2, \qquad \boxed{1.7}$$

where the excitation amplitudes a_{fi} are given in equation 1.5.
Finally, the relation between the cross section and the matrix elements is

$$\sigma_{i \to f} \propto \sum_{\pi\lambda} B(\pi\lambda, I_i \to I_f), \qquad \boxed{1.8}$$

which is a summation over all possible multipole components in the field.

2

Setup

Performing large-scale experiments in inverse kinematics with very exotic beams usually incorporates many different stages from the production of the beam in a source to the final delivery at the experimental setup. At the GSI Helmholtzzentrum für Schwerionenforschung GmbH in Darmstadt, Germany, exotic beams at relativistic energies can be produced by the combination of a linear accelerator, a synchrotron (SIS18), and a fragment separator. Furthermore, with the in-flight separation method it is possible to produce and subsequently separate exotic beams for transport to different experimental areas. The experiment described in this thesis was performed at the ALADIN/LAND setup, situated in Cave C.

This chapter briefly describes the production and transport of the beam to the fragment separator (FRS) and is followed by a short description of the in-flight method, used to produce the final beam, which is delivered to the experiment. Main focus is on the experimental setup. Each detector will be described, according to its main function and the expected performance.

2.1 Beam production and transport

The production of radioactive beams starts with the acceleration of stable beams. The production of the ions is performed in a high-current ion source used to create and stabilize a high-energy plasma, and to extract the produced ions. In the experiment described in this thesis, a MUCIS source type was used. The MUlti Cusp Ion Source is a commonly used source type, known for excellent low emittance and high-luminosity extraction of the ions.

Two different gases were used for the experiment. For stable beam measurements, a ^{40}Ar beam was produced by ionization of ^{40}Ar gas in the MUCIS source. For the exotic argon beam settings, an enriched ^{36}Ar gas was used with a consumption of around 0.2 l/day.

Fig. 2.1 shows the entire accelerator complex at the GSI facility. The first acceleration stage is performed with the Universal Linear Accelerator (UNILAC). The low-energy beam transport behind the ion source operates at an injection energy of 2.2 AkeV and transports the beam via the high-current injector of the UNILAC to different acceleration stages in a row, like Radio Frequency Quadrupoles (RFQs), Interdigital H-type structures (IH), and Alvarez structures, where the ions gain energy and are accelerated
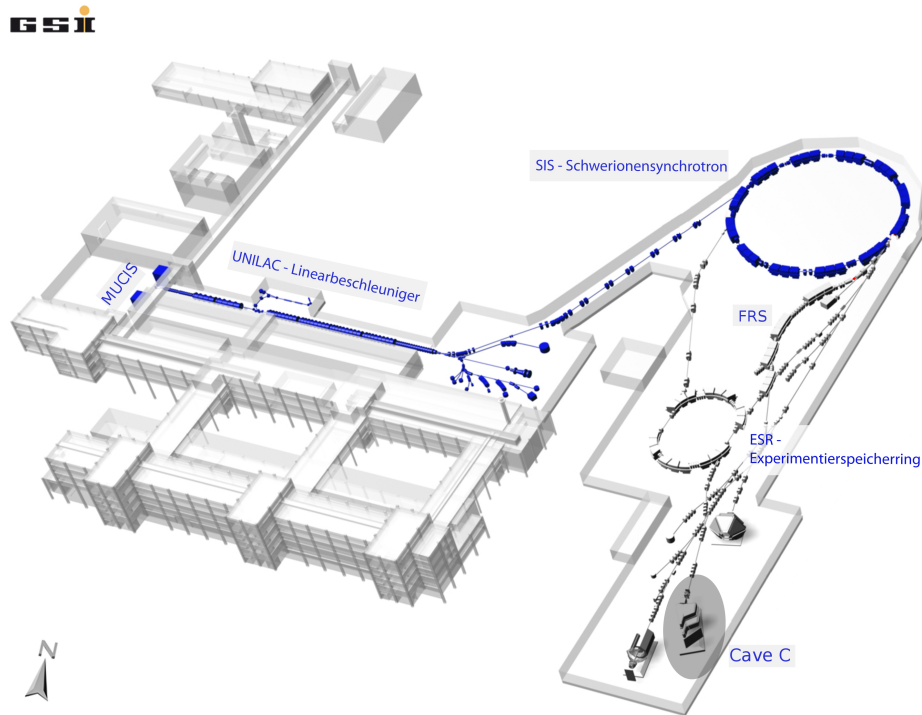
Figure 2.1: The accelerator structure of the GSI Helmholtzzentrum für Schwerionen-forschung GmbH in Darmstadt. Different stages comprise a linear accelerator and a synchrotron to accelerate ions to relativistic velocities. Taken from [13].

up to 11.4 AMeV, corresponding to $\beta = 0.15$, at the exit of the UNILAC. The length of this acceleration path is around 120 m, see [14]. At the output stage, the beam is not fully stripped yet. For this reason, a stripping foil is situated in the 130 m long transfer beam line from UNILAC to the next acceleration stage, the *SchwerIonenSynchrotron* (SIS18). The SIS18 is a fast cycling synchrotron with a circumference of 217 m and an average radius of 35 m. The maximum bending power is 18 Tm (SIS18), and the extraction energy varies in a broad range up to 4.5 GeV for a pure proton beam (i.e. $\beta = 0.985$). The extraction time can be chosen according to the needs of the experiment. A fast extraction mode, operating with a kicker and following septum magnets in the SIS18, is used to deliver high currents during a short time spill (like 500 ms spill length). The slow extraction, up to 10 seconds spill length, works by shifting the machines tune into an ion optical resonance state, in which it is subsequently possible to push the unstable particles by an electrostatic septum into the extraction channel. During the experiment described here, the slow extraction mode was used, and the maximum intensity of ions in the SIS18 during the experiment was around 3×10^{10} particles per

spill. Different beam energies were used for different ions, as can be seen in Tab. 2.1.

Table 2.1: Different beam energies and the corresponding $\beta = v/c$ at the exit of SIS18 used during the experiment.

Primary isotope	Energy (AMeV)	β	Comment
^{40}Ar	500	0.7593	Setting up and calibrations
^{36}Ar	825	0.8478	Main production run

Fragment Separator FRS

The transport of the primary beam to the different acceleration systems with its final stage in the SIS18 delivers a beam at relativistic velocities, which is now suited for the production of secondary beams, consisting of the desired exotic ions. Two main technologies are being employed in modern accelerator systems for production and separation of exotic beams. For low-energy experiments with a need for high intensity and not so extremely short-lived isotopes, the Isotope Separation On-line (ISOL) method is mainly used. Here, the exotic ions are produced in a combination of a thick production target and an attached ion source. A primary accelerated beam hits a thick target, in which secondary ions are produced. They diffuse inside the target area to the surface, and are ionized in the attached ion source. A post-accelerator is subsequently used to increase the beam energy and for separation and transportation of the secondary beam to various experimental setups.

The FRagment Separator (FRS) at GSI, as shown in Fig. 2.2, utilizes the in-flight separation method [15], which is the second technique. The primary beam at high energies penetrates a production target, situated at the entrance of the FRS. Interaction of the beam with the target material leads to fragmentation, and results in a suite of different exotic isotopes. A system of ion-optical devices, like magnets and degraders, is subsequently used for separation and transportation of the exotic isotopes to different experimental setups.

The fragmentation target is situated behind SIS18. A short transport channel guides the beam from the SIS18 to the target area of the FRS, where different targets are accessible and mounted on a target ladder. In the described experiment, a beryllium target was used with an areal density of 6347 mg/cm^2. In order to calculate production yields and the corresponding fragmentation cross sections in the target for the different produced exotic isotopes, an empirical parametrization of the fragmentation cross sections is used, which is called EPAXII[1]. It is based on combined data sets from heavy-ion induced

---

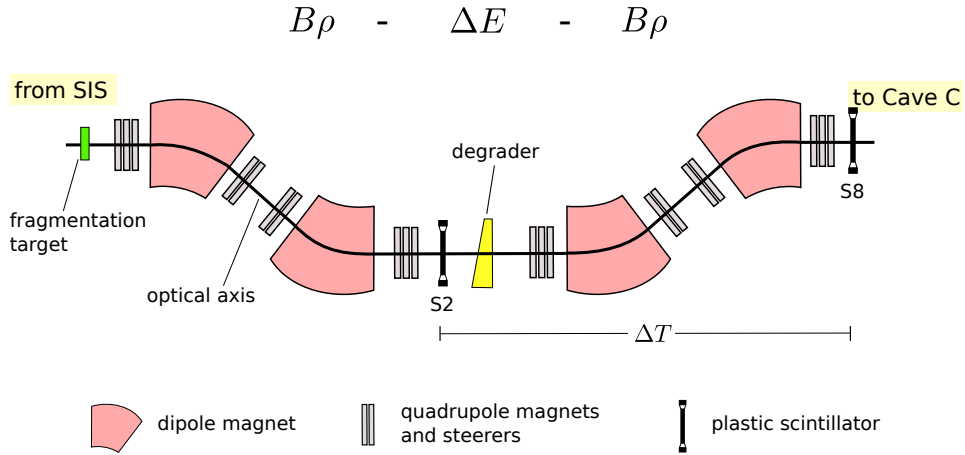[1]An Empirical Parametrization of Projectile-Fragmentation Cross Sections

Figure 2.2: The fragment separator (FRS) at GSI, situated behind the SIS18. Different stages are indicated, utilizing the in-flight separation method with a $B\rho - \Delta E - B\rho$ technique. In total four stages are used for purification of the beam and enhancement of the beam quality.

fragmentation reactions and proton-induced spallation processes [16]. In order to simulate the beam selection and transportation through the FRS, a Monte-Carlo simulation for projectile fragments, called MOCADI, is used. This code allows the calculation of the ion-optical transport of the beam through a system of magnets and degraders. It involves energy losses in materials, atomic and nuclear interactions, and charge-state calculations.

The FRS makes use of a common in-flight separation technique, called $B\rho - \Delta E - B\rho$, as shown in Fig. 2.2. Different steps are used to separate the beam ingredients and to advance the purity of the beam.

In total, four groups of dipole and quadrupole magnets are arranged to provide the ion-optical requirements for beam separation on a mass-to-charge basis. The method is based on the deflection of ions in a magnetic field for different A/Z ratios. Dipole magnets are used to bend the trajectory of the ions along the ion-optical path, whereas quadrupole magnets are used to correct for aberrations of the beam envelopes. Optical aberrations of even higher orders can be corrected by sextupole magnets, which are situated directly behind the dipole magnets. The four stages with their individual focal planes are used to purify the beam by means of A/Z. Each dipole magnet can therefore be used to bend the beam by an angle of 30°. At the exit of the FRS, the beam usually has an achromatic focus, i.e. the fragments are focused independent of their initial angle or momentum spread. This enables individual experiments to localize the beam spot on a defined small area on the secondary production target.

Besides the bending and focusing magnets, matter can be inserted into the middle focus plane of the device. Ions passing this matter deposit energy according to the square of

their nuclear charge, i.e. $\Delta E \propto Z^2$, which allows the separation of isobars.

To track individual ions through the FRS, a set of suitable detector types is used to measure the time of flight, the position, and the energy loss of the ions at different stages. This enables event-by-event identification of the incoming ions, which is the essential first step for the identification of the reaction channel. This is performed later during the analysis of the experiment. The scintillation detectors, used for the time-of-flight measurement in the FRS, are marked with S2 and S8 in Fig. 2.2.

Table 2.2: Different materials used in the FRS during the experiment. The areal density of the BC420 material is taken from [17].

Device	Material	Thickness [mm]	Areal density [g/cm^2]	Size [mm×mm]
FRS target	Be	34.3	6.347	-
S2	BC420	3.25	1.032	220×45
Degrader	Al	-	2	-
S8	BC420	3	1.032	220×100

During the experiment, the S2 scintillator detector failed because of the high intensity in the middle focus plane of the FRS. This results in a missing time-of-flight measurement between S2 and S8. However, it was possible to use only the time from S8 to the entrance of the experimental hall for an identification of the beam ingredients.

In general, the in-flight separation in the FRS is very efficient and can be used to extract even the most exotic fragmentation products with still sufficient transport efficiency. The measured transmission efficiency was 75 % for S2 → S8 and 51 % for S8 → Cave C, and was calculated with MOCADI to 95 % and 36 %.

2.2 Experimental setup: Cave C

At the final stage of the FRS the ions pass through S8 and provide a signal for a time-of-flight measurement, using the first timing detector in the experimental hall Cave C. The transfer beam line consists only of dipole and quadrupole magnets to bend and focus the beam along the optical axis. No further matter is included to influence the beam transport from the FRS to the experimental setup as little as possible.

In order to calibrate the time measurements, which is hampered by different cable lengths and electronics, three primary beam runs with exactly defined beam energies, are used to extract the necessary parameters.
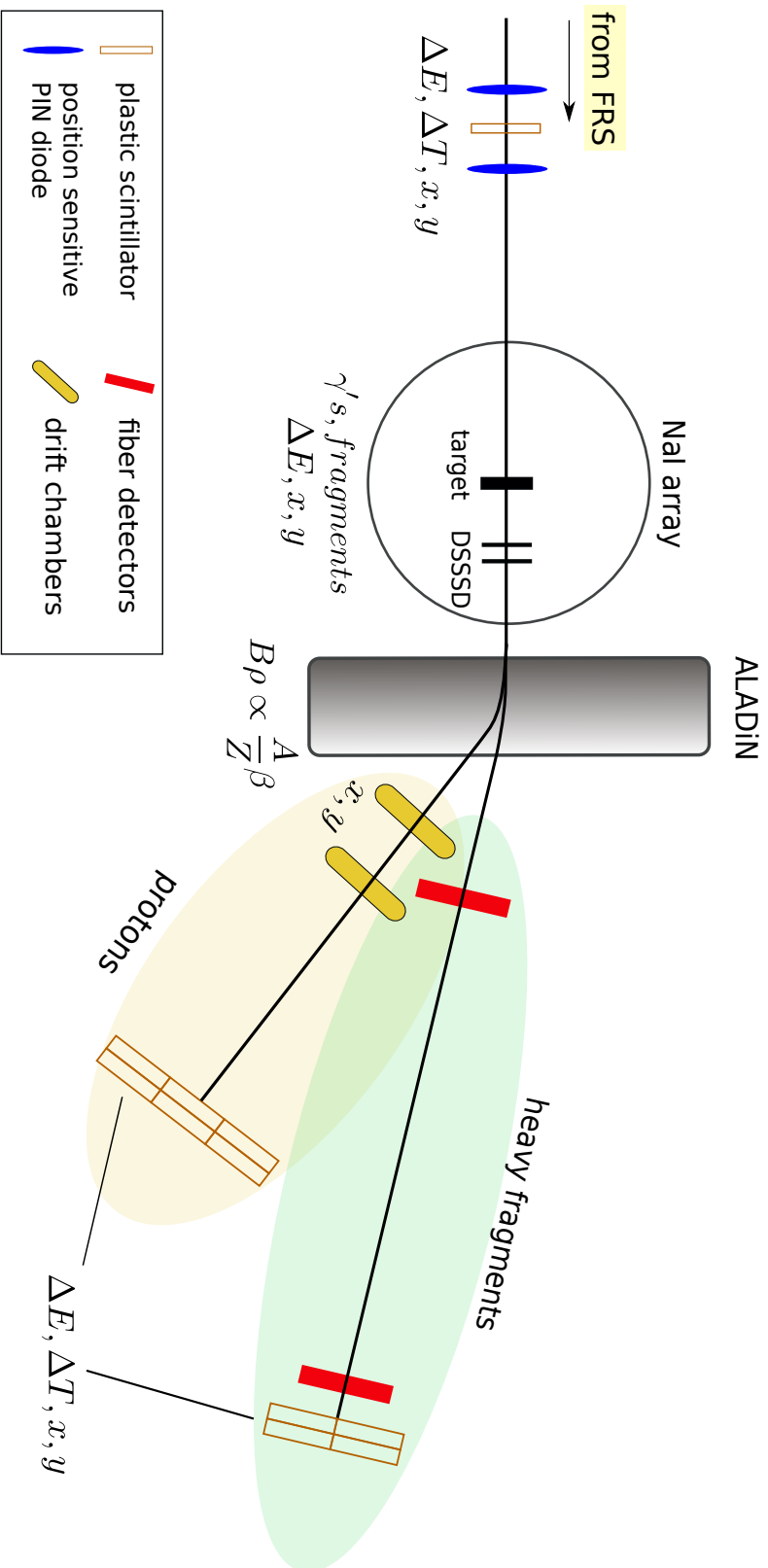
Figure 2.3: The ALADIN/LAND setup, situated in *Cave C*. In total, the experimental area has a length of around 20 m. Different detector types are used to measure in inverse and full kinematics. The distance from the last detector in the FRS to the first detector in the setup is around 55 m. See text for further details. Figure is not to scale.

16

2.2.1 Overview

Using the invariant mass method in inverse kinematics requires a set of different detector types and the corresponding read-out parts. Each detector fulfills individual requirements to reconstruct the desired quantity with high resolution and with the highest possible efficiency. The relativistic beam energy provides a big advantage, since the particles are boosted in forward direction in the laboratory system, which enables the use of smaller detector systems on the one hand, and results in a good coverage of the solid angle in the center-of-mass system on the other hand.
Fig. 2.3 shows a sketch of the ALADIN/LAND setup. Different calibrations are required to measure exact distances, offsets, and energy losses in MeV for individual detectors. For each experiment, a set of detectors can be chosen to the correspondingly involved physics.
In the next sections, a description of all detector systems and the data read out will be given.

2.2.2 Data acquisition

One of the crucial components of each nuclear physics experiment is the data acquisition. Apart from the concern of stability, the data acquisition must be fast, and should handle a huge amount of data in short times, without mixing events, or any other spoiling of the data. The dead time of the system (the time, in which the total system is blocked) has to be reduced to a minimum. Basic data reduction should be performed without losing good data.
For this reason, the ALADIN/LAND experiment makes use of a GSI internal development, the multiple branch system (MBS). It is being used at many other places and works fast, reliable, and it is well-suited for the needs of a large-scale experiment. Making use of many different subsystems requires a complex structure of internal timing. The subsystems are spread over a complete experimental hall, and long cables are used to connect the systems. There are different approaches to establish a reliable connection between different subsystems. In the MBS, two ingredients are common for all subsystems:

- a processor for running the readout function and for providing the network sockets

- a trigger module for internal dead-time blocking, being chained and in-phase with other systems.

As the system is capable of different standards, like e.g. Fastbus, CAMAC, VME, it is an universal tool for data acquisition.
Synchronization, data streaming, data collecting, and data sending is internally performed, and there is no need for the experimentalist to work on that. A specially suited user read-out function enables the experimentalists to include own specifications, and to implement the necessary functions for each individual data module.

Table 2.3: Different read-out systems used in the experiment according to the corresponding detector.

Detector	Type	Channels	Standard	Data acquisition modules
S2 and S8	plastic scint.	4	CAMAC	Silena 4418Q QDC Silena 4418T TDC
PSP	PIN diode	5	CAMAC	Phillips 7164H ADC
POS	plastic scint.	4	CAMAC	Silena 4418Q QDC Silena 4418T TDC
CB	NaI crystals	162	Fastbus	LeCroy 1885F QDC LeCroy 1875 TDC
DSSSD	Si strip	1024	VME	SIDEREM & SAM
PDC	wire chamber	2	VME	CCB & SAM
GFI	scint. fibers	34	Fastbus	LeCroy 1885F QDC
TFW	plastic scint.	64	Fastbus	LeCroy 1885F QDC LeCroy 1875 TDC
NTF	plastic scint.	32	VME	CAEN v792 QDC CAEN v775 TDC

Fig. 2.4 shows the basic read-out principle for most of the detectors used in the setup. Many detectors use photomultiplier tubes (PMTs) to measure the produced light during passage of the beam through the material. PMTs consist of several stages of anodes, called dynodes, where electrons, created by the photons of the scintillation light, are accelerated and multiplied in an electric field. The drop of the voltage behind the last dynode, induced by a last resistor, can finally be measured, shown as an electrical pulse in Fig. 2.4. This pulse is subsequently split with a ratio of 80:20 in a special split box behind the PMT. Two different branches are used independently to measure time and energy. The energy signal is delayed for a certain time with passive delays, and is subsequently fed into a charge-to-digital converter (QDC). The time branch is again subdivided into two main components.

To measure the arrival time of the ion, a constant-fraction discriminator (CFD) triggers, if the signal is above a certain threshold. The digital output signal of the CFD is then delayed and fed into a time-to-digital converter (TDC). During this time, a trigger decision has to be made. Therefore, the digital signal of another output of the CFD is sent to the main acquisition system, which checks for dead time, trigger combinations, and downscaling, and finally provides a master gate, which is sent back to the different subsystems. The gates for the QDC and the common stop (or common start) are gen-

erated and subsequently fed into the data-acquisition modules.

During digitization in the modules (provided a successful master gate was generated), a trigger for the read-out function, marked in Fig. 2.4 with "TRIVA trigger", is sent via a specially designed data bus to the individual front-ends. Finally, the read-out function is called to perform the read out of the modules and the data sending to a general place, the event builder, where the data is merged and compressed, is initiated. At this stage, the merged event information are sent out via network to be stored.

In general, the total time consumed for this process is up to a few hundred microseconds, and is therefore blocking the system during this time from acquiring the next event. In total 16 different detector triggers can be included into the system, and they can be logically combined. Eight detector triggers are used for physics events, whereas the other eight signals are used for offspill and calibration issues.
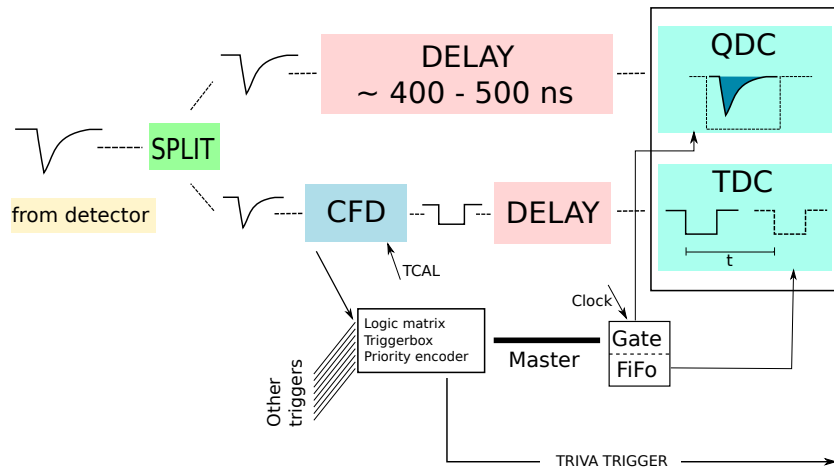

Figure 2.4: The conversion steps of a typical photomultiplier-based detector signal. A dedicated timing and an energy branch are separated, after the signal was split with a fraction of (80:20). Conversion modules, like TDCs and QDCs, are used to digitize the signal. Meanwhile, a special branch takes care of the trigger issues.

Trigger combinations

In order to combine different detector triggers to physics triggers, defined by the experimental needs, the *LeCroy 2365 Octal Logic Matrix* is used. The single detector triggers are connected to the input of the module. Internally, a logic matrix builds combinations of the different signals by applying AND/OR conditions, and finally produces a trigger signal, if the conditions are fulfilled. These signals are connected to a trigger box (TB8000), which performs the downscaling and the dead-time blocking. Furthermore, a

special data word is produced and sent to the event stream. The trigger pattern (TPAT) is a 16-bit word, encoding the trigger, which was delivered to the trigger box. Besides other information, each event header comprises the corresponding uniquely defined trigger word.

In total, eight physics triggers exist with different logical combinations of detectors. As an example, the fragment trigger comprises events, which are detected in the incoming part of the setup (spill on), with a good position on the target and a corresponding signal from a detector in the fragment branch.

Eight other triggers are used for calibration and other offspill event types. Fig. 2.5 shows the setup of the logic matrix.

Tpat#	Tpat name	spill on	pile-up	pixel	cb del. SUM	cb del. OR	FRS S8	cb SUM	ntf cosm.	tfw cosm.	cb OR	tfw mult.	veto wall	land cosm.	land mult.	ntf mult.	pos:ROLU	
1	Min. bias	∧														∧		physics
2	Fragment	∧	¬												∧	∧		
4	CB OR	∧	¬					∧							∧	∧		
8	CB SUM	∧	¬			∧									∧	∧		
16	Proton	∧	¬							∧					∧	∧		
32	Min. Bias - PileUp	∧	¬													∧		
64	Pixel	∧		∧												∧		
128	Neutron	∧	¬											∧	∧	∧		
256	CB muon	¬			∧											¬		offspill & calib.
512	LAND cosm.	¬											∧			¬		
1024	TFW cosm.	¬							∧							¬		
2048	CB cosm.	¬				∧										¬		
4096	Clock																	
8192	TCAL																	
-	Spill on																	aux.
-	Spill off																	

Figure 2.5: The logic conditions used in the logic matrix, combining different single detector triggers to eight physics and eight offspill triggers. The '∧' symbol indicates an AND condition, whereas the ¬ shows a NOT-AND relation.

2.2.3 The incoming detection

In order to perform a full incoming tracking for reconstruction of the four-momentum of each individual particle, a set of detectors is situated at the entrance of cave C, upstream to the secondary target. Behind the FRS, a transfer channel leads the ion beam to the experimental hall. The last detector in the FRS is the S8 plastic scintillator. The first detector in the experimental hall is a silicon PIN diode (PSP1) to measure the energy loss and the position on the detector, and hence to extract the charge and the trajectory of the ion.
The following detector is a plastic scintillator (POS) to measure times and to give the start trigger for the data acquisition. Behind this plastic scintillator, again a silicon PIN diode (PSP2) is situated to measure the energy loss and the position of the interaction in the detector.

PSP

In total two PSPs are used to measure the position and the energy loss of the incoming ions. A PSP consists of n-type silicon material and has a square shape with the size of 4.5×4.5 cm^2. The front side has boron ions implemented to form a pn-junction. This side is used as the anode and the back side is used as the cathode. In total 5 read-out pins are implemented. The deposited charge is proportional to the amount of electron-hole combinations formed while the beam traverses the material. They move towards the 4 read-out channels on the front side and induce a small current. With this information, it is possible to reconstruct the position of the ion. Therefore, the measured current Q_i of the individual read-out channels (with $i = 1, 2, 3, 4$) on the front-side are related to each other and weighted by the total deposited energy. It is subsequently possible to reconstruct x and y via the relations

$$x = \frac{(Q_2 + Q_3) - (Q_4 + Q_1)}{Q_1 + Q_2 + Q_3 + Q_4}$$
$$y = \frac{(Q_1 + Q_2) - (Q_3 + Q_4)}{Q_1 + Q_2 + Q_3 + Q_4}.$$

A position resolution of $\sigma \approx 200$ μm can be achieved with this detector. The backside, i.e. the cathode, of the PSP is used for the measurement of the total deposited energy. One single read-out channel picks up the ionization charge of the PSP (i.e. the current induced by the moving charge carriers), and this pulse can be used to measure ΔE. The achieved energy resolution is around 1 %.
In the analysis, both PSPs are combined to reconstruct the energy loss, the trajectory of the incoming ion, and to determine the exact angle and position on the target by extrapolation of the trajectory onto the target position. Fig. 2.6 shows a sketch of the PSP detector with its read-out positions.
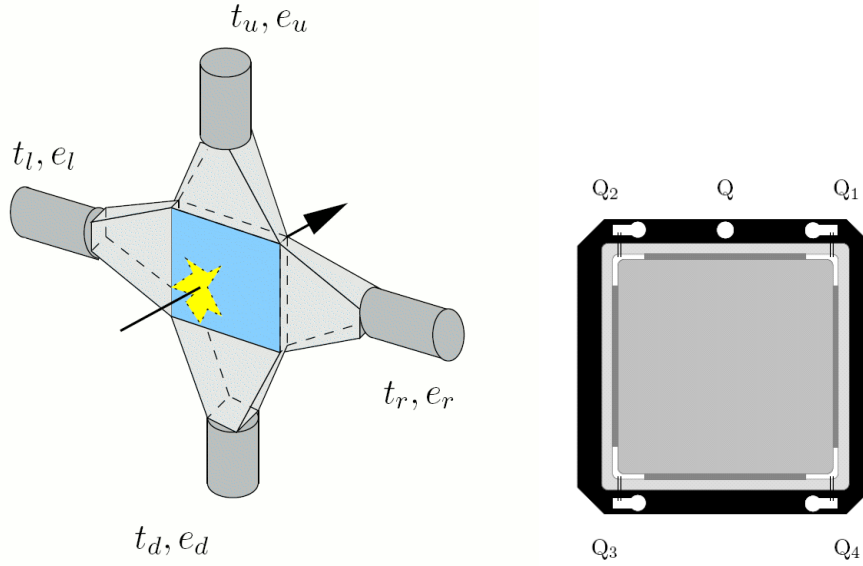
Figure 2.6: The two detectors used to constrain the incoming beam. The left picture shows a sketch of the POS detector, made of plastic scintillation material, which is optically coupled to four PMTs, enabling fast timing measurements (taken from [18]). The right picture shows the position sensitive PIN diode with its four read-out positions Q_i on the front side, and the anode read out Q on the back side. Picture taken from [19].

POS

In order to measure the incoming velocity and the corresponding beam energy, a time-of-flight measurement is performed. Therefore, a scintillator material with four fast PMTs attached is used. Different time-of-flight measurements can be performed with this detector, which is called POS, and which is shown on the left side of Fig. 2.6. For the incoming tracking, the time of flight from the S8 detector to the POS detector is used to calculate the energy of the incoming ions. According to the relation

$$B\rho \propto \frac{A}{Z}\beta\gamma,$$

it is possible to calculate the mass-over-charge ratio A/Z, if the magnetic rigidity $B\rho$ and an exact measurement of β is available. Since

$$\beta = \frac{v}{c} = \frac{d_{S8-POS}}{ToF \times c},$$

where d is the distance between S8 and POS known from the calibration, and c is the speed of light, it is possible to reconstruct A/Z for each individual ion by measuring the

time of flight (ToF) between S8 and POS.

POS has an active area of 2.5×2.5 cm^2 and a thickness of 200 μm. Four PMTs are optically attached to light guides of the detector, which transport the light with high efficiency to the PMTs. The intrinsic time resolution of the POS detector is determined to be $\sigma \approx 25$ ps, allowing exact time-of-flight measurements in combination with other timing detectors.

Another important usage of the POS detector arises from providing a time stamp for each event.

ROLU

Another detector is the ROLU detector. It mainly acts as a VETO detector for the setup. If a particle passes through the detector, the data acquisition will not record this particular event and discard it. The detector consists of four individual plastic scintillators, which are mounted in a movable frame. Two scintillators are mounted horizontally, whereas the other two are arranged vertically. Because of this, it is possible to open and close a rectangular window in the center of the detector with a step motor, which moves the individual parts along the x- and y-axis. The window in the center of the arrangement is used to define the beam size. All particles crossing this window are accepted and recorded, whereas the ions, hitting the ROLU detector, are discarded.

Distances and remarks

The measured distances to the main secondary production target are 227 cm from PSP1, 194.3 cm from POS and 105.3 cm from PSP2. In general, with these information, a complete incoming tracking and reconstruction of the four-momentum of each particle is possible and performed within the analysis. Particle trajectories can be calculated and extrapolated onto the target to yield a position of the ion on the target. From this point on, the outgoing tracking is required, in order to reconstruct the four-momentum of all outgoing particles. This is more complex, since it is not exactly known, how many particles are produced in different open reaction channels. Therefore, more complex algorithms are needed to perform the outgoing particle reconstruction.

2.2.4 The fragment detection before the magnet

A certain amount of time and effort is spent on adjusting the beam at the beginning of the experiment. Basically, a beam with a diameter of only a few millimeters, which hits the target in a restricted area, would be the ideal case for reconstruction of the trajectories of the outgoing particles. In reality, different distortions make the beam wider and spread out over the target. Since there are a few last quadrupoles in the experimental hall, which can be controlled remotely by the experimentalists, it is possible to further adjust the beam spot and the diameter of the beam envelopes to a certain level.

The reaction target is mounted on a wheel. This wheel can be moved remotely, in order to allow the use of different samples without interruptions of the vacuum. A step motor is used to access in total nine different target positions. Several target materials with individual thicknesses are mounted in the frame of the wheel. One frame is left empty, in order to perform a measurement without any target in the beam. This is used for subtracting the empty target data from runs with a target inserted, since a lot of other materials, like vacuum windows and foils, are traversed by the beam, which create break-ups and other reactions.

The properties of the targets are chosen based on the desired reactions, like the composition, the thickness, the areal density, and the purity. The main target used to induce the electromagnetic excitation is a ^{208}Pb target with an areal density of 515 mg/cm^2. The target dimension is 3×3 cm^2.

In order to subtract nuclear background contributions, a ^{12}C target is used. This target has a thickness of 2 mm and a corresponding areal density of 369.8 mg/cm^2.

γ-ray detection

In order to detect γ-rays emitted from a moving excited ion, a spherical 4π γ-detector is placed around the target to cover the full solid angle. This detector consists of 162 NaI crystals and is called Crystal Ball. It consists of 12 pentagonal and 150 hexagonal shaped NaI crystals, to reach an equally distributed solid angle coverage over all crystals, shown schematically in Fig. 2.7.

The total excitation energy of the excited state in the ion can be reconstructed by measurement of the sum energy, whereas the multiplicity, i.e. the total number of NaI crystals, which registered an event, serves as a basis for the analysis of cascades and angular correlations of a γ-decay in a nucleus. The granularity of the detector allows the correction of the Doppler-shift of the emitted γ-rays. The total efficiency is between 90 % (for $E_\gamma = 1.3$ MeV) and 96 % (for $E_\gamma = 3$ MeV). The single crystals reach intrinsic energy resolutions of 5 % to 10 % in the full energy peak [20].

DSSSD

The reaction products are strongly boosted in forward direction in the laboratory frame, since the incoming beam has relativistic energies. This enables the use of more localized detector systems behind the target for detection and tracking of the outgoing particles, although they need a higher intrinsic granularity to resolve different trajectories of the particles. Therefore, a set of two Double-Sided Silicon Strip Detectors (DSSSDs) is placed downstream of the target at a distance of 107 mm and 133 mm.

The DSSSDs provide independent read-out strips for a measurement of the x- and y-position of the ion track. In total 1024 strips are used per detector, with 640 strips for the x-direction and 384 for the y-direction. The pitch size is different for each direction, i.e. 27.5 μm for the x- and 104 μm for the y-direction. The total active area of the
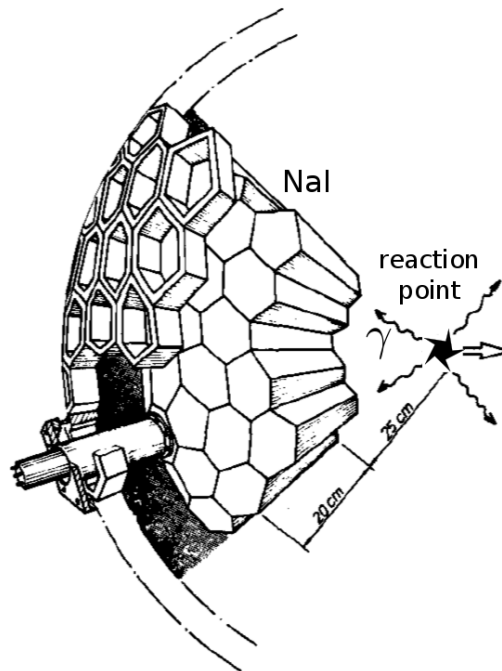
Figure 2.7: A part of the Crystal Ball used in the ALADIN/LAND setup. The detector is composed of 162 NaI crystals with different shapes to reach a maximum coverage of the full solid angle. PMTs are attached, in order to read out the produced signal. The picture is taken from [20].

DSSSDs is 72×40 mm^2 with a thickness of 0.3 mm.

The energy deposition in matter depends on the atomic Z of the impinging ion. In principle, this allows the determination of the charge, based on the energy loss.

The main purpose of the DSSSDs is the extraction of the position of the interaction with a position resolution of $\sigma \approx 100$ μm.

2.2.5 The proton branch

In the homogeneous magnetic field of the ALADIN magnet the heavy-ions and protons are separated based on their different mass-over-charge ratio. This separation enables the usage of two different branches: the proton and the heavy-ion branch with individually designed detectors for high-efficiency and large-acceptance performance. A particle without any deflection in ALADIN would travel along a straight line (0°-line) through the magnetic field. The detectors of the heavy-ion branch are situated at an angle of 16.7° with respect to the 0°-line. The proton branch detectors are arranged at an angle of 31° with respect to the 0° line. This provides a clear separation of different reaction

products behind the ALADIN magnet. Two different detector systems are employed to measure the protons of the reactions. In order to extract the position of the protons, two wire drift chambers are used. Behind them, a time-of-flight wall is situated to measure the energy loss and the corresponding time of flight of the protons. This setup allows to measure all kinematical variables of the protons, and to reconstruct their four-momentum.

PDC

The proton drift chambers (PDCs) are wire chambers, filled with a mixture of argon (80 %) and CO_2 (20 %). A passing proton ionizes the gas and produces an electron avalanche, which drifts to the read-out wires. As shown in Fig. 2.8, the active area is 100×80 cm^2, and consists of 144 wires in x-direction and 112 wires in y-direction. The anticipated spatial resolution is about 200 μm for minimum ionizing particles with an efficiency of 95 %.

The hit positions, measured with the PDCs, are an essential part of the proton tracking algorithm. By combining the hit positions on both PDCs and the hit positions on the DSSSDs, it is thus possible to determine an accurate track of the proton through the magnetic field.
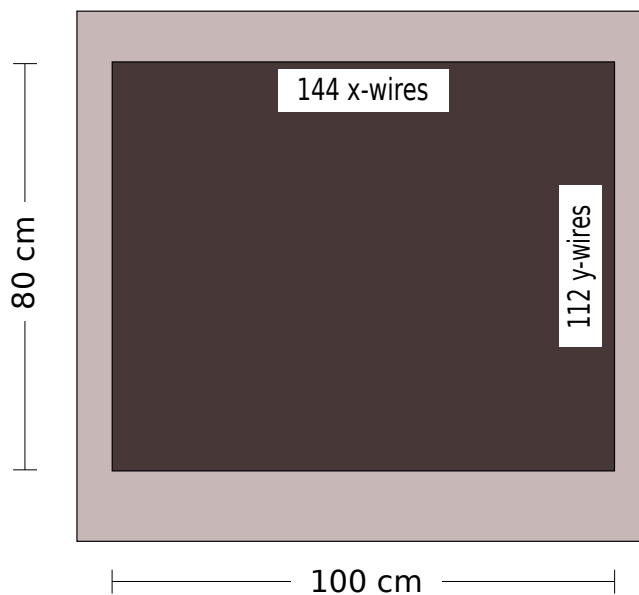
Figure 2.8: A front view of the proton drift chambers. It is used in the proton branch of the setup in order to measure the trajectories of the emitted protons with a desired position resolution of 200 μm.

In order to reach a position resolution of $\sigma \approx 200$ μm, a detailed knowledge about the drift characteristics of the produced electrons in the gas is required. For this purpose, simulations are performed with the Garfield simulation package. This code allows to simulate two- and three-dimensional drift chambers and the transportation properties of the gas mixture [21]. In principal, there are different methods available, how the interaction position on the PDCs can be determined. The simulation of the drift characteristics and the velocity of the electrons drifting towards the wires, is performed with the Garfield simulation, and results in an x(t)-curve, which correlates the arrival time t to the radius x (distance of the wires is around 7 mm). Thus, the position of the interaction on the PDC can be extracted from the arrival time. The simulation method is a well-suited possibility to determine the x(t)-curve, but it would require to simulate the x(t)-curve for each individual experiment. Another possibility is to make use of the experimental data, which enables a more experiment-specific calculation of the x(t)-curve. This algorithm is used in the analysis [22].

TFW

The big time-of-flight wall (TFW) consists of 32 plastic scintillation paddles. At each paddle two fast PMTs are attached for detection of the scintillation light. In total 18 horizontal and 14 vertical paddles are arranged as shown in Fig. 2.9. Each vertical paddle has the dimension of $147 \times 10 \times 0.5$ cm^3, whereas the horizontal paddles have the dimension of $189 \times 10 \times 0.5$ cm^3. Thus, it is well suited for time-of-flight and energy-loss measurements.

Two layers, arranged in opposite directions, have the advantage of connecting independent information from four PMTs about the energy loss and time. Besides this, it is easier to calibrate the paddles in terms of energy and time synchronization.

The expected time resolution of the TFW is $\sigma \approx 100$ ps. The energy loss and the corresponding scintillation light yield depends on the atomic charge Z of the incident ion, which is minimal for protons. This results in low energy loss of the proton in the TFW and demands high voltages for the PMTs. A calculation with SRIM, a simulation package for the energy loss of ions traversing a target material (Stopping and Range of Ions in Matter, c.f. [23]), shows an electromagnetic stopping power for protons in plastic material of $dE/dx \approx 250$ keV/mm for $E_p = 650$ MeV and $dE/dx \approx 316$ keV/mm for $E_p = 350$ MeV. The corresponding projected full-stopping range is 177 cm and 66.8 cm, respectively.

The position of the interaction can be determined by measuring the arrival time of the scintillation light at the two attached PMTs. A hit in the middle would produce scintillation light, which arrives at the same time at both ends of the paddle. Therefore, it is possible to calculate the hit position from the time difference of both PMTs, taking the speed of light in the particular material in account. In a similar manner, it is possible to calculate the deposited energy, which should be independent of the position of the hit.
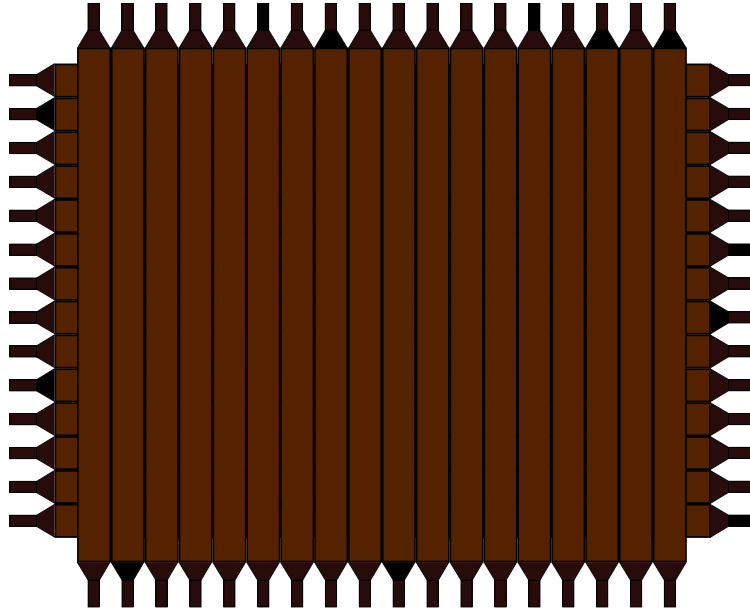
Figure 2.9: The big time-of-flight wall is used to measure the arrival time of the protons in the proton branch. It consists of 32 paddles of plastic scintillation bars with optically coupled PMTs. Note, that the lengths of the 18 bars in horizontal and the 14 bars in vertical directions are different (189 cm and 147 cm, respectively).

2.2.6 The heavy-ion branch

According to

$$B\rho \propto \frac{A}{Z}\beta\gamma,$$

the deflection of an ion in a magnetic field depends on the mass-over-charge ratio. It is clear, that protons are much more deflected than the residual ions. The mass and charge separation of ALADIN allows to make use of a special heavy-ion branch in the setup. Similar to the proton branch, two different detector types are used to measure the trajectory, the time of flight, and the charge of the residual heavy-ions. Furthermore, a reconstruction of the mass of the heavy-ion is possible by employing a special tracking algorithm.

GFI

After the ALADIN magnet, the ions are moving through air, which makes it more difficult to constrain the exact trajectory of the ions, because the charged reaction products scatter on air molecules. Similar to the proton branch, a special detector type is used to measure the x-position of the interaction. The detectors are called *Grosse Fiber Detektoren* (GFI), and two detectors are situated at a distance of 5.2 m and 7.3 m from the secondary production target behind the ALADIN magnet.

As shown in the top of Fig. 2.10, the GFIs have an active area of 50×50 cm^2 with 475 scintillation fibers arranged vertically. The fibers have a quadratic cross section of 1×1 mm^2, and a fiber-fiber distance of approx. 1 mm. For more information, see [24]. Intrinsically, the GFIs show a position resolution of less than 1 mm, depending on the charge of the heavy residuals. Thus, it is possible, similar to the proton drift chambers, to constrain the trajectory of the ions and to track the particles in combination with the position on the DSSSDs through the magnetic field.

NTF

The last detector in the heavy-ion branch is the *Neue ToF* wall (NTF), shown in the bottom of Fig. 2.10. It has a smaller size than the TFW, however, the working principle is exactly the same. It consists of 16 paddles of plastic scintillation material with the dimension of $48 \times 6 \times 0.5$ cm^3. Eight paddles are arranged horizontally, and the other eight paddles vertically. This results in the same advantages as for the TFW. At each end of a paddle, fast PMTs are optically attached to measure the scintillation light.

Since the momentum transfer in the reaction and the deflection angle of the heavy-ions in the magnetic field of ALADIN is small, the total beam spread is less than for protons. For this reason, the small active area of the NTF is sufficient to cover the expected illuminated area.

In order to produce an internal synchronization of the time and the energy, a special sweep run is performed. By variation of the magnetic field, it is possible to diversify the horizontal position of the beam and to illuminate at least all vertical paddles. By inserting a high-Z target, the resulting beam spread in y-direction can subsequently be used to hit a small range of different y-paddles and to perform the synchronization also for them.
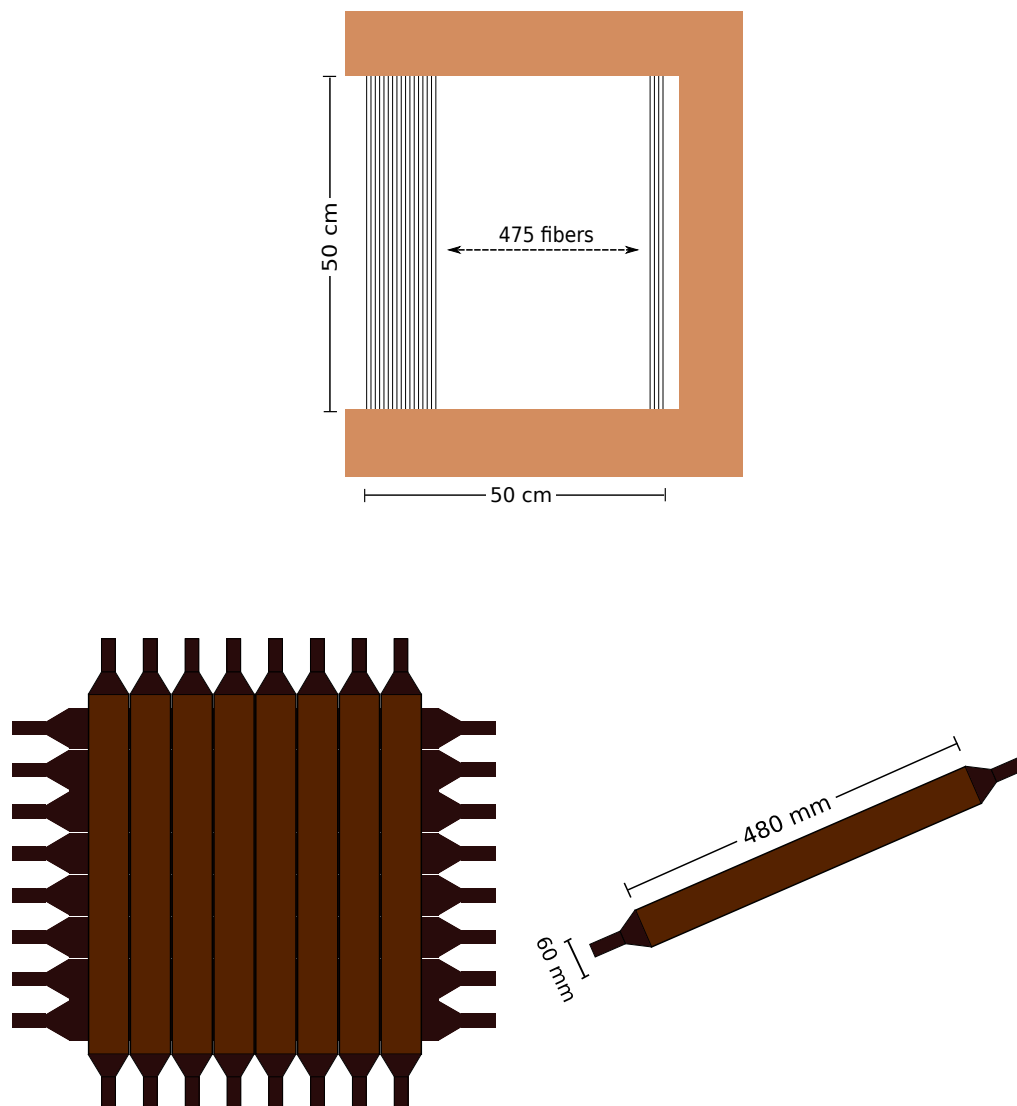
Figure 2.10: The two detectors used in the fragment branch. The GFI detector (top) consists of vertically arranged plastic scintillation fibers to measure the hit position of a heavy residual with a resolution of around 1 mm. A position sensitive PMT with a special read-out grid mask is attached to the fibers. The NTF (bottom) is arranged in a similar way as the TFW in the proton branch. Here, 16 scintillation paddles of the size $48 \times 6 \times 0.5$ cm^3 are equally distributed in horizontal and vertical direction.

3

LENA

Low Energy Neutron detector Array

In the following years, a major upgrade of the existing GSI facility will be built. At the international accelerator facility FAIR[1], a so-far unreached variety of nuclear physics experiments will be possible. In parallel, an upgrade of the existing ALADIN/LAND setup is already ongoing. The R^{3}B setup combines high-energy measurements of the most exotic nuclei with high intensities and target luminosities into a versatile next-generation setup. It comprises large-acceptance measurements in complete and inverse kinematics. Furthermore, it will be possible to study isospin asymmetric nuclei close and beyond the drip line. Basic nucleon-nucleus interactions can be studied by utilizing charge-exchange reactions, like the (p,n)-reaction. With this reaction, it is possible to study basic properties of nuclei, related to the strong and weak interaction, and it is especially suited for nuclear structure and astrophysical research.

The following sections are dedicated to a detector instrumentation work, which is an essential component of this thesis. In order to detect the recoiling low-energy neutrons of the (p,n)-reaction, a new detector is planned and first prototypes are built. The Low Energy Neutron detector Array (LENA) is characterized and basic properties are extracted. Moreover, a measurement of the neutron energy-dependent detection efficiency was performed at the Los Alamos National Scattering Center (LANSCE), and is described in a following section. Detailed GEANT3 simulations complete the description of the measurements and are used to derive the detection efficiency for neutrons with kinetic energies up to $E_{kin} \approx 6$ MeV. The results, presented here, are also published in Nuclear Instruments and Methods in Physics, see [25].

3.1 The R^{3}B experiment at FAIR

The existing radioactive beam facilities all over the world provide unique and highlighted insight into the structure of matter under extreme conditions at very exotic places in the nuclear landscape. New facilities are planned and are currently under construction. One of the upcoming next-generation facility will be the extension of the already successfully

---

[1]Facility for Antiproton and Ion Research

running GSI Helmholtzzentrum für Schwerionenforschung GmbH in Darmstadt to the FAIR facility. So far, it is one of the leading institutes in nuclear science with many different applications for fundamental nuclear research.

The already existing fragment separator FRS will be upgraded to the SuperFRS, which can produce exotic isotopes and transport them to various experimental setups, see [26]. At the final plane of the high-energy branch of the SuperFRS, the successor of the already running ALADIN/LAND setup will be situated. It utilizes Reactions with Relativistic Radioactive Beams (R³B) to extend the successfully performed studies at the existing setup to experiments with even more exotic reactions, in order to understand the nuclear structure of so-far inaccessible nuclei. The general experimental concept of the ALADIN/LAND setup will be kept and developed for further studies, however, new detector types are required to cover the big field of anticipated studies. For more information see [27].

Fig. 3.1 shows a sketch of the desired setup. It is capable of measuring reactions with exotic beams at high energies. It is adapted to use a variety of scattering reaction types, like electromagnetic excitation, knockout and breakup reactions, and light-ion elastic and inelastic scattering in inverse kinematics.
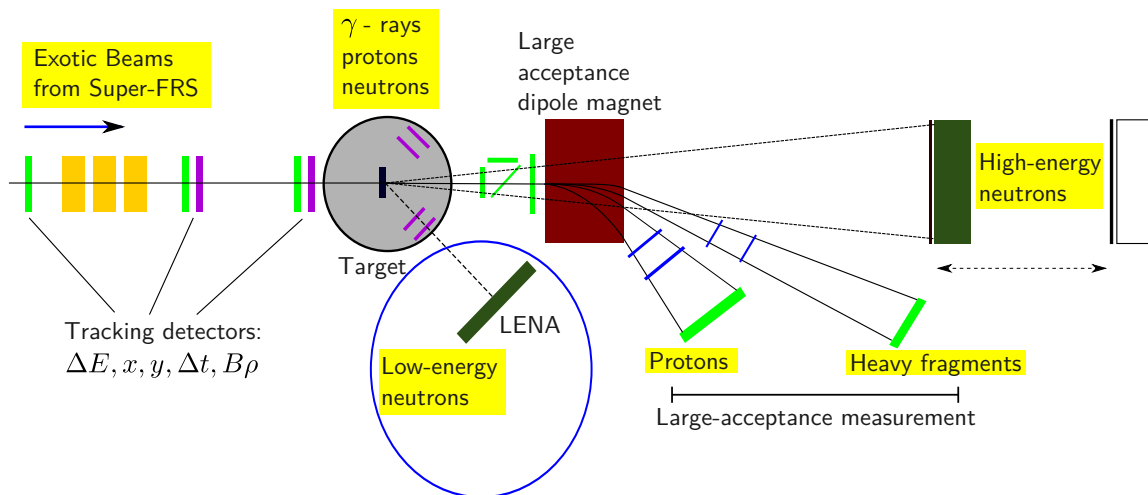
Figure 3.1: Main part of the planned R³B setup at FAIR, Darmstadt. LENA is situated downstream of the target and the position is marked in the picture. The distance to the target depends on the kinematical requirements for each experiment and will be around 1 - 2 m (not to scale).

It also provides the infrastructure allowing charge-exchange reaction studies in inverse and full kinematics. For (p,n)-type reactions, the usage of a liquid hydrogen (LH$_2$) target is anticipated, surrounded by a 4π γ-detector to measure in-flight decays of excited ejectiles. It is intended to construct a specially suited detector for detecting the recoil

neutrons of the (p,n)-reaction.

The next section describes the required properties of the detector, which can be derived from the involved kinematics.

3.2 LENA - basic considerations

In the following subsections, the general required properties for the LENA detector are derived from basic kinematical considerations. Therefore, the kinematics of a typical experimental study is deduced from two-body kinematics, yielding already the basic requirements for the LENA detector. Furthermore, the anticipated detector type and detection mechanism will be described, and measurements of fundamental properties will be presented.

3.2.1 Required properties

The properties of the anticipated detector can be derived directly from the involved kinematics, which can be viewed as a regular two-body relativistic scattering process. It is common to describe the contained variables either in the laboratory frame, which is in rest, or in the center-of-mass system. The transformation between both systems can be performed with a Lorentz transformation.

The top part of Fig. 3.2 shows the basic relation of the momentum vectors between the center-of-mass system and the laboratory system. Note, that the momentum vectors and the angles in this illustration are treated in a classical Galilean transformation, hence, there are no relativistic effects considered. However, the figure can be extended into a more quantitative presentation, shown in the bottom part of Fig. 3.2. Here, the fundamental transformation from the center-of-mass system to the lab-system is already performed and reflects the basic properties of typical two-body kinematics.

The ordinate denotes the energy of the recoiled neutron from the (p,n)-reaction, whereas the abscissa presents the behavior of the polar angle θ_{lab} of the neutron relative to the incoming beam axis measured in the laboratory. The plot is derived from a calculation, which treats a typical case of interest for a (p,n)-type reaction study in inverse kinematics. The reaction considered is p(^{56}Ni,^{56}Cu)n. It utilizes the unstable ^{56}Ni as a projectile at a kinetic energy of 300 AMeV and leaves the (Z + 1, N - 1)-nucleus ^{56}Cu as the heavy residual in the exit channel. In the reaction, a target proton undergoes a charge exchange with a neutron bound in the projectile nucleus, leaving a recoiling neutron under the conditions shown in Fig. 3.2. This case is of special interest, since it involves important isotopes present in a core-collapse supernova. Therefore, the Gamow-Teller transitions need to be known exactly and, since the nickel isotope is radioactive with a short half life ($t_{1/2} \approx 6$ d), it was never measured before. Furthermore, ^{56}Ni is a doubly-magic nucleus and it was believed, that the Gamow-Teller transitions could be different from most other nuclei. It was recently also investigated at MSU [28].
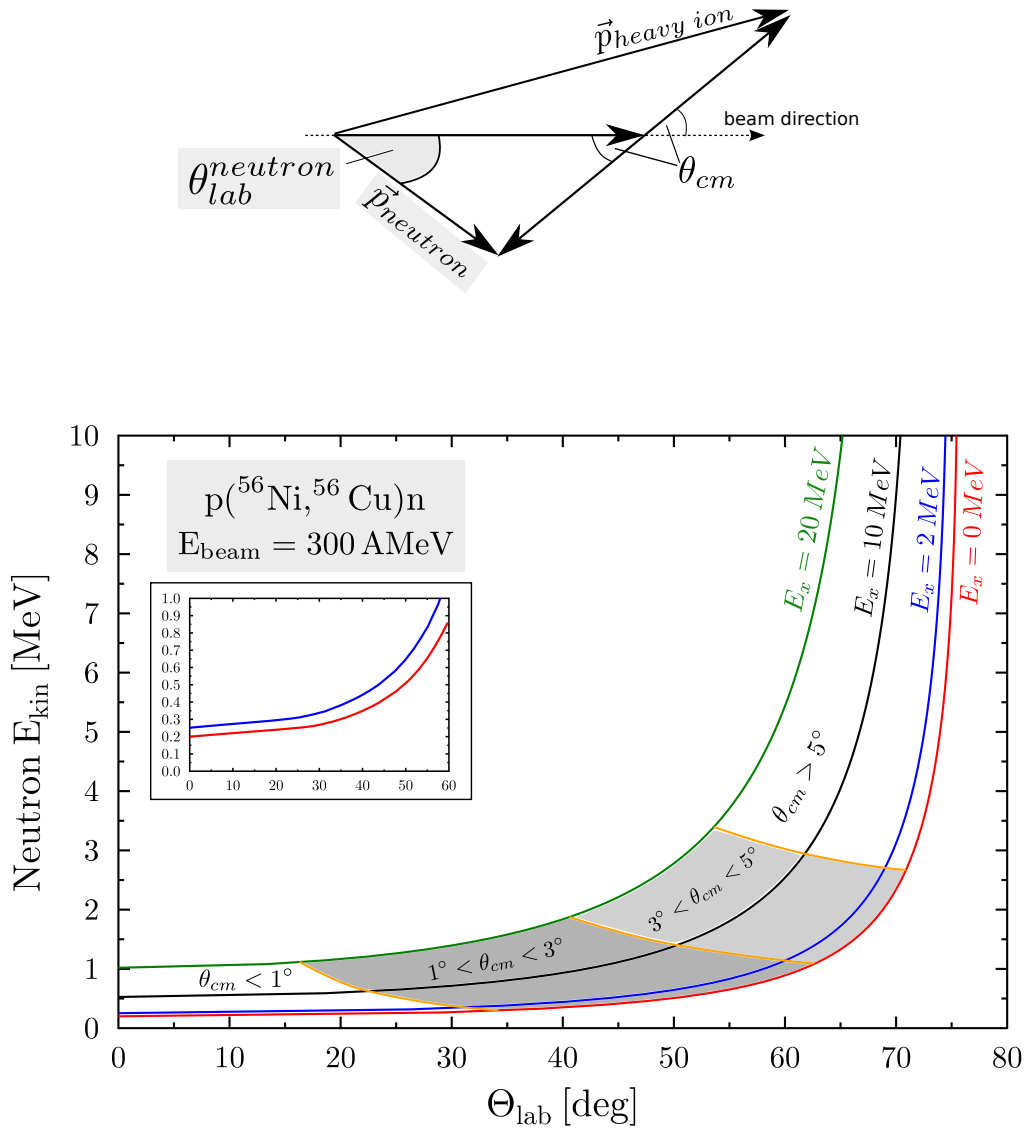
Figure 3.2: Top: Two-body kinematics, treated in a pure Galilean picture. The relation between the variables in the laboratory frame and the center-of-mass frame is shown. Bottom: Example calculation performed for the interesting reaction p(^{56}Ni,^{56}Cu)n in inverse kinematics. Different scattering angles Θ_{CM} and excitation energies E_x in the daughter nucleus are indicated in the plot, whereas the inlay shows a zoom into the two lowest excitation energies and the corresponding laboratory angles. The recoil-neutron energies are plotted on the ordinate.

In general, the anticipated inverse kinematics provide best suited conditions for the proposed studies. The transformation from the center-of-mass system to the laboratory system depends on the beam energy. As it can be seen from Fig. 3.2, at beam energies of 300 AMeV, the center-of-mass angle θ_{CM} is still small (which is required for measuring forward-scattering), but it is related to big laboratory angles up to 90°. This conceals a huge advantage, since the recoil-neutron detector can be placed at these angles and is out of way for other detectors. The setup easily allows to position a detector at around 60° around the target, thus enabling perfectly matched measurements at low momentum transfers.

Both variables, the kinetic energy and the angle, measured in the laboratory, should be extracted with good resolution, in order to derive the angle in the center-of-mass system and the ejectiles excitation energy. Fig. 3.2 clarifies, that the resolution of the measurement should be good enough to distinguish between different excitation energies. Especially the difference between low-excitation energies makes it more complex, since the detector needs to be able to resolve the different kinematical lines. Taking these considerations into account, it is clear, that the detector needs a neutron energy resolution of around 10 %, and an angular resolution of around 1° for θ_{lab}. Besides the constraints in resolution, it is necessary to build a versatile detector setup, since the angle to be covered vary from experiment to experiment.

3.2.2 LENA setup

The detection of neutrons at intermediate kinetic energies has a long tradition and different detection techniques exist. While charged particles, like protons or heavier ions, interact with the detector material via ionization, neutrons are not subject to the electromagnetic interaction. Thus, it is more difficult to detect them, since they are able to penetrate matter without any detectable effect.

In order to satisfy the above discussed requirements, several possible detector types were considered. The need for high angular resolution, high detector efficiency, and low costs left two possibilities:

(a) liquid scintillator arranged in an array

(b) organic plastic scintillation bars.

Option (b) provides easier handling and is also a common detector type in the existing ALADIN/LAND setup, thus, the second option was chosen. Basically, the neutron energy can be derived from a measurement of the neutron time of flight from the reaction point to the interaction point in the detector, considering the detector array to work similar to a time-of-flight wall. The detector paddles consist of organic plastic scintillation material of type EJ-200, which is made of Polyvinyltoluene (PVT) with the dimension of $1000 \times 45 \times 10$ mm^3. This material is a synthetic polymer with a peak in the violet-blue ($\lambda \approx 425$ nm) region of the emission spectrum of the scintillator. The

properties of the produced light are optimal for satisfying the needs of a fast timing detector. The pulse has a rise time of 0.9 ns with a pulse width (FWHM) of only 2.5 ns. This makes the material ideal for timing measurements with resolutions below 1 ns.
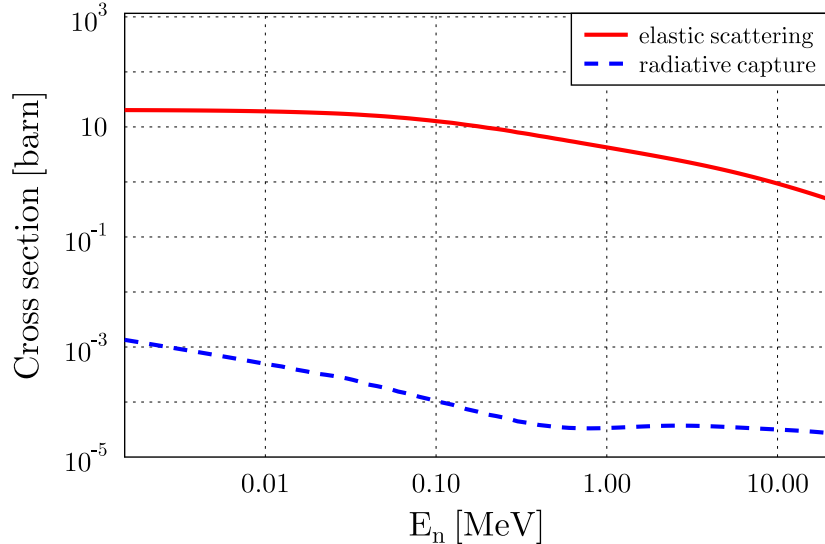

Figure 3.3: Elastic scattering and radiative capture cross sections for the interaction of the neutron in the scintillation material on protons. The main detection mechanism is the elastic hadronic scattering of the neutron on protons of the material. Other parts are negligible. Note, that in the anticipated neutron energy range from 0.01 - 10 MeV, a dramatic decrease of the radiative capture cross section can be seen.

The main detection mechanism is the hadronic interaction of the incident neutron with the scintillator material in form of elastic scattering on protons. As can be seen in Fig. 3.3, the main component of the interaction of low-energy neutrons with the protons in the material, is elastic scattering, whereas the radiative capture p(n,γ) probability on a proton is negligible, especially in the anticipated energy range of the neutrons (0.01 MeV $\leq E_n \leq$ 10 MeV). Thus, the neutron interacts with the protons of the material via hadronic elastic scattering, leading to deposition of energy, which is then transformed into scintillation light by interaction of the recoiled protons with the electrons of the molecules of the material.

However, since ionization of the surrounding matter is mediated by the protons, the occurrence of an energy *quenching* effect is unavoidable. The scintillator response is varying for different interacting particles, e.g. the light yield of an electron is much higher than for a proton. This is because of different ionization densities in the material, depending on the particle type. Still, compared to a proton, the carbon nuclei in the plastic scintillator material produce even less light, this means, they do not contribute at

all to the neutron detection process. This is also supported by the following simulations. Clearly, the *quenching* effect influences the detection efficiency, because the signal is reduced. The main challenge is subsequently to reach the lowest possible threshold, to detect neutrons also with kinetic energies below 100 keV.

The fluorescence light travels along the detector bar and is reflected at the edges of the paddle. The light losses can be substantially reduced, if the paddle is wrapped with a special foil with high reflection power. It turned out, that a multilayer polycarbonate reflector foil (3M VM2000) is highly suited for that purpose and is therefore directly attached and wrapped around the bar. In order to detect the light, two fast photo-multiplier tubes (PMTs) are optically coupled to both ends of the detector bar. The optical light passage is supported by a thin layer of silicon grease with high viscosity ($\mu = 100000$ cSt), which assures less light losses. However, the PMTs and the attached read-out electronics constrain the detection threshold, and, therefore, it is important to use PMTs with high gain in the order of 10^7 and low noise capability. Furthermore, the PMTs should provide similar timing properties like the scintillation bar, reflected in the rise time of the output signal, which should be in the range of around 1 ns.

Two PMTs from different manufacturers were tested to reach the lowest possible detection threshold. The Photonis XP2262 is a 12-stage fast PMT with a rise time of 2.3 ns and high gain of 3×10^7, see [29]. Alternatively, the Hamamatsu R2059 PMT was tested, which is also a 12-stage fast PMT with a faster rise time of only 1.3 ns with a lower gain of 2×10^7, see [30]. Different measurements, performed with both tubes, did not show any significant difference in the signal amplitudes. Hence, for the reason of availability, all further measurements were performed with the Photonis XP2262 tube.

The top left part of Fig. 3.4 shows a sketch of one single detector paddle with two attached PMTs and the dimensions. The angular resolution is determined by the dimensions of the front side of the detector, facing the reaction point in the target. However, the detection efficiency depends on the thickness, i.e. the length of the path in matter for the traversing neutron. In order to find the best suited detector efficiency at high angular resolution, two different setups are possible and shown in the top right part of Fig. 3.4. *"Setup A"* describes the arrangement with the narrow side of the detector facing the reaction point (i.e. the 10 mm side of the paddle), whereas in *"setup B"* the wide side, i.e. the 45 mm side, faces the reaction point. These expressions will be used in the further text.

Combining single detector bars to an array is the anticipated final goal. This results in a higher coverage of the solid angle and increases the overall detection efficiency. To reduce cross talk, i.e. scattering of neutrons into different detector bars, the detectors are arranged in a way shown in the bottom part of Fig. 3.4.

The single detector bars are individually tilted to face the reaction point and are arranged in a flexible holding structure, made of aluminum, to reduce the interaction probability of neutrons with the frame. The position of the individual bars inside these substructures is kept versatile and can be rearranged, depending on the proposed experiment.
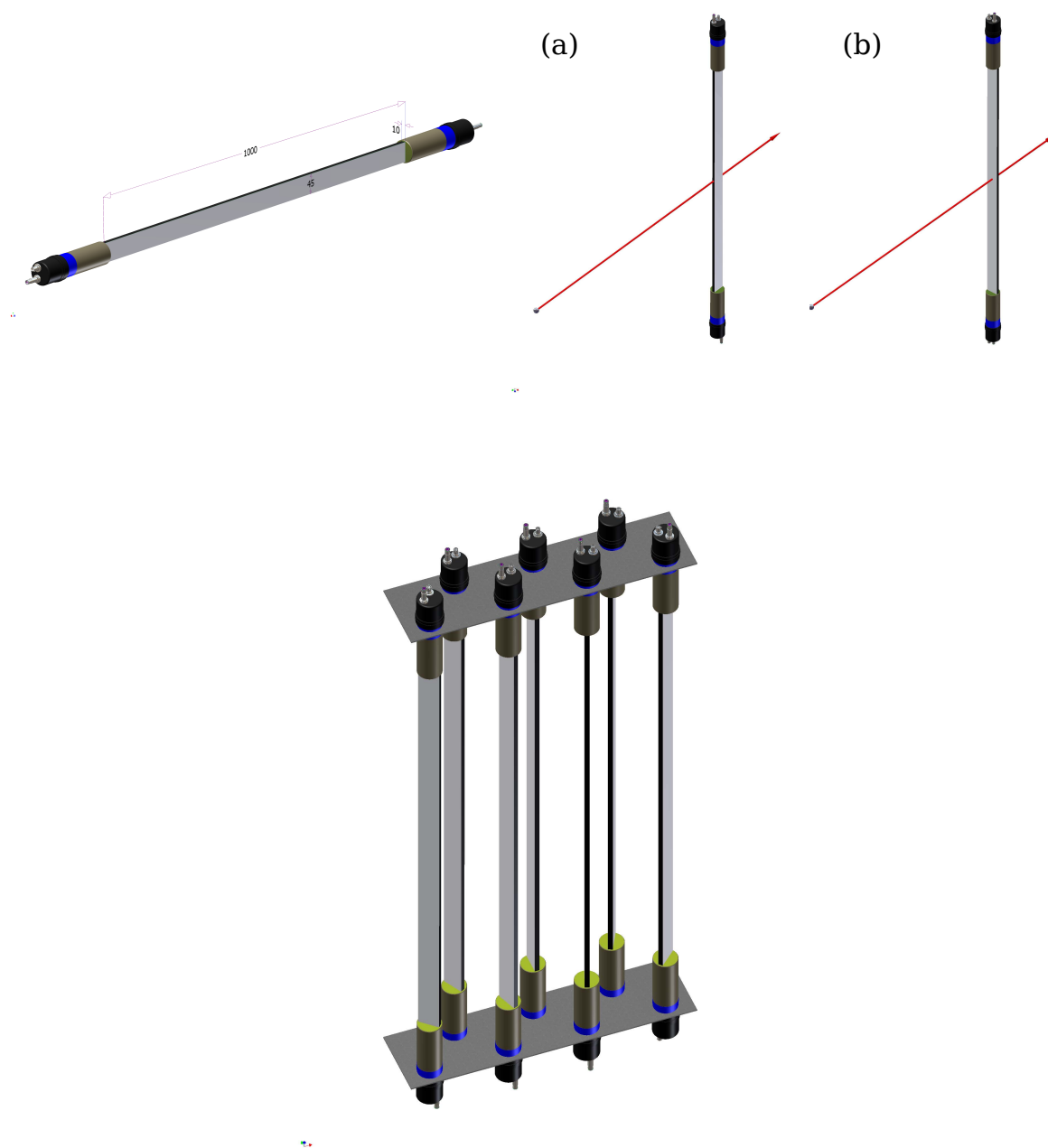
Figure 3.4: Top left: The dimensions of a single LENA detector paddle with two PMTs optically attached at each end of the paddle. Top right: Two different setups used in this thesis. In *"setup A"* the 10 mm side of the detector is facing the reaction point. *"Setup B"* denotes the situation, where the 45 mm side of the detector faces the reaction point. Bottom: One part of the LENA array. Several detectors are merged together, facing an imaginary reaction point close to the detector. The final arrangement depends on the individual proposed experiment.

3.2.3 Characteristics

A well-established model describes the transport of fluorescence light in a plastic scintillator starts from the assumption, that the light intensity $I(x)$ can be described by an exponential decay because of losses in the material. Starting with an intensity of I_0, the reduction of the light intensity is specified with the relation

$$I(x) = I_0 \cdot e^{-\lambda \cdot x}. \tag{3.1}$$

The variable x is depending on the chosen coordinate system and describes the path length, which the light has traveled. Furthermore, λ is the inverse of the optical light attenuation length, which is a material-specific property and is defined as the required path length, in which the light intensity drops to $1/e$ of the initial intensity. Basically, two independent measurements can be performed for one paddle, i.e. at each end of the detector by the PMT. Having $I \propto \Delta E$ and let e_i with $i = 1, 2$ be the measured intensity with the i-th PMT, it is

$$
\begin{aligned}
e_i &= E_0 \cdot e^{-\lambda x_i} \quad (i = 1, 2) \\
\Rightarrow e_1 \cdot e_2 &= E_0^2 \cdot e^{-\lambda \cdot (x_1 + x_2)}
\end{aligned}
$$

where E_0 is the deposited energy. The length L of the bar is fixed and defined as $L = x_1 + x_2$. By taking $e^{-\lambda \cdot (x_1 + x_2)}$ as a constant, it finally results in

$$E_0 \propto \sqrt{e_1 \cdot e_2}.$$

With this relation, it is thus possible to measure the quenched deposited energy of the neutron in the material without a position-dependent effect. To measure the optical light attenuation, a γ-emitting radioactive source is used, which is placed on the detector and moved step-by-step by an exactly known distance along the bar. By measuring the light intensity at one PMT, it is possible to extract the optical light attenuation. The manufacturer Eljentechnology states an attenuation length of 400 cm ($\lambda = 0.0025$ cm^{-1}), which is usually given for a huge piece of the material, see [31]. The light attenuation length should be reduced, since reflections at the edges of the paddle influences the light transportation drastically.

A collimated ^{60}Co source was placed in steps of 10 cm from one PMT, where the light intensity was measured. The top part of Fig. 3.5 shows the result of the measurement. A logarithmic fit, according to the above mentioned formula, is applied and fits the data well. Errors shown stem from the inaccuracy of the position measurement, combined with the resolution of the measured light intensity.

The extracted slope of the exponential function corresponds to the inverse of the optical light attenuation length and is found to be

$$\lambda = (0.0100 \pm 0.0003) \text{ cm}^{-1}.$$
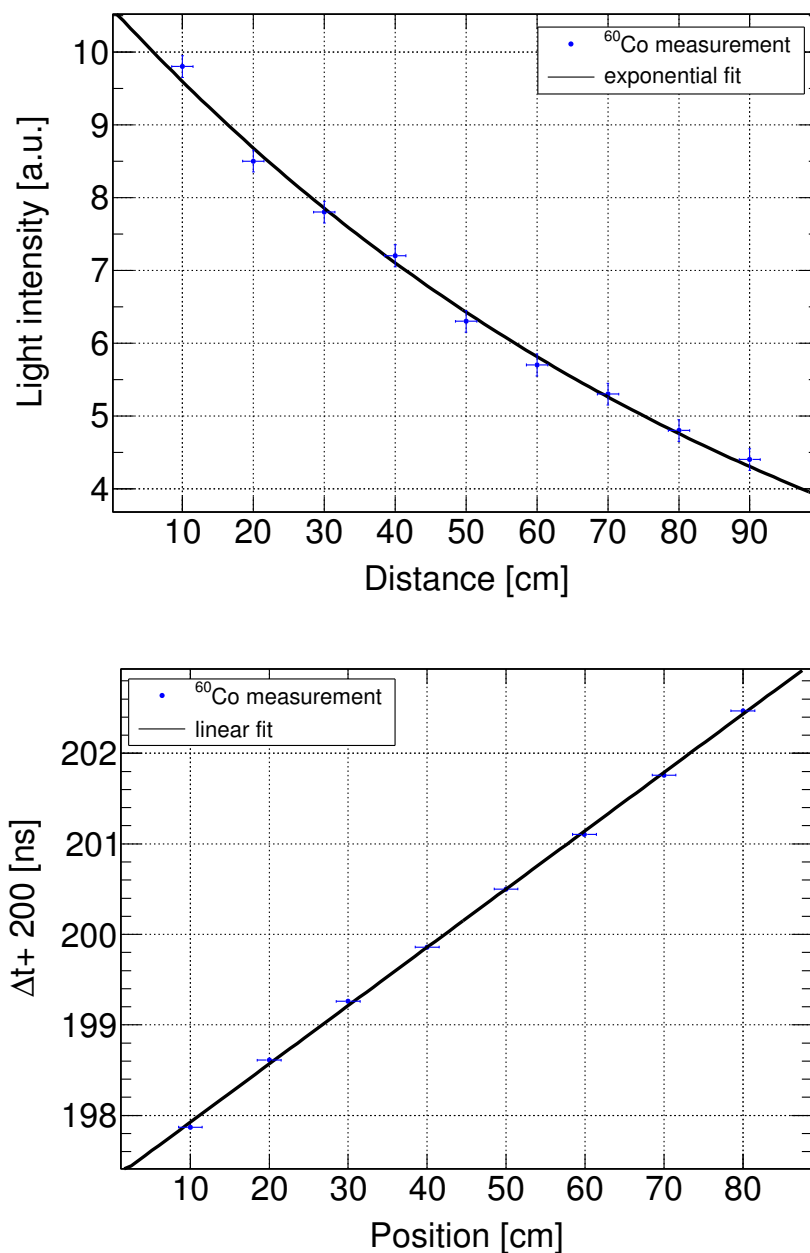
Figure 3.5: Top: The Compton edge of the ^{60}Co source is used to find Q_1 for different distances to the PMT. Assuming an exponential reduction of the light intensity, it is possible to extract the optical light attenuation length, which results in (100 ± 3) cm. An exponential fit to the data is shown (solid line). Bottom: The speed of light in the paddle is measured by moving the same source along the paddle, and by extraction of the time difference between the two PMTs. A linear fit to the data is shown (solid line).

This results in an attenuation length of (100 ± 3) cm.

Because the energy of the scattered proton depends on the number interactions of the neutron in the detector it is not possible to extract the neutron energy with this method. Thus, in order to extract the energy of the neutrons, it is necessary to make use of the measured incident time of the neutrons, i.e. to use the detector as a time-of-flight device. The time measurement is important for two reasons. First, it can be used to measure the time of flight from a start detector to the LENA detector. Secondly, it is possible to extract the position of the hit on the paddle, which is needed, since the neutron could also be scattered into the kinematical azimuthal angle ϕ. This would correspond to a vertical hit position on the detector and results in a longer flight path. Hence, it is important to identify the position on the detector, which can be performed by taking the speed of light in the paddle and the time difference of both PMTs into account.

In order to measure the effective speed of light c', again the collimated ^{60}Co source is utilized and positioned along the paddle step by step. The arrival time of the light at both ends is measured with the attached PMTs and by subtracting the times, it is possible to extract the effective speed of light c' in the paddle, via

$$x_i = c' \cdot t_i \quad (i = 1, 2)$$
$$\Rightarrow \frac{(x_1 - x_2)}{\Delta t} = c',$$

where $(x_1 - x_2)$ are the distances x_i from the PMT and Δt is the measured time difference. The bottom part of Fig. 3.5 shows the measured spectra and the expected linear fit. The ordinate is arbitrarily shifted by 200 ns for readability reason. The inverse of the slope of the linear fit results in the effective speed of light in the paddle, which is extracted to be

$$c' = (15.5 \pm 0.1) \text{ cm/ns.}$$

However, measuring the neutron energy with the time-of-flight method requires a sufficiently good timing resolution of the detector. As mentioned above, the anticipated time resolution should be less than 1 ns. The resolution was measured with a collimated ^{60}Co source, placed on the center of the bar. It is measured to be $\sigma_t = 0.52$ ns. Assuming a similar time resolution for both PMTs, the time resolution for one side results in $\sigma_t = 0.37$ ns. Fig. 3.6 shows the corresponding measurement and a Gaussian fit. Taking the measured speed of light in the paddle and the extracted time resolution into account, it is possible to calculate the expected position resolution along the detector bar. It results in $\sigma_{\text{position}} \approx 6$ cm.

The time-of-flight measurement and the subsequent extraction of the energy of the neutron is related by

$$E_n^{kin} = 0.5 \cdot m_n \cdot \left(\frac{s}{\Delta t}\right)^2, \hspace{3cm} \boxed{3.2}$$
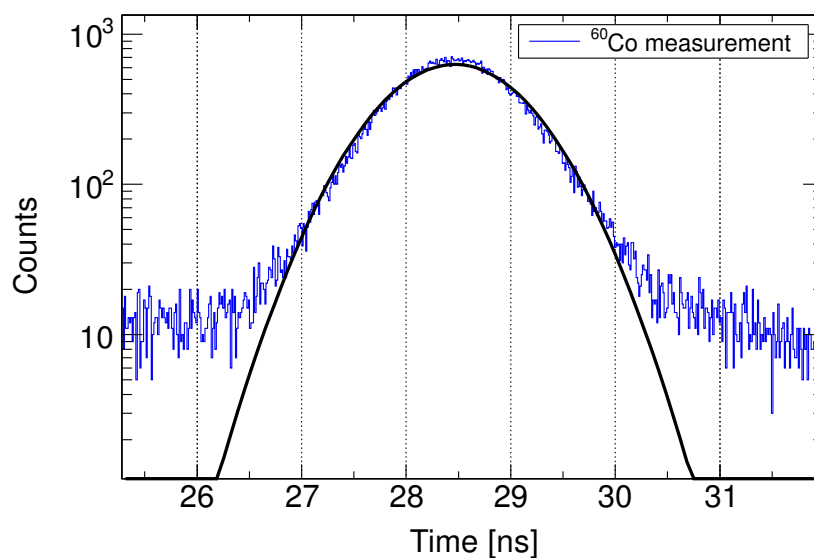
Figure 3.6: Measurement of the time resolution with the ^{60}Co source in the middle of the module. The FWHM is about 1.23 ns for the time difference. Assuming a similar resolution for the two ends, the time resolution for one side results in 0.87 ns (FWHM).
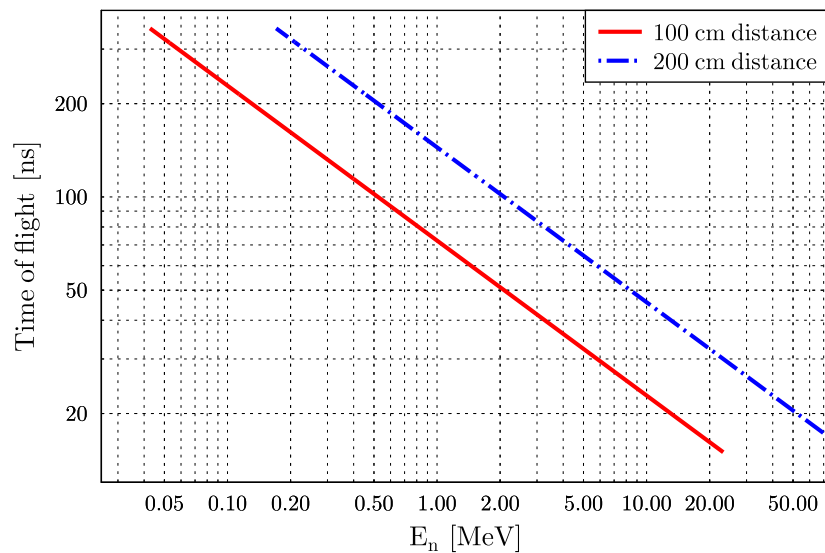

Figure 3.7: Non-relativistic neutron kinetic energy and time-of-flight dependence for two different distances of the detector to the reaction point. Note, that both axes are plotted in logarithmic scale. The plot is derived from formula 3.2.

where s is the distance between the LENA array and a start detector, m_n the neutron mass and Δt the measured time. The distance depends on the required energy resolution, in order to resolve different excited states in Fig. 3.2. However, the distance also influences the coverage of the solid angle. Therefore, a compromise between the two variables should be aspired. A typical distance for the beam energies achievable at the R^{3}B setup would be $s \approx 100$ cm.

Fig. 3.7 shows the dependency of the measured time of flight on the neutron energy E_n for two different distances between the start detector and the LENA array. The distances are chosen to be 100 cm and 200 cm, respectively. At low neutron energies, the non-relativistic formula 3.2 for E_n^{kin} is sufficient and describes the experimental situation well.

3.3 Simulations and measurements

In order to understand the detector response in a qualitative way, detailed simulations with the GEANT3 package[2] were performed, see [32]. In the first part of this section, the basics of the simulations are described. Furthermore, these simulations were used to simulate the detector response to γ- and X-ray sources. The results are compared to the corresponding measurements showing excellent agreement.

3.3.1 GEANT3 simulations

GEANT3 is a program package provided by CERN to simulate the passage of elementary particles through matter. Different interactions are implemented and measured cross sections are involved, in order to achieve high reliability. The simulations were performed with the package version 3.21 and the linked GCALOR[3] interface [33], which includes the MICAP[4] interface, see [32]. This package is especially suited for simulation of the interaction of neutrons in matter with kinetic energies below 20 MeV and is based on measured and calculated cross sections.

The simulations, performed in the framework of this thesis, are restricted to one single detector bar. GEANT3 tracks the started particle in small steps and calculates the energy loss and other quantities for each individual step. Thus, it is possible to retrieve the total deposited energy of a traversing neutron in a scintillation material.

In general, GEANT3 is not calculating the energy quenching effect, described above, automatically, neither the light propagation in the material. Therefore, the simple light tracking algorithm is applicable, in order to track the light to both ends. This simulates the light intensity (with $I \propto \Delta E$), read out by the two PMTs. The basic relation is given in formula 3.1, with λ being the inverse of the measured optical light attenuation

---

[2]GEometry ANd Tracking
[3]Geant Calorimeter
[4]Monte-carlo-Ionization-Chamber-Analysis-Program

length (see section before). Since the quenching effect is not taken in account, it is heuristically implemented into the simulation code. The quenching effect relates the recoil-proton energy in the material (originating from elastic scattering of the neutrons) to the light output, produced by the interaction of the recoil-protons with the electrons of the material. Therefore, a formula, given by Cecil et al. (c.f. [34]), is used and fitted for the low energy part of the recoil-protons for easier handling. This formula uses material-dependent coefficients and is for the case of the LENA detector

$$E_{ee}(E_p) = 28 \cdot E_p^2 + 0.215 \cdot E_p.$$

This conversion between the proton energy E_p and the electron-equivalent energy E_{ee} is used in the simulation and is valid under the assumption, that protons are fully stopped in the material. It is possible to implement a threshold, depending on the condition, if the light intensity is above or below the specified value. However, this is only true under the assumption, that there are no losses from the PMTs and the attached electronics, which definitely affects the final digitized charge and time.
Furthermore, two simplifying assumptions are made, in order to reduce the complexity of the calculations.

(a) It was not checked for each event, if the protons are actually fully stopped in the material. The assumption is, however, justified by a calculation with SRIM, which clearly shows, that a proton with an energy of $E_p = 10$ keV or $E_p = 2$ MeV is fully stopped in the material already after ≈ 0.2 μm and ≈ 69.4 μm, respectively.

(b) In order to take the low interaction probability and low energy deposition (i.e. due to high quenching) of the carbon atoms in the material into account, the calculation neglects the interaction on carbon nuclei, and instead, it treats it in the same way like for protons. In particular, at low incident neutron energies, the carbon only produces light above the threshold, if it is re-scattered on a proton.

3.3.2 Response to γ- and X-rays

Several measurements with γ- and X-ray sources, available at GSI and the University of Frankfurt, were performed to extract basic properties of the detector and to constrain the simulation to the measured data. In total, the simulation is able to reproduce the response of the detector very well and works in different energy regimes reliably good.
In order to simulate the response of the detector to γ- and X-rays, the decay properties of the sources are correctly implemented into the simulation code. Furthermore, the intrinsic resolution of the detector is folded with the resulting spectrum, following the typical $\sigma \propto 1/\sqrt{\Delta E}$ characteristics of the energy resolution

$$\sigma = \frac{3.4 \cdot 10^{-2}}{\sqrt{\Delta E}} \left[\frac{1}{\sqrt{MeV}} \right]$$
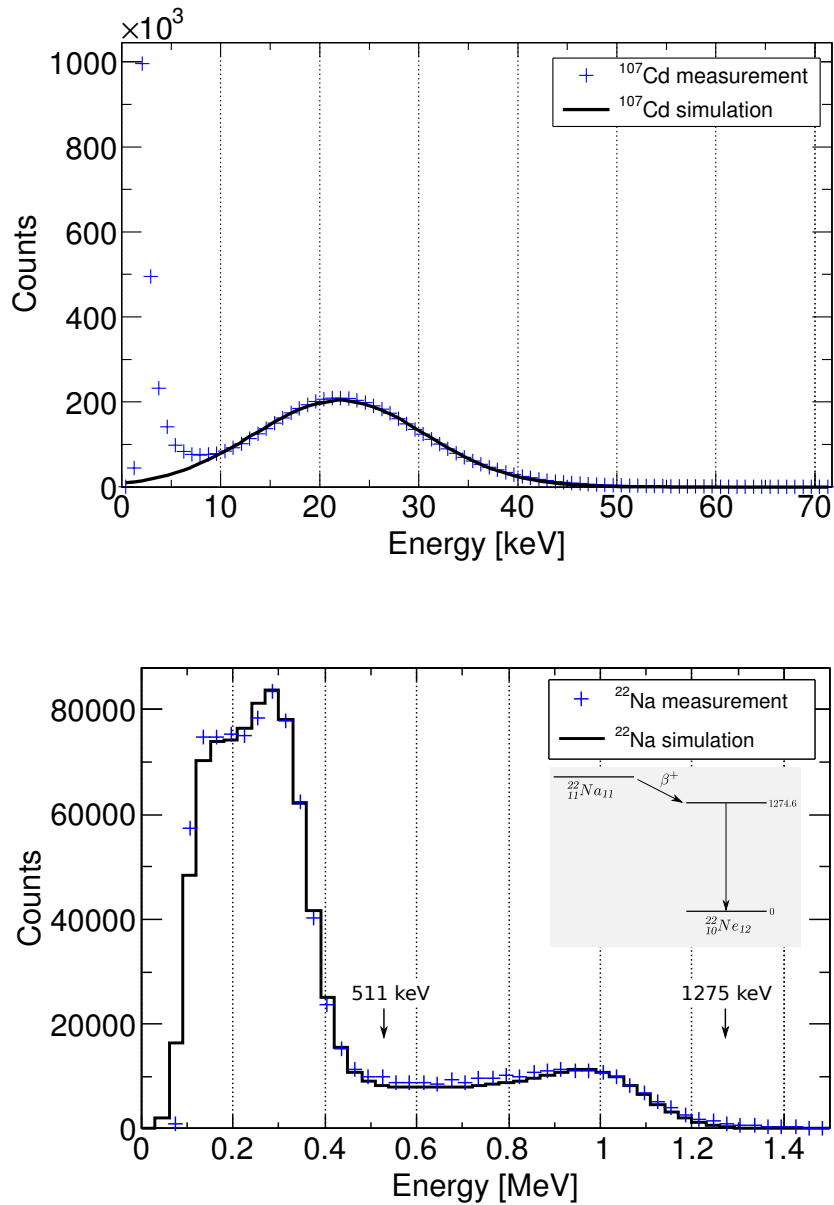
Figure 3.8: Top: Measurement of the low-energy γ-ray at 22 keV following the decay of ^{107}Cd and comparison with a GEANT simulation. Below $\approx$ 10 keV, the experimental spectrum is dominated by electronic noise. Bottom: Measured and simulated response to γ-rays emitted in the decay of ^{22}Na. The positions of the Compton edges of the two emitted γ-ray photons at 511 keV and 1275 keV allow the energy calibration of the setup.

for the LENA detector.

The top part of Fig. 3.8 shows a measurement with a ^{107}Cd source attached to the center of the detector bar. The strong peak at around $E_\gamma \approx 22$ keV is produced by the X-rays following the decay of ^{107}Cd and is described by the simulation (black line). The low-energy region below 10 keV is dominated by electronic noise in the measurement with a charge-to-digital converter (QDC).

The bottom part of Fig. 3.8 shows a measurement and the corresponding simulation of the detector response to the decay of ^{22}Na. This isotope decays via β^+-decay, meaning ^{22}Na $\longrightarrow e^+ + \nu_e + {}^{22}$Ne and produces two γ-rays of 511 keV by annihilation of the positron in the material. Furthermore, the decay to the ^{22}Ne ground-state proceeds via emitting a γ-ray from the 1274.6 keV level in ^{22}Ne. The γ-rays can be detected with the detector and interact mostly via Compton scattering in the detector material. This produces the two Compton edges in the spectrum. Both of them are perfectly reproduced with the simulation.

In general, all simulations showed excellent agreement, proving, that for the electromagnetic interaction, the code works well.

3.4 Efficiency studies for neutrons

The detector will be used in (p,n)-type charge-exchange reactions. Therefore, it is necessary to understand the detector response to neutrons. Of special interest is the detection efficiency, since this is an important ingredient for the determination of the cross section for different excitation modes.

In order to understand the details of the detection efficiency, a measurement with an intense neutron beam was performed at the Los Alamos Neutron Scattering Center (LANSCE) in New Mexico, USA. In this section, the general setup is described, followed by the analysis and the results of the experiment. Again, the simulations are employed to describe the experimental results and they show excellent agreement.

3.4.1 Setup and analysis

One detector bar was taken to the Los Alamos Neutron Scattering Center in order to measure the response of the detector to an incident neutron beam. The facility provides different experimental areas, situated around a tungsten neutron production target, enabling the usage of pulsed neutron beams to perform time-of-flight measurements. Therefore, a white neutron spectrum is produced by spallation processes, initiated by a 800 MeV proton beam penetrating the tungsten target. The proton beam currents reach up to 135 μA and thus, high intensity neutron beams with energies from the thermal region up to several hundreds of MeV are produced. Fig. 3.9 shows the schematic setup of the facility. The experiment was performed at flight path 5 (FP5) with a distance of 9 m to the primary production target. A fission chamber for flux measurements,

equipped with a thin ^{235}U foil, was placed at the entrance of the experimental setup, viewing a lower-tier moderator. The flux is very high (100 neutrons/s/cm^2/eV in the energy region between 10 and 500 keV) at this small-distance experimental area. The beam spot size was restricted to a diameter of around 1 cm by arranging paraffin blocks in the main beam line.
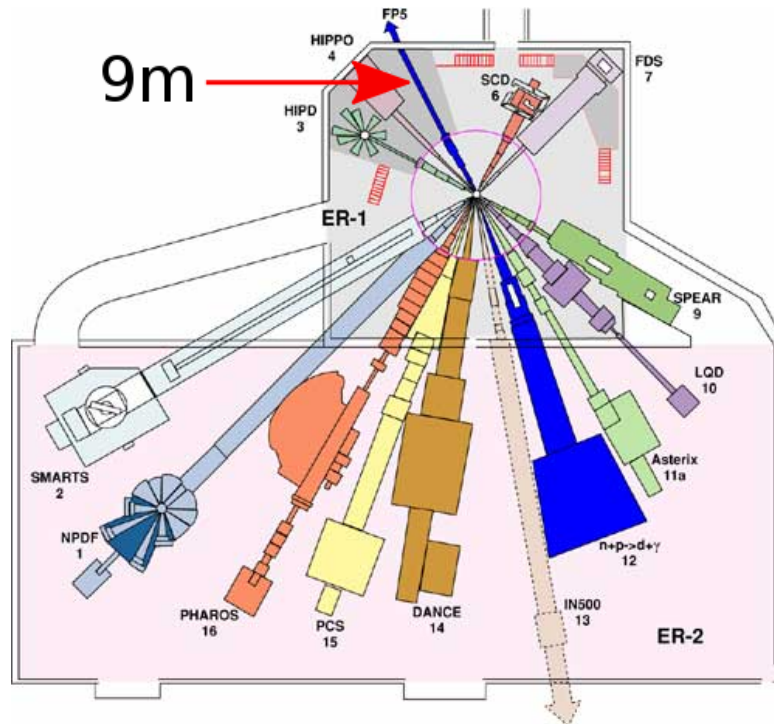
Figure 3.9: Different flight paths situated around the tungsten target at the Los Alamos Neutron Science Center (LANSCE). Protons at 800 MeV are used to create spallation neutrons while impinging on the tungsten target. The experiment, described in this chapter, was performed at the shortest flight path FP5, marked in the picture (not to scale). Picture adapted from [35].

In order to avoid the strong interaction of the detector with the intense primary neutrons and the huge γ-flash, produced in the spallation process in the tungsten target, the detector was placed at a distance of 1 m off the primary beam line. Moreover, a double time-of-flight technique is employed to measure the neutron response of the LENA detector. Since it was placed outside the primary beam line, it was possible to utilize the fission neutrons produced in the ^{235}U foil in the fission chamber. ^{235}U is highly fissile and thus, a sufficient amount of secondary neutrons was produced by the primary neutrons in the thermal region, where the fission cross section of ^{235}U is high. At these primary neutron energies, the average number of secondary neutrons produced per fission event

(denoted by $\bar{\nu}$)) accounts to $\bar{\nu} = 2.42$ [36]. They are emitted into the full solid angle. In total, two time-of-flight measurements are performed, which are

(1) Blocking the data acquisition system, until the very late primary neutrons (having low energies) in the pulsed neutron beam reached the fission chamber. Subsequently, 2 ms after the start pulse, delivered from a pickup detector situated before the tungsten target and triggered by the passage of the protons, a time window of 3 ms was opened, in which the neutron energies in the thermal region between 17 - 70 meV are highly suited to trigger fission events in the fission chamber.

(2) Measuring the time of flight for a registered event in the fission chamber to the neutron detector during the opened primary time window.

The top part of Fig. 3.10 shows a sketch of the setup. The bar faces the fission chamber with its narrow side (*setup A*) to maximize the interaction probability for the fission neutrons.

The read-out was based on flash analog-to-digital converters (FADCs). The Acqiris model DC265 transient digitizer (Agilent Technologies SA, Geneva, Switzerland) was used. It is utilizing an internal 8-bit digitizer at a maximum sampling rate of 500 MS/s (million samples per second). This corresponds to one sample every 2 ns. The module is read-out with a PC, connected via PCI standard bus. The bottom part of Fig. 3.10 shows a sketch of the electronic setup.

If fission events, detected in the fission chamber, triggered the data acquisition, the entire waveform of both PMTs and the chamber were recorded for 2 μs, ensuring, that the complete time range is covered. Fig. 3.11 illustrates two different recorded waveforms, triggered by a signal in the fission chamber.

The analysis of the experiment can thus be performed offline without any loss of data. This is a big advantage of FADCs. All waveforms are saved and hence, it is possible to set individual thresholds and algorithms for the time and for the charge information. Fig. 3.11 shows a typical analysis step. An internal software constant-fraction discriminator is used to extract the time of flight of the neutrons to travel from the fission chamber to the neutron detector. It is possible to employ an user-written charge-to-digital converter, which can also be seen in Fig. 3.11. This is a powerful analysis feature and enables the extraction of a time of flight on an event-by-event basis without losing any information. A multiplicity variable is used to store the amount of waveforms detected in one time frame of the read-out time.

3.4.2 Results and simulations

In order to understand the detector response to the incident fission neutrons, a simulation was employed. Main focus of the simulation is not the deposited energy, but rather the measured time of flight from the fission chamber to the detector. Therefore, it is necessary to use a realistic energy distribution for the fission neutrons, in order to simulate their correct characteristics. The distribution is derived from the ENDF database,
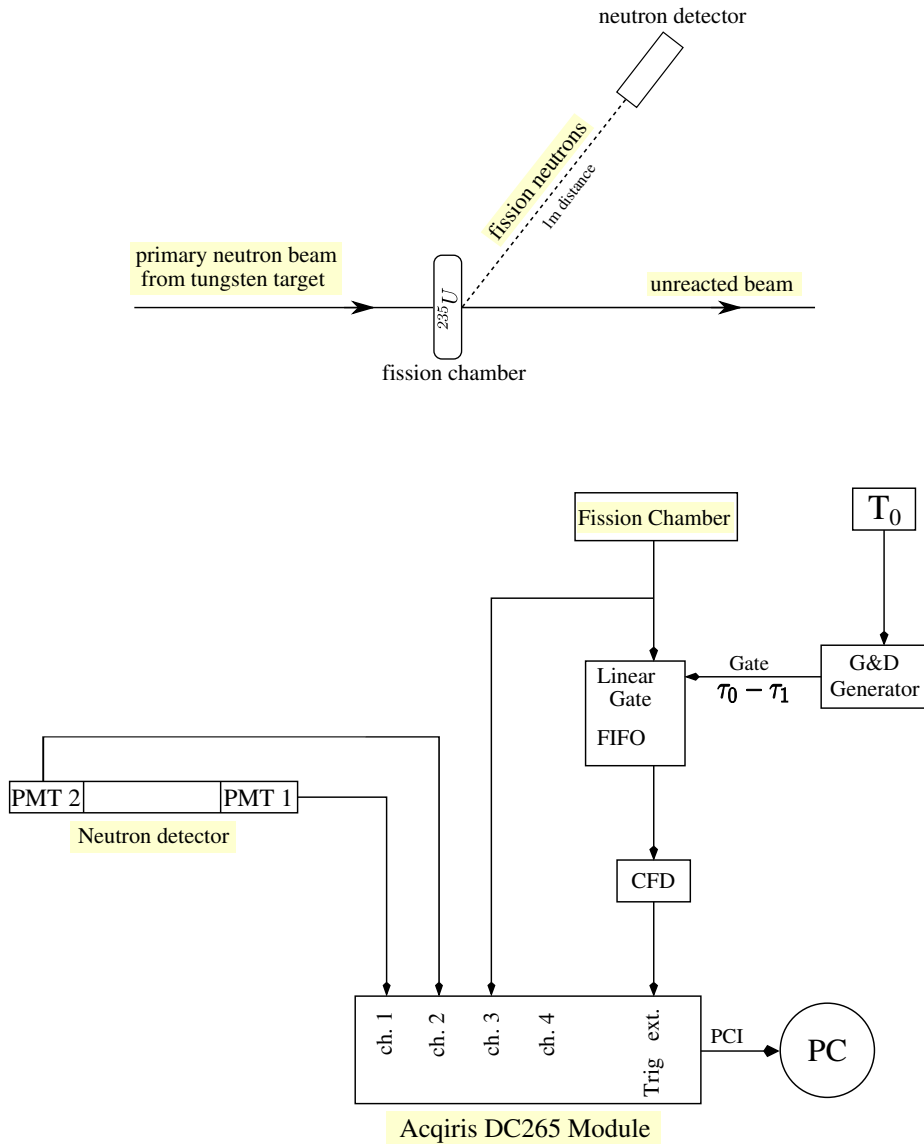
Figure 3.10: Top: Sketch of the geometrical setup during the neutron efficiency calibration at LANSCE. Bottom: Sketch of the electronic setup during the neutron efficiency calibration at LANSCE. See text for further details.

which contains evaluated and recommended data for incident neutron reactions, see [36]. Fig. 3.12 shows the energy distribution of fission neutrons from ^{235}U($n_{thermal}$,f).
The distribution is used to simulate the fission neutron energies by randomly choosing a neutron energy with the corresponding probability, which is proportional to the differential cross section in the figure.
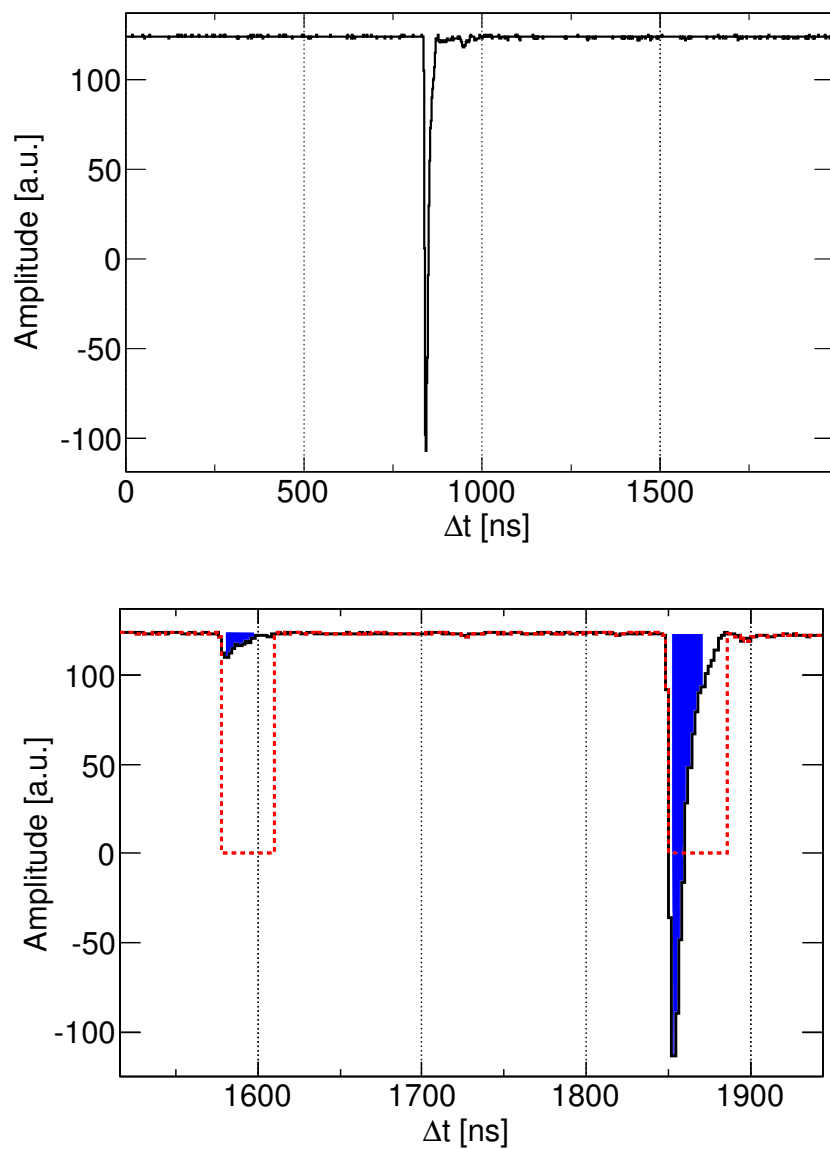
Figure 3.11: An user-written constant-fraction discriminator (red color) and an integrator (blue color) were used to extract the time of flight and the energy deposition.
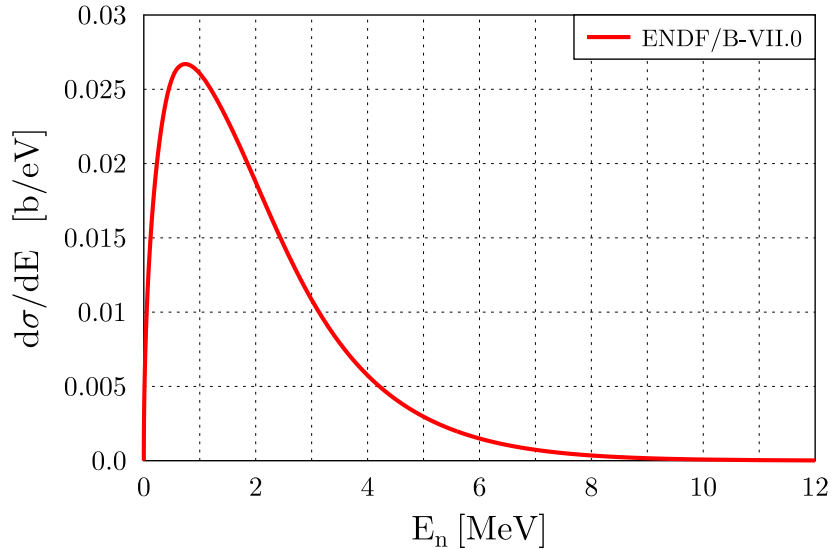
Figure 3.12: Energy distribution of the fission neutrons produced in the ^{235}U(n$_{thermal}$,f) reaction. The incident neutron energy is $E_{inc} = 10^{-5}$ eV. The distribution is used in the code for a realistic simulation of the experiment. The data is taken from the ENDF/B-VII.0 database [36].

The neutron source was placed at a distance of 1 m, as in the actual experiment. Furthermore, the γ-rays, produced in the fission process, are simulated as well and are emitted into the full solid angle. For the simulation of the timing characteristics of the detector, only the first interaction point is considered and used to extract the time of flight. The spectrum of the γ-rays is folded with the intrinsic resolution of the detector, which was found earlier. In order to simulate the response for neutrons for this particular experiment at LANSCE, the same amount of neutrons, measured with the fission chamber, were simulated, i.e. 1.7×10^8 neutrons.

Fig. 3.13 shows the measured time-of-flight spectrum compared with the simulation. The inlay shows a zoom into the time-of-flight spectrum. In both figures, the simulation fits the measured data very well, which is also valid for the strong γ-peak at the beginning of the spectrum. This again shows the reliability of the simulations, and it seems, that even the interaction of low-energy neutrons in the material is described very well and can be used, to reproduce the measured data.
Obviously, at neutron energies below 200 keV, the spectra is distorted and is not fitting the simulation anymore. However, this effect can be explained by taking the background in the small experimental area into account. The surrounding concrete walls were very close to the detector and thus, e.g. scattered primary neutrons and γ-rays from late neutron captures in the walls, dominate the measurement. The simulation of a realistic
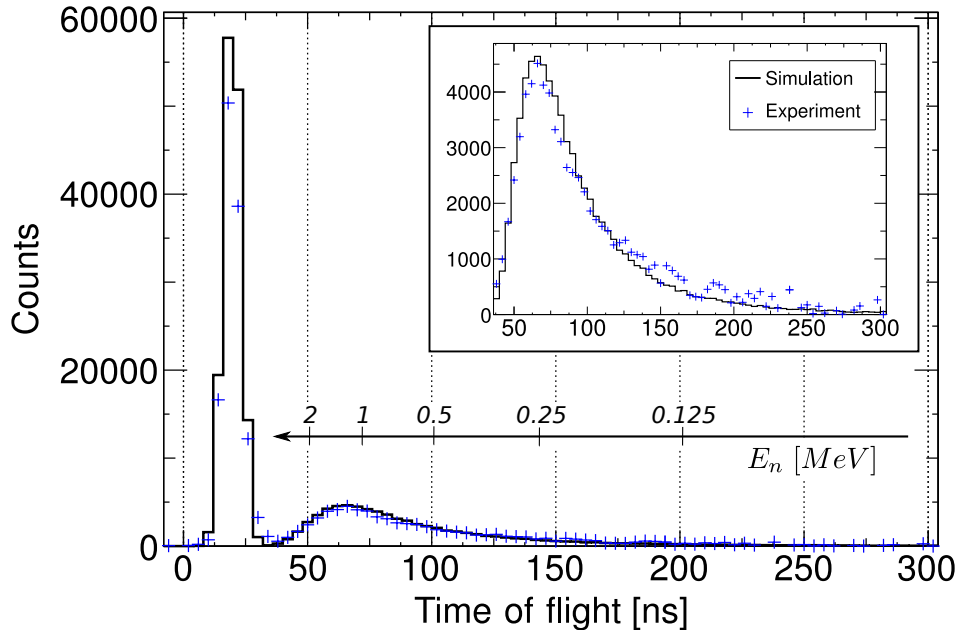
Figure 3.13: The time-of-flight spectrum for the fission neutrons including the strong
γ-peak from prompt fission events, measured with one LENA detector
bar. Furthermore, a simulated time-of-flight spectrum, produced with the
GEANT3 simulation, is shown (solid line). Both spectra show excellent
agreement. The inlay is a zoom into the time-of-flight region corresponding
to neutron events. Neutron energies are indicated.

background would require a very detailed knowledge about the setup, and is a time-
dependent effect, which is difficult to simulate.

However, the simulation agrees very well with the measurement. In a final step, the
simulations are employed to extract the detector response to mono-energetic neutrons,
describing an ideal case without any distortions. The next chapter describes the results
of the simulations.

3.5 Efficiency simulations

Based on the performed detailed simulations, it is possible to describe the measurements
with γ- and X-ray sources very accurately. Furthermore, the measurement performed at
the Los Alamos Neutron Scattering Center (LANSCE) with secondary fission neutrons,
triggered by primary thermal neutrons on ^{235}U, can be reproduced with the simulations
very well. This shows, that the principal response of the detector can be described with
the simulation. This enables the usage of the simulation to extract a neutron energy-

dependent detection efficiency.

The simulations allow the determination of the response to mono-energetic neutrons without any surrounding material. This ideal case delivers the upper limit of the efficiency by not taking any effects of the attached electronics or background into account. In order to simulate the detector response to neutrons, the two different setups, mentioned in Fig. 3.4, are taken into account, where "setup A" describes the situation, when the neutron hits on the narrow side of the detector, and "setup B" is used, when the neutron hits the wide side of the detector.

An important ingredient is the implemented lowest detection threshold, which simulates the detection threshold of the attached electronics. In order to incorporate this into the simulation code, the deposited energy is converted into light output and tracked to the ends of the detector bar. In the efficiency simulation, the incident point is in the middle of the detector bars, meaning a distance of 50 cm to each end. Furthermore, if the tracked light intensity is too low to overcome the threshold at both sides, the event is discarded and not taken into account. The requirement, that both PMTs have to register an event above threshold, is also applied in real experimental situations to suppress electronic noise, coincidences with cosmic rays, and background.

However, the relation between the number of incident neutrons and the efficiency ϵ is given by

$$\epsilon = \frac{n_{det}}{n_{inc}},$$

with n_{inc} being the total number of simulated neutrons hitting the detector and n_{det} is the number of neutrons producing enough light to pass the given threshold.

In total, 6 thresholds are implemented in the simulation (10 - 50 keV, 100 keV). In a real experimental situation, the aim is to reach the lowest possible threshold, just situated above the single-electron noise of the PMT. At the lowest threshold of E_{ee} =10 keV, it is possible to reach an efficiency of more than 60 %, using the detector in *setup A*. If a high angular resolution is not required for a certain experiment, the detectors can be arranged in the way shown in "setup B", which favors a higher coverage of the solid angle, but suffer a loss of efficiency (for the lowest threshold, the maximum efficiency reached is $\epsilon_{max}^{10keV} \approx 20$ %).

The result can be compared to a similar detector built at the Forschungszentrum Dresden-Rossendorf. Their detector size of $1000 \times 42 \times 11$ mm^3 is comparable to the dimensions of LENA. In total, an efficiency of (20 ± 3) % for neutron kinetic energies in the range of 200 - 600 keV with a detector of 11 mm thickness was found. The simulations performed in the framework of this thesis show an efficiency of (19 ± 1) % for the same energy region. Thus, they agree very well and again demonstrates the good description of the interaction within the GEANT3 simulation code.
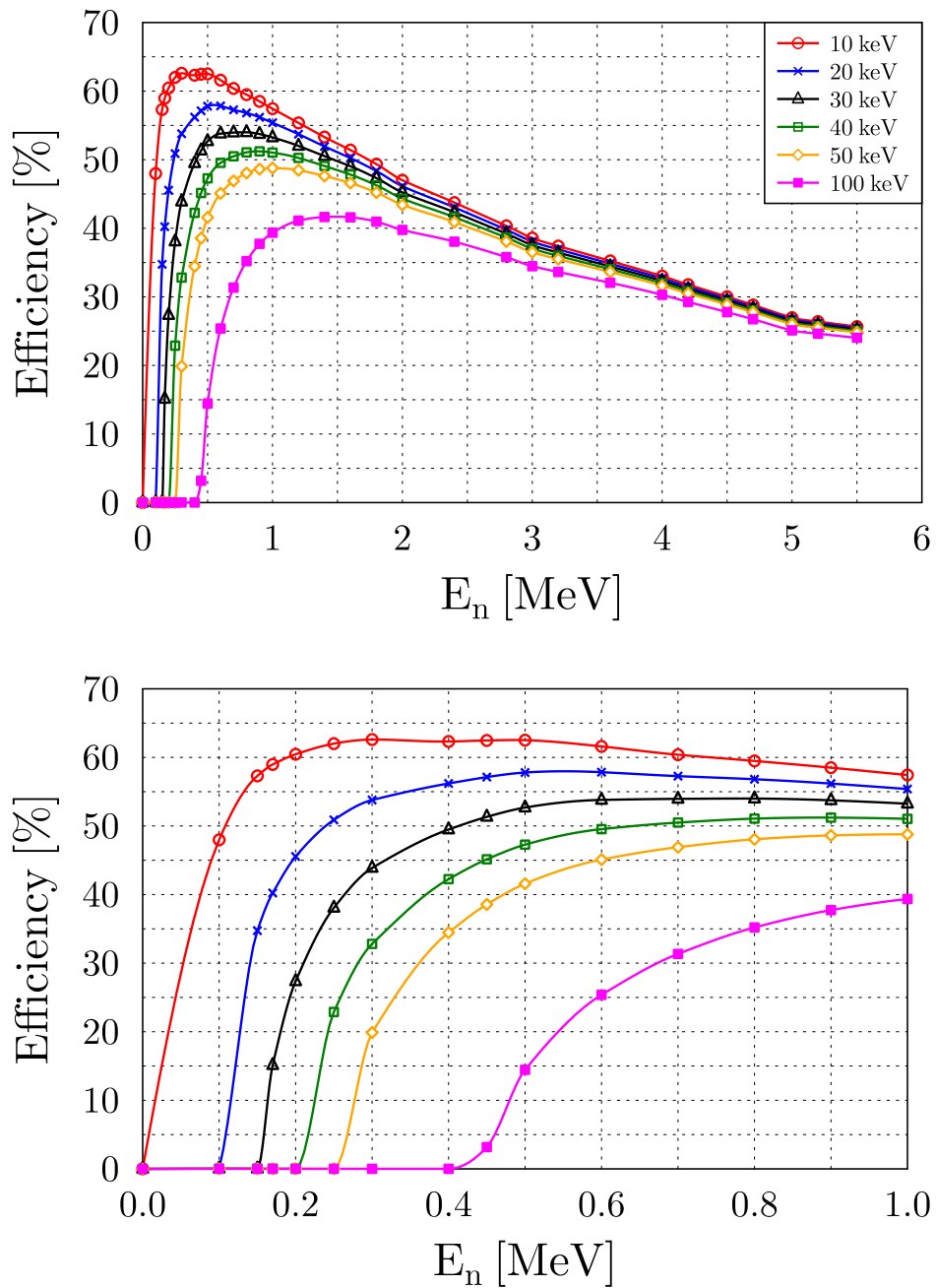
Figure 3.14: Simulated response of a LENA bar to mono-energetic neutrons for *"setup A"*. The plot in the bottom is a zoom of the 0 - 1 MeV region of the plot shown in the top. Detection thresholds are indicated.
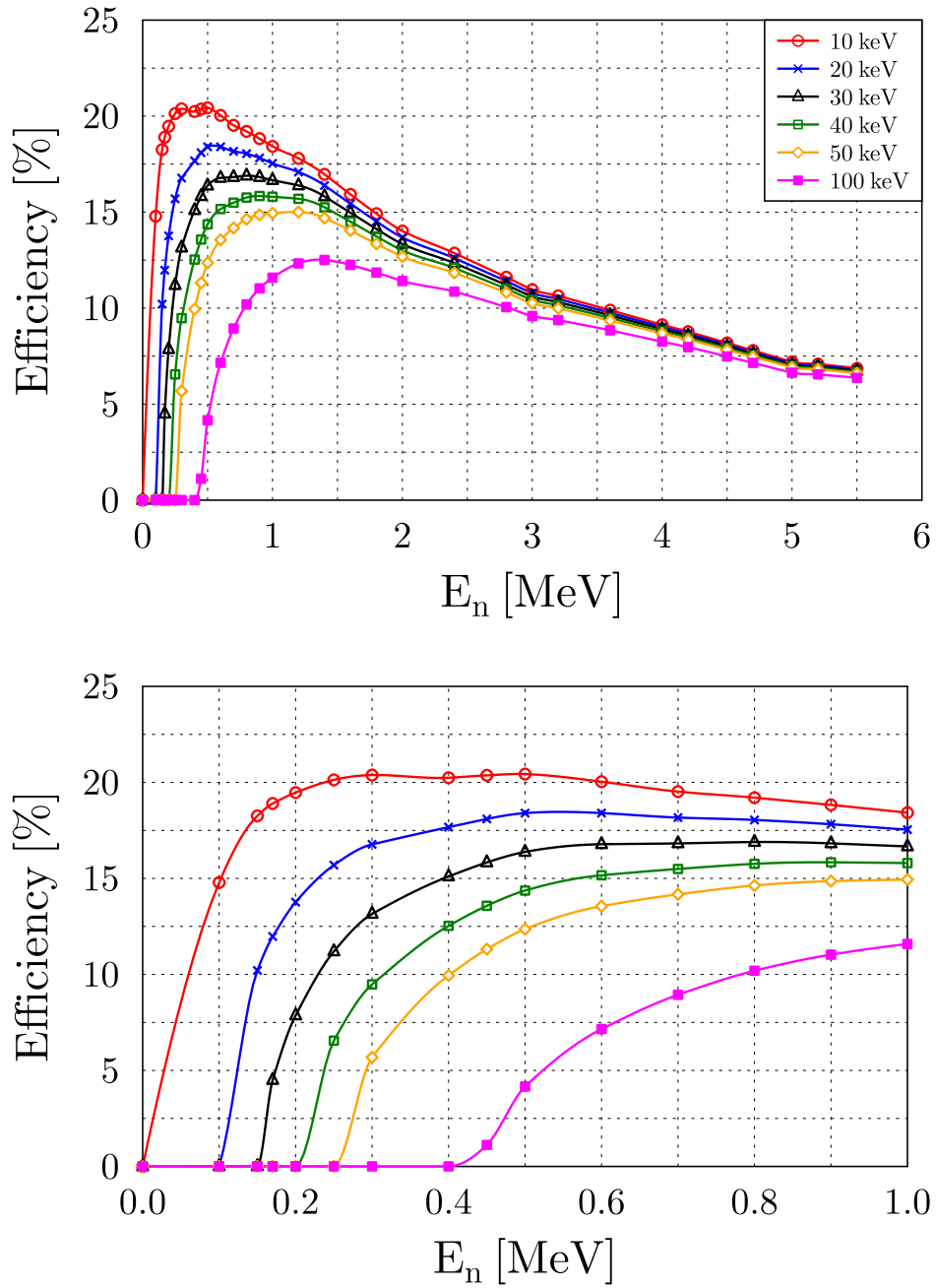
Figure 3.15: Same as Fig. 3.14, but for *"setup B"*.

4

Analysis and Concepts

The following chapter describes the most important analysis steps in the evaluation of experiments performed at the ALADIN/LAND setup. After an introduction to the basic concepts, the analysis package land02, fundamental analysis steps, and a detailed description of the calibrations of the individual detectors are presented.

At the end of the chapter, the tracking algorithm is described and connected to the efficiency and acceptance corrections for the proton trajectories in the proton branch.

4.1 Overview

The analysis of experiments performed at the ALADIN/LAND setup incorporates many different detector systems and thus a variety of calibration steps. Moreover, all detectors need to be internally and externally synchronized with respect to time and energy.

In the experiment described in this thesis, in total four different detector types were used,

(1) Plastic scintillators with fast PMTs attached

(2) Semiconductor detectors

(3) Electron drift chambers

(4) NaI crystals.

Every detector type needs to be calibrated with individual alogrithms during the analysis of the experiment. In the experimental phase, different calibration routines are running, used to monitor the performance of the detectors during the whole experiment. Furthermore, since many detectors are based on the same detector type, it is possible to combine the calibration steps into standalone programs, which deliver the necessary information for the calibration.

In order to be able to perform the basic calibrations, different beam settings during the run are used to take special data necessary for the calibration purposes.

(a) **Three energy runs:** At the beginning of the experiment, (at least) three different beam energies are employed to calibrate the incoming ion identification. This is subdivided into two tasks, namely

(i) Measuring the distance from S8 to POS with the time of flight using the known beam energy of the accelerator.

(ii) Calibrating the energy loss in the PSPs with a beam of known nuclei and energy.

(b) **Sweep runs:** To illuminate the active area of the detectors behind the magnet, the beam is *swept* over the entire area by varying the magnetic field within a certain range. The sweep run is restricted to the horizontal plane, since the magnet bends the trajectory of the ions in x-direction.

(c) **Pixel runs:** In order to calibrate the position reconstruction of the PSPs, a special grid mask is inserted remotely in front of the PSPs. On the grid mask, holes are situated at known distances. The image of this mask can be reconstructed with the PSPs, and can be used to calibrate the position read-out of the detectors.

To extract the charge of a passing ion, the theory of Bethe-Bloch is employed, describing the energy loss of an ion of charge Z in matter of the thickness dx, by

$$-\frac{dE}{dx} = \frac{4\pi e^4 Z^2}{m_e c^2 \beta^2} \cdot N \cdot Z_{\text{material}} \cdot \left[\ln \left(\frac{2m_e c^2 \beta^2}{I} \right) - \ln \left(1 - \beta^2 \right) - \beta^2 \right], \qquad \boxed{4.1}$$

where Z_{material} is the charge of the material, N the number density, and I the ionization potential of the material. Moreover, e and m_e are the charge and the rest mass of the electron. The relativistic factor $\beta = v/c$ and the Lorentz factor $\gamma = (1 - \beta^2)^{-1/2}$ are also used.

This relates the energy loss to the charge of the traversing ion in first-order approximation via

$$Z \propto \beta \sqrt{\Delta E}.$$

For a more precise description of the energy loss in material, the code ATIMA[1] is used (cf. [37]), which is based on measured and extrapolated energy losses in materials.

4.2 land02 software package

The software framework, which is used to perform important parts of the analysis, is called land02. The software package is written in C++. It incorporates a data unpacker, which is unpacking the binary data files into the file format used for the analysis. It is mandatory to set calibration parameters in a text file, which is parsed during the execution of the program.

The analysis starts with an internal calibration of a detector, i.e. energies and times measured with different detector components are adjusted to match each other. In the

---

[1]ATomic Interaction with MAtter

next step, the whole detector is treated as one unit, not using any sub-modules anymore (e.g. different PMTs of a scintillator detector). Finally, it combines different calibrated detectors.

It turned out, that different analysis levels are required to cover the full calibration of all detector types. They are

○ **RAW** This level contains the untreated information as provided by the different conversion modules. The data unit is **channels**, being the native unit delivered from the front-end systems.

○ **TCAL** The times are converted in **ns** and the charge offsets (pedestals) are subtracted.

○ **SYNC** Times of individual detector components are shifted to the same mean value. The energies are multiplied by a factor to reach an intrinsic gain matching.

○ **DHIT** The coordinate system is changed to an internal detector coordinate system, additionally, single modules are now treated in bigger sub-modules (e.g. PMTs to paddles).

○ **HIT** This level provides a calibrated detector, having only one energy and one time output. All modules are combined to one single detector. The coordinate system is now changed to the external system of the experimental setup.

○ **TRACK** At this final stage, the data of one detector can be combined with other detector systems and it is possible to extract basic identification information, like the mass-over-charge ratio of the incoming beam, or the velocity of each individual ion.

In the last level, the basic calibration is finished and user-written routines are now applied to proceed with the final analysis of the experiment. An example is the tracker, which connects hits in different detectors with a physically possible trajectory to extract information like the mass or the momentum of the ion.

In principal, this analysis structure is valid for most of the detectors, still, a few detectors need different reconstruction schemes. One example for this is the Crystal Ball, which is usually already fully calibrated in the SYNC level.

ONLINE calibrations

The basic calibrations for the TCAL and the SYNC level are already performed ONLINE during the experimental phase. In order to calculate the slope of a time-to-digital converter (TDC), i.e. the relation between the internal timer, counted in channels, and the time in ns, a constantly running time calibrator (tcal) is used in the data acquisition. The charge offset of a QDC needs to be subtracted from the measured data and is measured during the experiment. Also the passage of cosmic background can be used to calibrate different detector modules, and the measured data is subsequently recorded in the files.

TCAL

During the experimental phase, a constantly running clock delivers pulses to each individual front-end system. The random time generator module is programmed to preferably cover the $(t_{stop} - t_{start})$ range between 100 - 400 ns, which is the typical range for the used TDCs at ALADIN/LAND.

A special highly-linear TDC is employed to digitize the time between the stop and start signal in order to provide a reference measurement. By relating the measurement of $(t_{stop} - t_{start})$ in each of the individual TDCs to the known time, it is thus possible to extract the slope (i.e. the linear transformation factor between channels and times in ns), as can be seen in Fig. 4.1. The offset stems from the cable paths at each TDC input, and is slightly differing for individual channels. In principle, this offset should remain the same during the experiment, as long as no cables are changed. Thus, it also serves as a monitor for the reliability of the TDC throughout the full experiment.
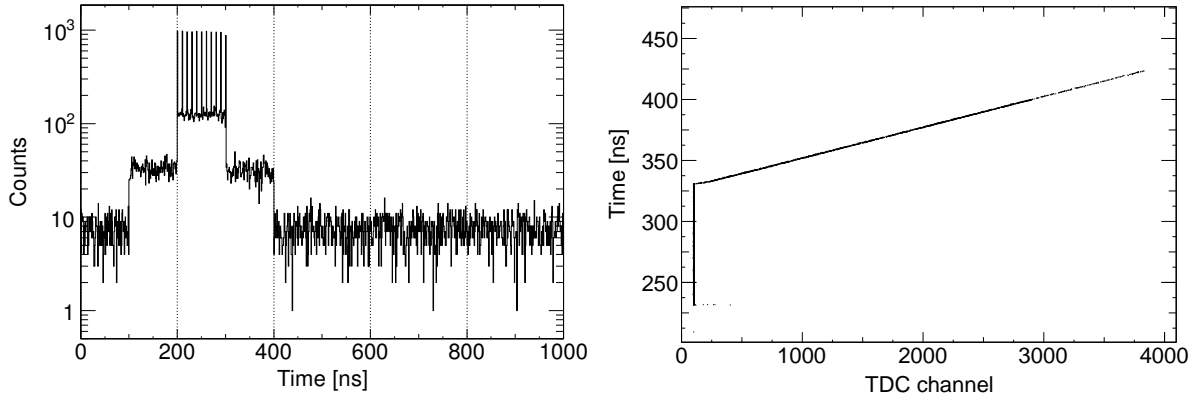
Figure 4.1: Left: The TCAL time distribution measured with a reference TDC. The region between 100 and 400 ns is preferred. Right: Linear correlation between the measured TCAL time calibration distribution and the channels of a TDC. The slope of the distribution gives the conversion from channels to times.

CLOCK

A QDC integrates the current of the incoming pulse in a given time window, which means it measures the charge. This is performed by an internal integrator circuit. However, the circuit requires a bias voltage to operate linearly and constant over time. This results in a zero-input voltage of the QDC and sets the internal zero-point of the QDC. This operating voltage and its digitized value is called pedestal.

The data acquisition system of the ALADIN/LAND setup provides a constantly running

clock, which triggers a read-out of the QDC when no event occured, only the pedestal of the QDC is digitized. The resulting value is used twice. First, it is used to set repeatedly an internal QDC threshold, which is used to reject events below a given value. Secondly, it can be used to monitor the performance of the QDC during the experiment, since the pedestal value should not change. Fig. 4.2 shows a typical pedestal distribution for one energy channel of the POS detector.
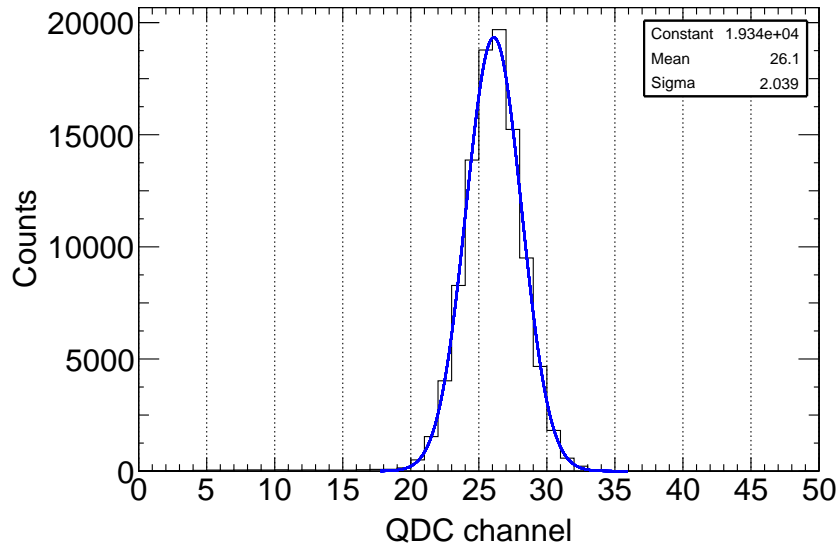
Figure 4.2: A typical pedestal distribution of a QDC channel. The width of the distribution is 2 channels, which is a common value for the QDCs in use.

Software-based routines evaluate the TCAL and CLOCK data and deliver the corresponding calibration parameters, which are subsequently incorporated into the land02 package. This is the basic calibration sufficient to perform the first step from the RAW to the TCAL level. In the following sections, the data are assumed to be calibrated up to the TCAL level or higher, if not explicitly otherwise mentioned.

4.3 The incoming calibration

The beam entering the experimental area usually consists of many different isotopes with similar mass-over-charge ratio. Therefore, it is necessary to identify the incoming beam and the reaction channels. This procedure can be done offline during the analysis. A measurement of the velocity, position, and charge is required for the reconstruction of the four-momentum of the incoming particles. For this purpose, three detectors are situated upstream of the target position:

(1) S8 [time, position]

(2) POS [time]

(3) PSP [position, energy loss]

The distance between S8 and POS is determined with the help of measurements at different energies at the beginning of the experiment, via

$$
\begin{aligned}
\beta = \frac{v}{c} &= \frac{S_{S8-POS}}{\Delta t_{S8-POS} \cdot c} \\
\Delta t_{S8-POS} &= t_{meas.} - t_{off} \\
\Rightarrow \beta \cdot t_{meas.}(\beta) &= \frac{S_{S8-POS}}{c} + \beta \cdot t_{off}.
\end{aligned}
$$

With the known β for the (three) different energies, it is thus possible to extract the distance S_{S8-POS} and the time offset t_{off} (stemming from cable lengths) by using the linear correlation between $(\beta,\beta t_{meas.})$. The distance for the experiment analyzed here was $S_{S8-POS} = 55$ m. This value is used throughout the entire analysis, and is thus used to extract the velocity of each individual ion.
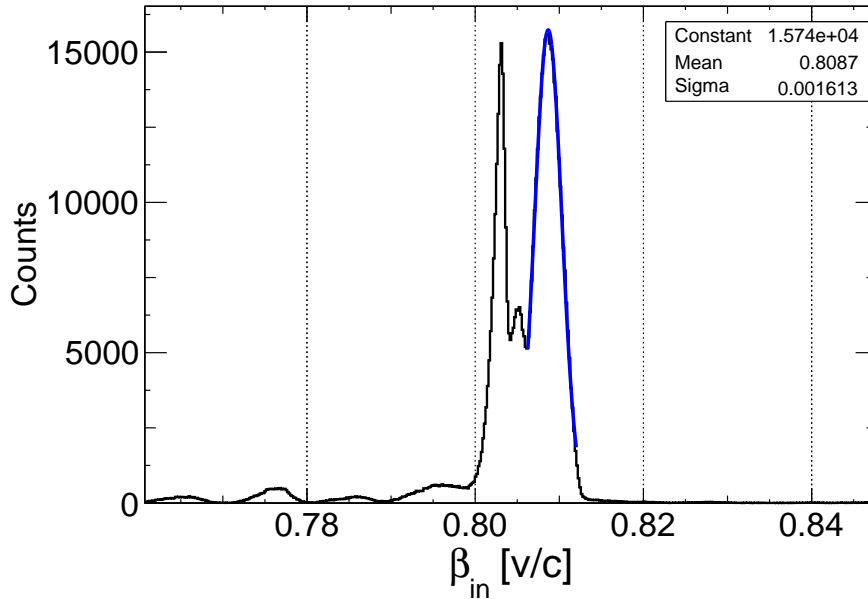
Figure 4.3: The β distribution for incoming ions shows three dominant peaks corresponding to the isotopes ^{32,33}Ar and ^{31}Cl. The resolution is extracted to be 0.2 %.

One of the basic formulas of ion optical setups relates the momentum p and the charge q of an ion to the magnetic field B and the gyroradius ρ by

$$B\rho \quad \propto \quad \frac{p}{q},$$

and by using $p = A\beta\gamma$ and $q = Z$, the formula is

$$B\rho \quad \propto \quad \frac{A}{Z}\beta\gamma.$$

Note, that the $B\rho$ value is known from the settings of the fragment separator (FRS). Thus, it is possible to measure the mass-over-charge ratio from the time of flight. Fig. 4.3 shows the distribution of different β-values for the incoming particles.

As mentioned above, the energy loss and the corresponding charge of the passing ions is calculated based on the heuristic Bethe-Bloch formula, see formula 4.1. The relation between the energy loss ΔE and the charge Z also depends on the velocity β of the traversing ions. This effect is included in the analysis. The Position Sensitive PIN diodes (PSPs) are used to extract the energy loss and the position. Two independent PSPs are placed in front of the target.

The left part of Fig. 4.4 shows the position calibration of the PSP, performed during the pixel run. The right part of Fig. 4.4 shows the position-dependent energy loss. It is important to correct this slight effect, since it leads to distortions in the energy-loss spectrum, which affect the reconstruction of the charge.
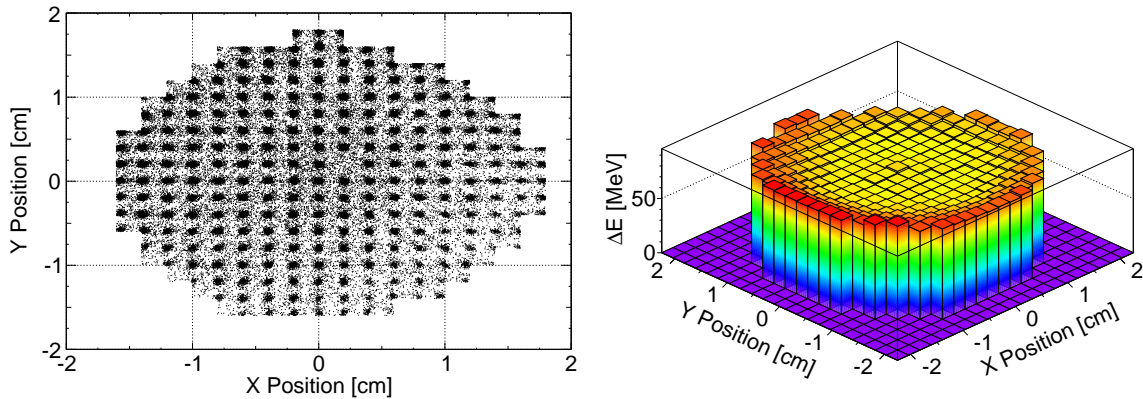
Figure 4.4: Left: The position calibration of the PSP is performed with a special grid mask. The holes in the grid mask can be identified. Right: Energy-loss distribution correlated to the position on the PSP. The position-dependent effect is corrected in the analysis.

After applying the necessary corrections, it is possible to gain the mass-over-charge ratio

and the charge for each individual ion impinging on the target.

Fig. 4.5 shows the resulting identification plot with the clear separation of different isotopes delivered in the beam. Table 4.1 summarizes the most important properties of the incoming ions.

Table 4.1: Basic kinematical and ion-optical settings for the isotopes considered in this thesis.

Isotope	β_{in}	Δt_{S8-POS} [ns]	A/Z	Bρ [Tm]	ΔE_{PSP} [MeV]	Events
^{32}Ar	0.8087	228.02	1.7778	7.5936	48.9	3.1×10^7
^{31}Cl	0.8049	229.09	1.8235	7.6835	44.0	6×10^6
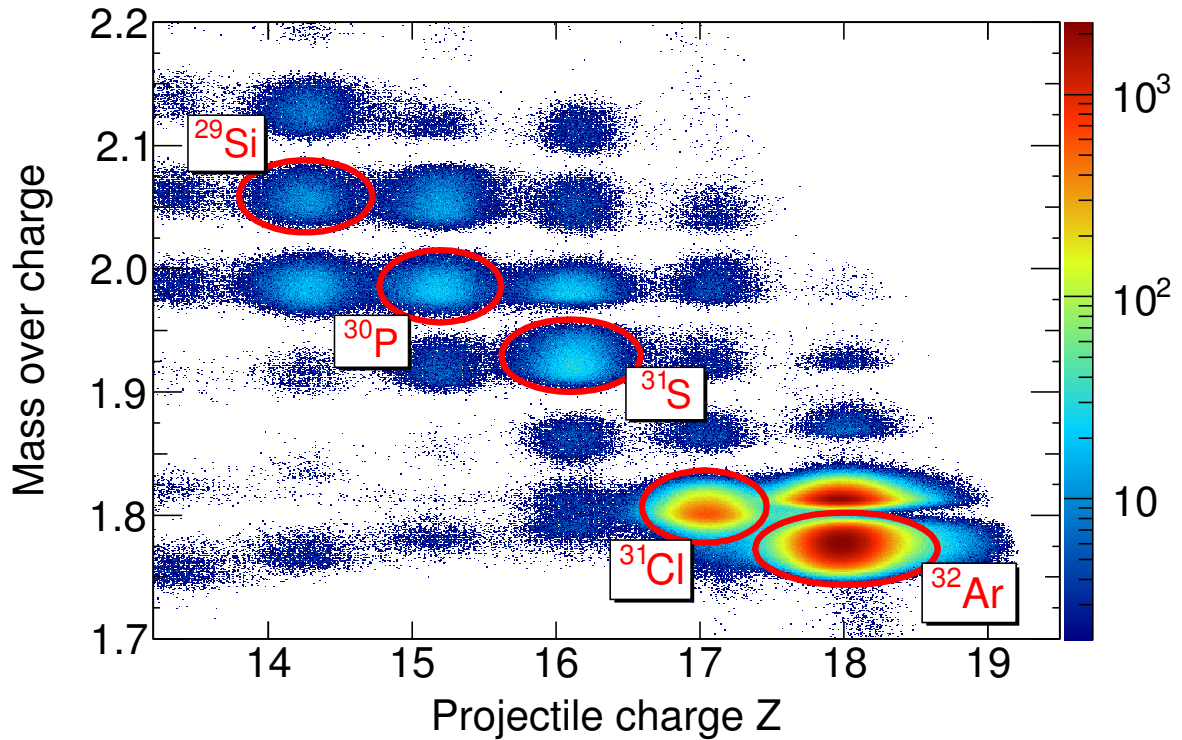
Figure 4.5: The incoming beam identification. An unique allocation of the different beam ingredients can be performed by plotting the mass-over-charge ratio and the measured charge. A variety of isotopes delivered in the beam cocktail can be identified.

4.4 The reconstruction of outgoing particles

The incoming beam is focused on the secondary target, where the reaction is supposed to take place. Downstream of the target, different detectors are placed to detect the outgoing particles. Since there are many possible reaction channels, it is necessary to be able to detect a variety of different particles. For the electromagnetic excitation mode, there can be several de-excitation channels energetically allowed. The most prominent ones are shown for the example of ^{32}Ar. They are

$$^{32}\text{Ar} \xrightarrow{\text{EM excit.}} {}^{32}\text{Ar}^* \longrightarrow {}^{31}\text{Cl} + p$$
$$\searrow {}^{32}\text{Ar} + \gamma$$
$$\searrow {}^{31}\text{Cl} + p + \gamma$$
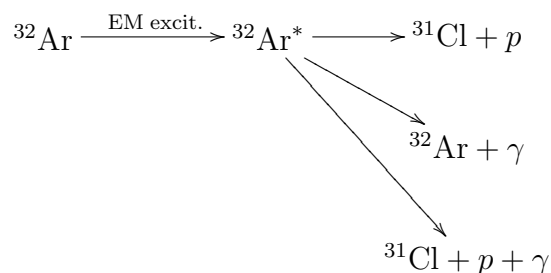
In order to be able to determine the excitation energy, all particles and γ-rays have to be detected. During electromagnetic excitation negligible momentum is transferred during the reaction. The particles are emitted in a small cone in beam direction.

The detection of the outgoing particles is split into different branches: for heavy ions (in the previous example ^{31}Cl), for protons, and for γ-rays, emitted instantaneously in-flight from the decaying residual ion. The γ-detection is performed with the Crystal Ball, whereas the heavy ions and the protons are separated in-flight in the magnetic field of the ALADIN magnet. DSSSDs are situated between the reaction point and the ALADIN magnet in order to reconstruct the trajectories of all particles. By combining the trajectory before and behind the magnet, the vertex of the reaction products can be reconstructed.

The four-momentum p_μ comprises the energy E and the momentum $\vec{p}$ of the corresponding particle in the following way ($\hbar = c = 1$):

$$p_\mu = (E, \vec{p}),$$

where the vector components of $\vec{p}$ can be determined by measurement of the polar and azimuthal angle θ and ϕ, and the total momentum p_0, via

$$\vec{p} = \begin{pmatrix} p_0 \sin\theta \cos\phi \\ p_0 \sin\theta \sin\phi \\ p_0 \cos\theta \end{pmatrix}.$$

The total momentum p_0 can be derived by

$$p_0 = m_0 \cdot \beta \cdot \gamma,$$

thus employing the time of flight to calculate β and the Lorentz factor γ.

4.4.1 The DSSSDs

The reconstruction of the position of the interaction point in the DSSSDs is obvious, since the detector itself is segmented into strips with known dimension. It is important to distinguish between a proton and a heavy ion traversing the detector. The signal will be different for both particle types and since the DSSSDs are the only detectors, where both particle types have to be detected at once, it is important to investigate this difference in more detail.

If a particle crosses the DSSSDs, a small pulse is generated, distributed over several strips depending on the charge. The induced small pulse is read out with the attached electronics. Like other detectors, the DSSSDs also deliver pedestals in each strip, which are subtracted in the TCAL level. Fig. 4.6 shows the detector response for a single hit, spread over a few strips.
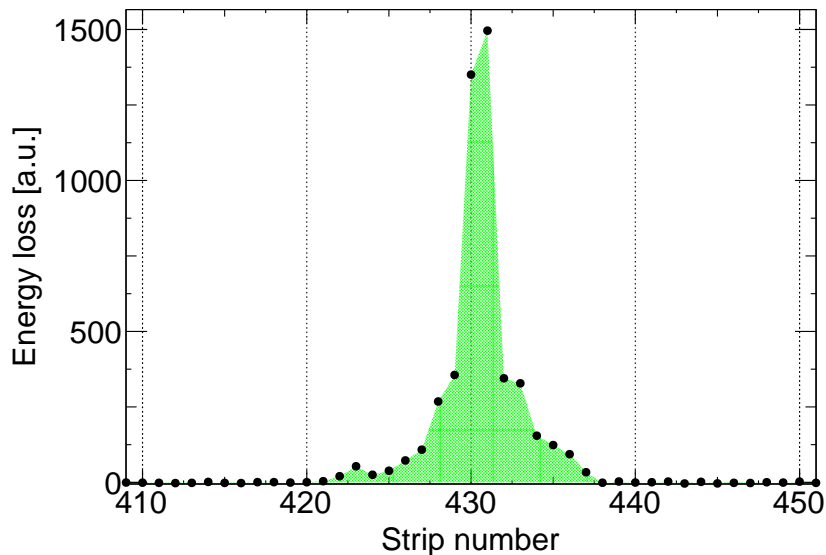
Figure 4.6: One event detected in the DSSSDs. The charge is distributed over a few read-out strips. The area below the peak (green) corresponds to the energy loss and is subsequently used in the higher analysis levels.

In order to find the position and the total deposited energy, a reconstruction of the hit distribution needs to be performed. The center of gravity corresponds to the interaction position, because each individual strip can be mapped to a position. A hit involving more than one strip is called a cluster.

One of the problems of the reconstruction algorithm lies in the treatment of dead strips, defined as strips with a distorted or no signal, and appearing on each side of the detector. If such a strip is involved in a cluster, it is important to treat it correctly.

The area below the response function can be related to the energy loss of the penetrat-
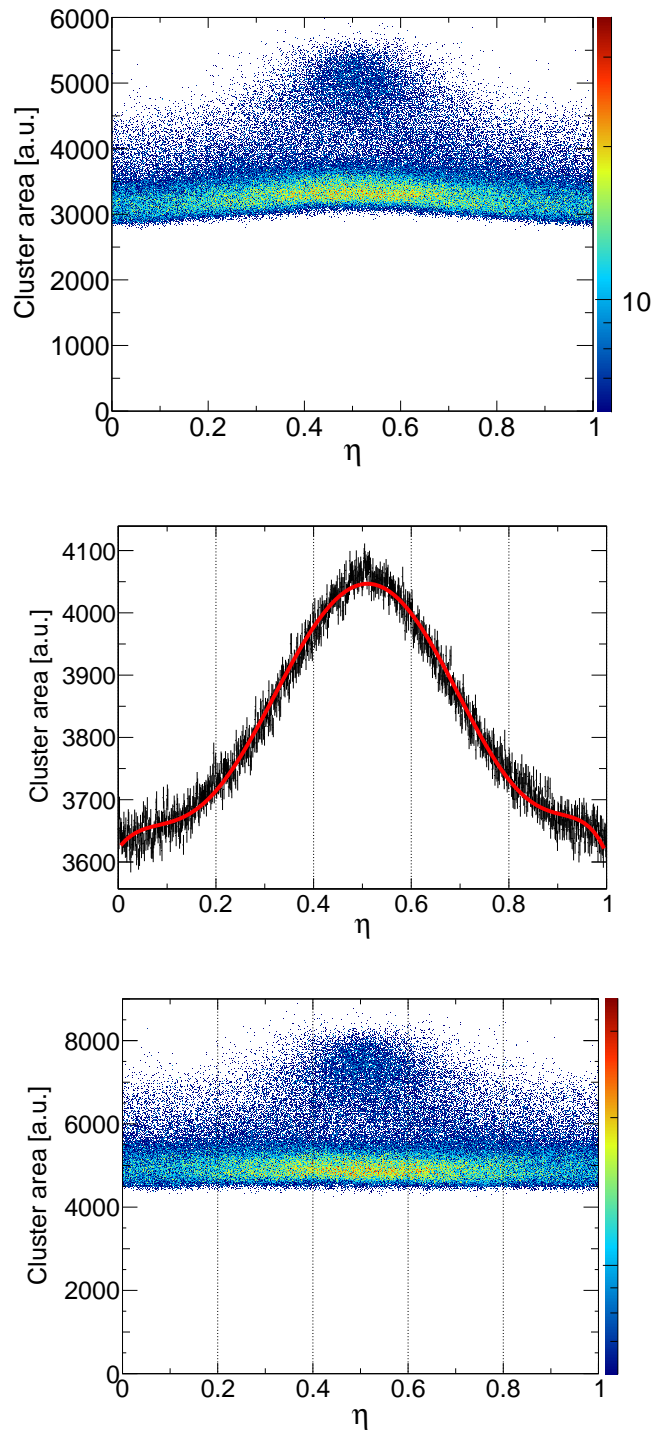
Figure 4.7: Topmost: The uncorrected cluster area between two strips for the unreacted beam ^{32}Ar depending on η. Middle: The η profile and a corresponding correction function (red fit). Bottom: The η-corrected energy loss.

ing ion. Therefore, for each single hit, the response function is applied and the integral is calculated and assigned as the energy of the hit. Moreover, the energy deposition depends on the exact interaction position of the hit. Especially between two strips, the digitized energy-loss value is different than for a direct hit. This effect is treated with a special η-correction function. The variable η describes the position between two strips and is used for inter-strip hits. The topmost figure of Fig. 4.7 shows the η distribution for the unreacted ^{32}Ar beam. The middle part of the figure shows the profile of the distribution with a corresponding correction fit. The η-fit parameters are subsequently used to correct the η-profile, and the result of this correction is shown in the bottom part of Fig. 4.7.

Moreover, the strip read out is performed by different on-board VA chips (a high dynamic range charge sensitive amplifier and shaper). Each VA chip connects 64 strips and is able to store the signal for a certain time. Furthermore, each single signal is sent to the flash-ADCs and is digitized there. Each VA chip ($\equiv$ 64 strips) is working with a slightly different gain and hence, a gain matching is required. The problem of this correction is, that in the DHIT level of the land02 analysis package, the single energies are already transformed to the cluster area ($\equiv$ area below the hit distribution). This means, it is not possible to assign an individual energy to each strip, which could be corrected then. Moreover, the transformation between the SYNC level (with individual strip energies) and the DHIT level (with cluster sum energies) is an unique mapping function. It turned out, that it is possible to apply the corrections on the DHIT level and to correct wrong gains and other distortion effects in a position-dependent way. Fig. 4.8 shows the results of this calibration step. It can be seen, that the bottom part of the figure shows the corrected and calibrated energy-loss spectrum as a function of the position. Furthermore, all four sides of the two detectors are calibrated in the same way and thus, gain factors are applied to adjust the energy losses to one common value.

However, the charge $Z = 18$ is already too high to resolve several individual charges around $Z = 18$. Especially the S-side of the detector shows a response, which is dominated by saturation of the cluster area, stemming from the special read out of the S-side, where only every fourth strip is read out and the others in between are left floating. Fig. 4.9 shows the cluster area of both sides plotted against each other for the unreacted ^{32}Ar beam. As stated above, the S-side resolution is dominated by saturation effects, seen as a long tail to high energies, whereas the K-side works much better.

The situation is different for protons. Protons cause only very small signals in the detector. The width of the response function is called base width, which corresponds to the number of strips contributing to the cluster area. Fig. 4.10 shows the proton cluster area, situated very close to the electronic noise, and the difference in the base width for protons and heavier ions (in this case ^{32}Ar).

68
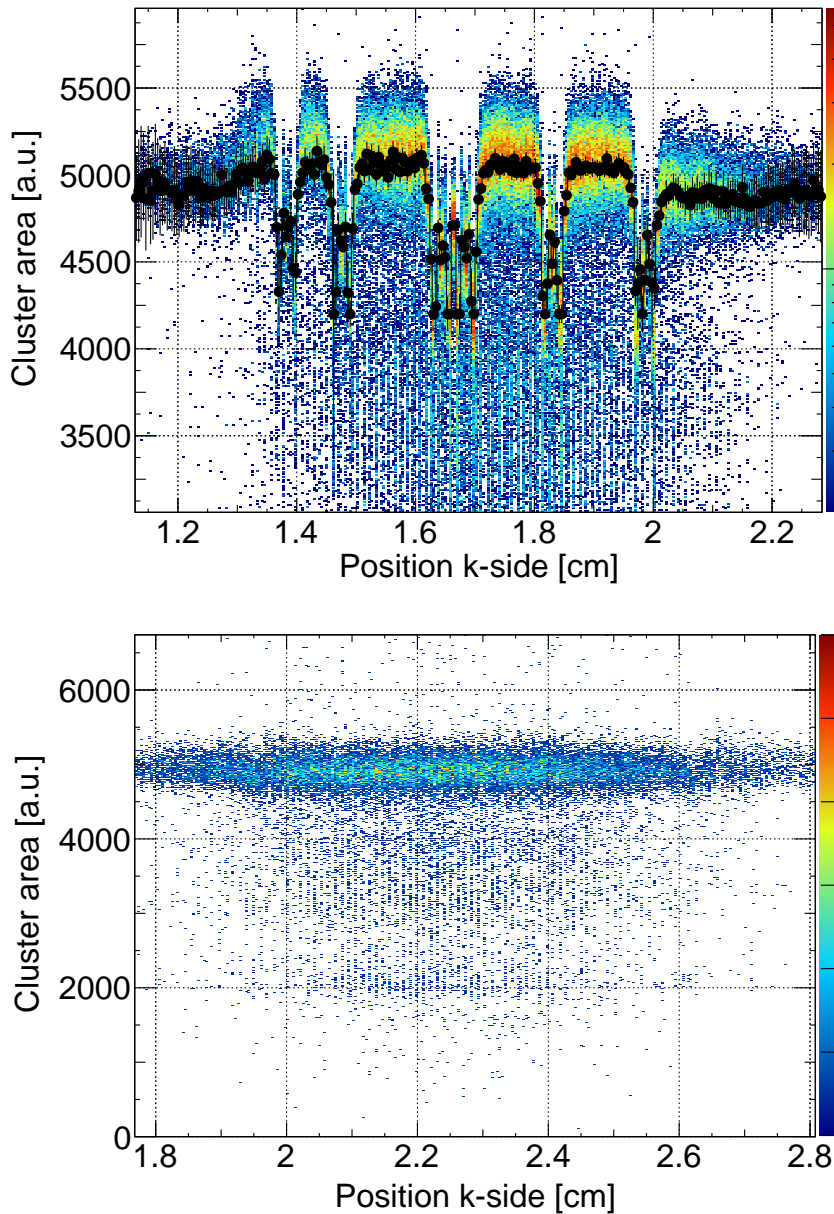
Figure 4.8: The center of gravity of a single hit gives the position on the corresponding side of the DSSSD, whereas the cluster area corresponds to the energy loss. Top: The distorted energy-loss spectrum of the K-side of one DSSSD. Different single-strip gains, VA chip gains, and other effects lead to an unmatched spectrum. The fit points (black points) indicate gaussian fits performed for slices of the spectrum. Bottom: The energy-loss spectrum after the correction.
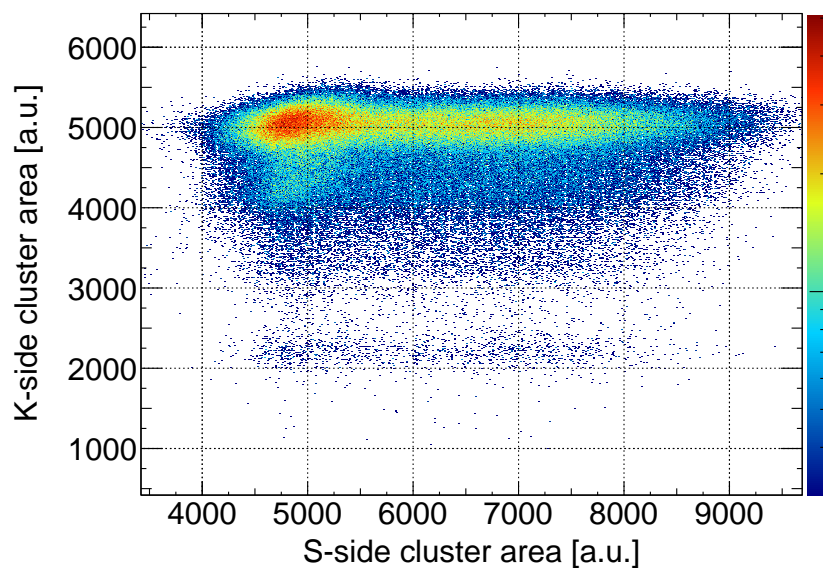
Figure 4.9: The response of the K- and S-side of one DSSSD to the unreacted ^{32}Ar beam. In an ideal case, only the red area, corresponding to the energy loss of one ion species, would be observed. The long tails to higher energy-loss values in the S-side cluster area stem from overflow because of the different read-out scheme of the S-side, whereas the K-side response shows small tails towards lower energies.
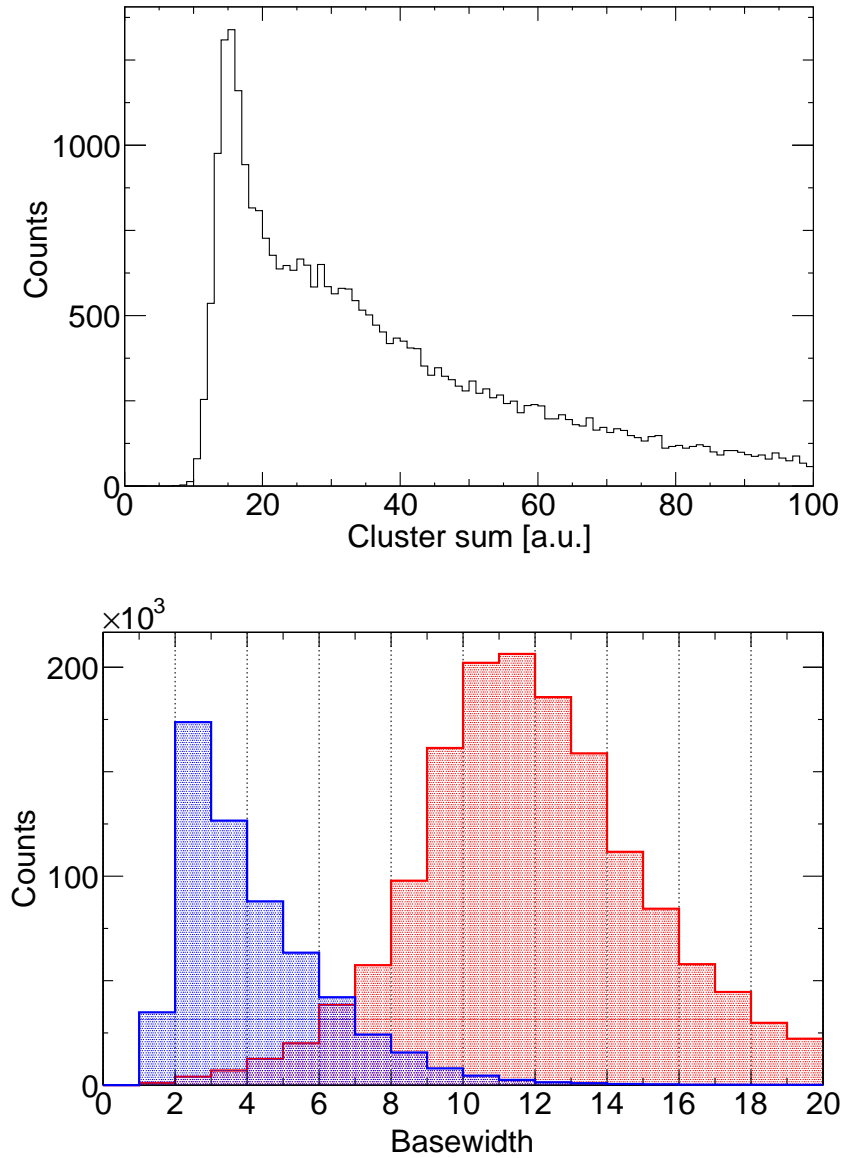
Figure 4.10: Top: The low-energy area of the cluster sum is mainly dominated by noise (around 15). The protons are situated in the region 20 - 60. Bottom: The base-width ($\equiv$ the number of involved strips) distribution for fragments (red) and protons (blue).

4.4.2 The magnetic field

In order to perform an accurate tracking through the magnet, the magnetic field inside the yoke has to be known. The $\vec{B}$ field was measured a few years ago by moving a hall sensor through the magnet and measuring the components of the magnetic field vector in each direction. Fig. 4.11 shows the three components of $\vec{B}$, if a particle moves along the z-axis through the field. The field shows small fringe field effects, mainly at the entrance and exit of the yoke. Typically, magnetic materials show hysteresis effects, but those effects can be neglected here.
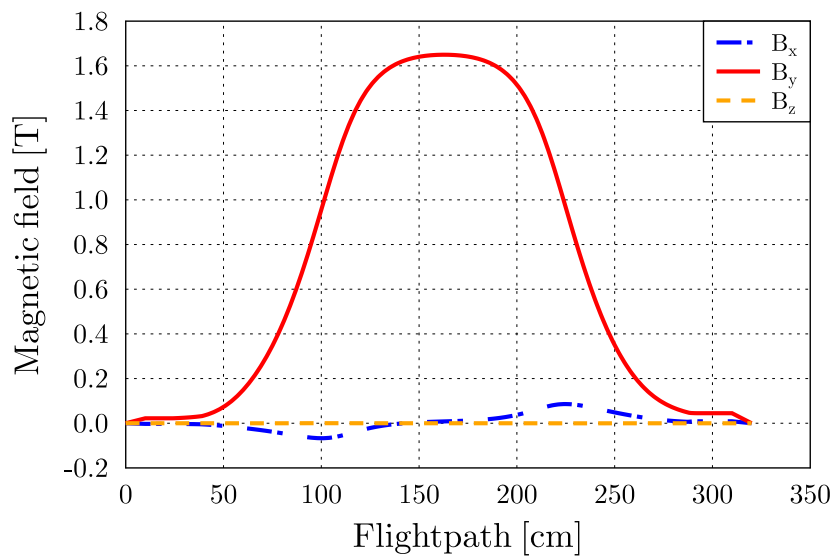
Figure 4.11: The magnetic field components of the ALADIN magnet. The three components of the field vector $\vec{B}$ are shown. Main direction of the field is along the y-axis. Small modulations of the field in the other directions stem from fringe field components.

The magnetic field has to be chosen in the way, that all particles are deflected, still being detectable in the different branches. Throughout this experiment, the maximum current ($I = 2475$ A) was applied for all settings.

4.4.3 The fragment branch

In the magnetic field, the different residuals are deflected according to

$$B\rho \propto \frac{A}{Z}\beta\gamma.$$

Since the magnetic field B is fixed, the gyro radius ρ is changing, depending on the mass A, charge Z and the velocity, reflected in β and γ of the particle. This results in different trajectories, while moving in the magnetic field.

At an angle of 16.7° relative to the undisturbed beam axis, the heavy fragment branch is situated. In order to reconstruct the trajectory of the heavy residuals, two tracking detectors are used, the GFIs. Furthermore, to constrain the charge Z of the heavy ion and the time of flight, the NTF is used.

GFI

The main task of the calibration of the GFIs is to reconstruct the two-dimensional mapping function $f(u,v)$, which is used to image the measured position (u,v) on the read-out grid mask of the position-sensitive PMT to an x-position in laboratory frame. A sweep run is used to hit almost all of the fibers and thus to induce a signal in the full read-out grid mask. A special algorithm is applied for peak-finding and separation of the (u,v)-points. As soon as the (u,v)-points are categorized, the mapping function $f(u,v)$ is employed to calculate the x-position of the hit. Fig. 4.12 shows the two steps. In the top part, the grid points are found and characterized, whereas the figure below shows the correlation of the x-positions of the first and the second detector. The linear correlation is expected, with an almost full illumination of the detector during the sweep run. Single wrongly reconstructed lines can be seen, which are because of false allocations of (u,v)-points, mainly because of too little collected statistics.

However, the calibration finishs in the HIT level, where the detector signals are converted to x-positions. Moreover, by combination of both detectors, it is possible to extract an angle between different particle trajectories. As stated above, the deflection in the magnetic field is depending on the charge, mass and velocity of the ion. Therefore, ions with the same charge, but different mass, are separated. Especially for lighter ions, the total deflection is larger.

Fig. 4.13 shows the separation of two isotopes. Using the small-angle approximation, it is possible to use the correlation between $\Delta x = x_2 - x_1$, where x_i ($i = 1, 2$) is the x-position in GFI1 and GFI2, respectively, and the position in one of the two GFIs to yield a clear separation of the ions. This allows special two-dimensional cuts on the GFIs for further cleanness of the reaction channel. Note, that this is more and more difficult for heavier ions, since the particle tracks are not clearly and visibly separated anymore, because of the smaller deflection in the magnetic field.
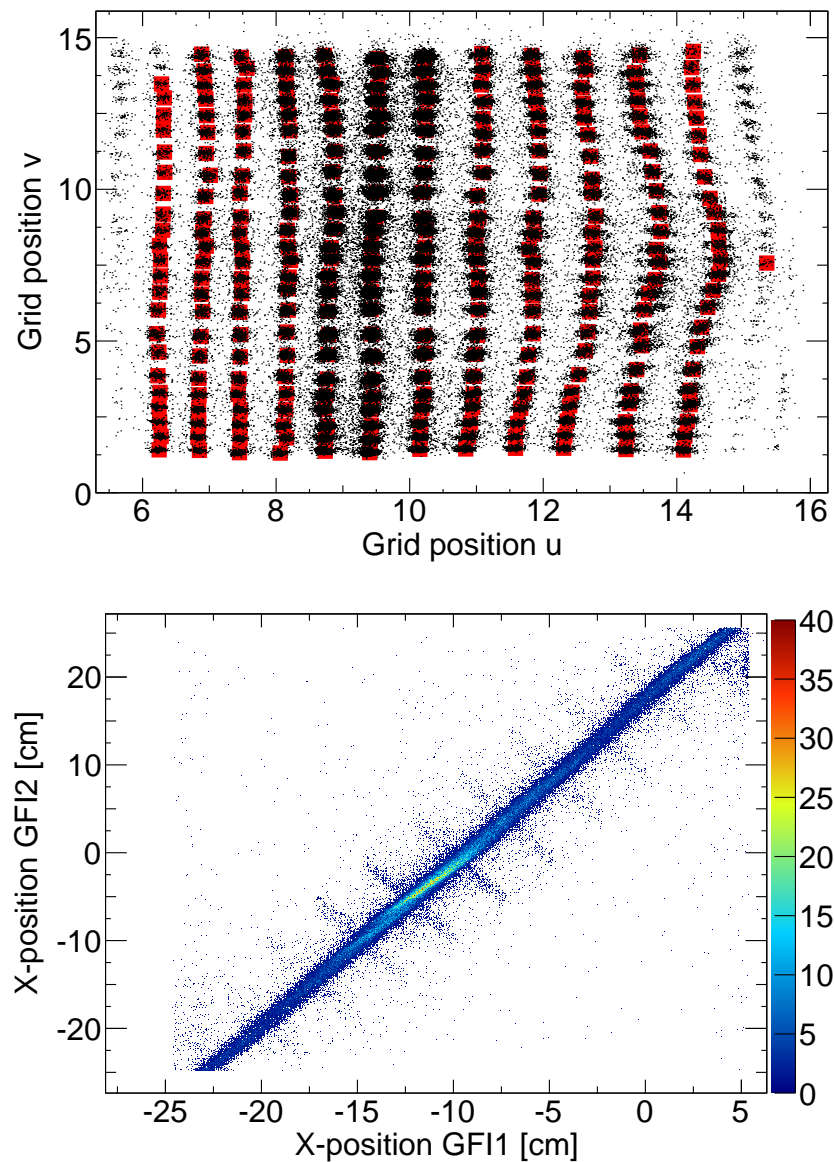
Figure 4.12: Top: The GFI hit reconstruction is based on a grid mask, which is attached to the position-sensitive PMT. Individual points in the (u,v) correlation are mapped to an unique x-position. The red squares are used to find the mean positions of the distributions. Bottom: The linear correlation between GFI1 and GFI2. Distortions stem from wrongly identified positions.
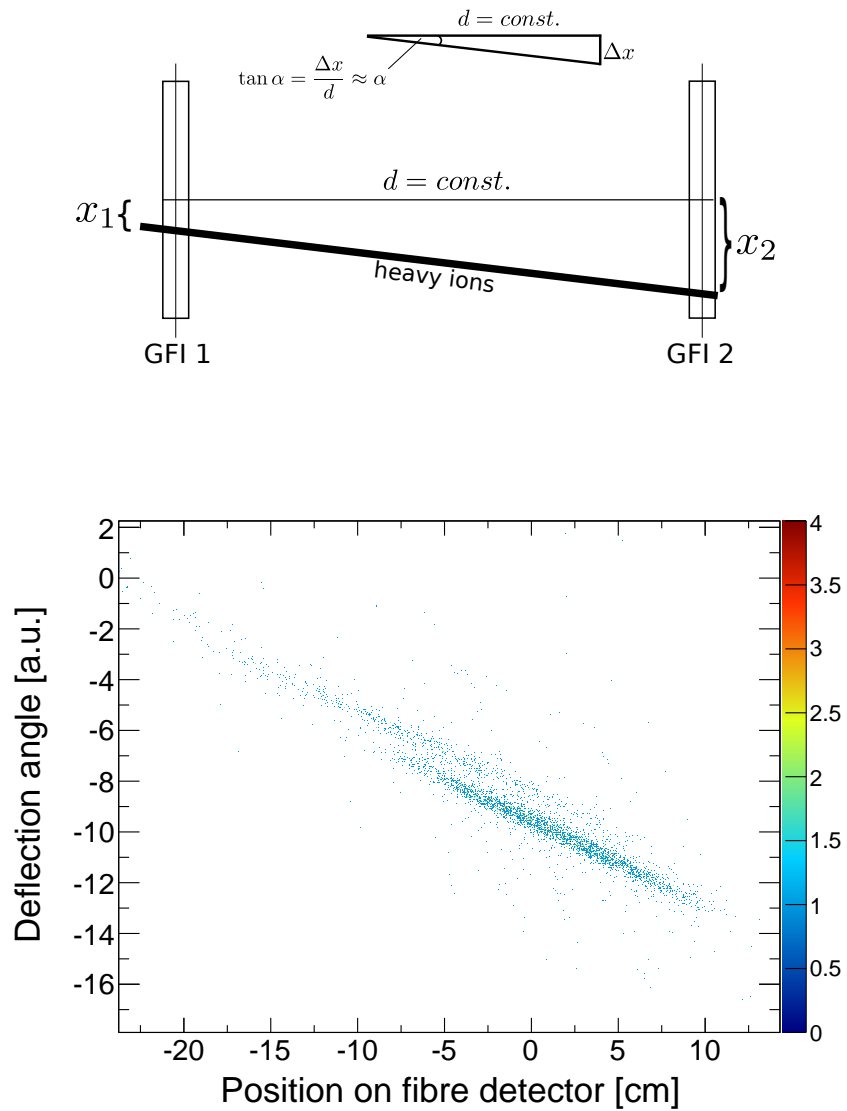
Figure 4.13: Top: Small-angle approximation used to extract the deflection angle for different isotopes. Bottom: Separation of two isotopes in the two GFIs.

NTF

The reconstruction of the time of flight between POS and the last detector in the fragment branch is performed with the NTF. The response to heavy ions allows the extraction of the charge Z of the traversing ion, which is proportional to the square root of the energy loss and the velocity. It is described with the Bethe-Bloch formula via

$$Z \propto \beta \sqrt{\Delta E}.$$

A rough gain matching of the PMTs is already done with the high-voltage settings in the experiment. However, the detailed gain matching and time calibration is performed later during the offline analysis. In principal, the calibration steps are:

(1) Conversion from channels to ns, and pedestal subtraction, performed with the on-line TCAL and CLOCK calibration data. Here, each PMT is treated individually. (**TCAL level**)

(2) Energy and times synchronized for each PMT. PMTs are still treated individually. (**SYNC level**)

(3) Both PMTs of one paddle are combined, resulting in one energy and one synchronized time for each paddle. Hit multiplicity ($\equiv$ number of hits) is calculated paddle-wise. (**DHIT level**)

(4) The full detector delivers one energy and one time for each event. Hits of x- and y-paddles are combined, no treatment of single paddles anymore. (**HIT level**)

The step from the TCAL to the SYNC level is performed by utilizing beam particles, hitting the detector. A particle with the same mass, charge and velocity deposits the same amount of energy in each individual paddle.
Being synchronized, the single PMTs can be combined to deliver one energy and one time per paddle. The times are calculated via

$$t_{DHIT} = 0.5 \cdot (t_1 + t_2).$$

For the energies, a similar algorithm is applied with

$$E_{DHIT} = \sqrt{e_1 \cdot e_2},$$

with e_i (i=1,2) being the energies measured with the two PMTs attached to the scintillation bars.
Finally, to reach the HIT level of the data analysis, all gain-matched and synchronized paddles are taken into account and combined into one single energy and time for each hit. The multiplicity is defined as the number of paddles, which recorded an energy deposition. Furthermore, the hit position is calculated via

$$\text{position} = c' \cdot t_{diff} = c' \cdot 0.5 \cdot (t_1 - t_2),$$
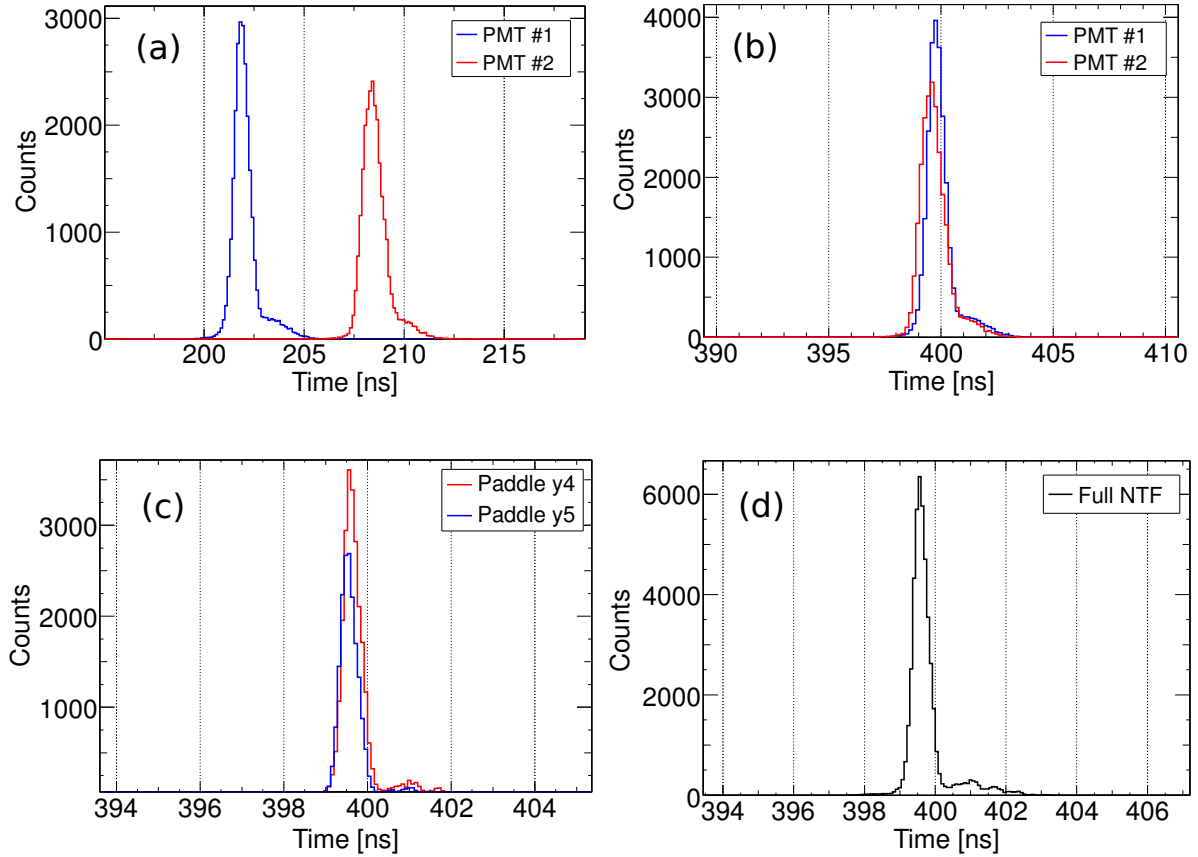
Figure 4.14: The different calibration steps for the NTF exemplary shown for the time and a hit in the center of the detector. The TCAL level (a), the SYNC level (b), the DHIT level (c), and finally the HIT level (d). Note, that in the top panel, the distributions are for two single PMTs of one paddle, whereas the left picture in the panel below shows two different paddles. In the HIT level, only one time and energy is delivered. Finally, the detector is internally synchronized.

with c' being the effective speed of light in the paddle. Fig. 4.14 shows the different calibrations leading to a calibrated detector.

The intrinsic time resolution can be calculated by taking the individual PMTs of one paddle and the crossing paddle into account. Calculating the time difference and using a Gaussian fit, an intrinsic time resolution of $\sigma_t = (43.96 \pm 0.37)$ ps is extracted, see Fig. 4.15. In the analysis, the paddles are combined and thus, the time resolution for the full detector is increased.

Fig. 4.16 shows the energy loss correlated to the x-position in the HIT level.
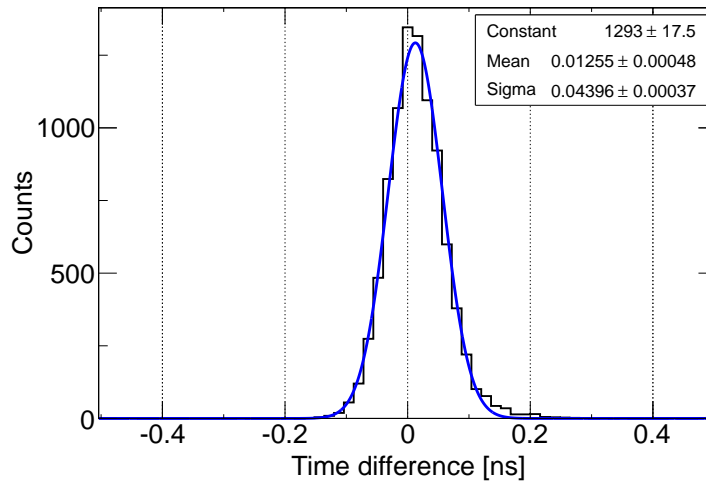
Figure 4.15: The intrinsic time resolution of the NTF. Here, the time difference of two paddles (which means four PMTs) is taken, and a Gaussian fit is applied. The intrinsic resolution is extracted to be $\sigma_t = (43.96 \pm 0.37)$ ps.

Note, that the x-position is calculated with the crossing y-paddle. Three x-paddles contribute to the energy loss, as illustrated in the figure with x_i. As can be seen, the energy loss is not flat along the paddles, moreover, it is distorted at the edges of the paddles. This effect has different explanations. First, the paddle is wrapped with a foil to protect it from light. The quality could be different along the foil. Secondly, especially at the edge, the ion could penetrate only parts of the paddle, rather the space between two paddles. This leads to less energy deposition. Finally, it could also be the scintillation material itself. Irregularities in the material (or between the corresponding paddles) can also contribute to this effect.

However, it is possible to correct this effect, as shown in the bottom part of Fig. 4.16. This allows clear cuts with sufficient separation of the unreacted and the reacted ions.

Furthermore, Fig. 4.17 shows the "smiley" effect. This effect occurs in the sweep run, where the beam is swept over the full NTF to illuminate all vertical paddles. It can clearly be seen, that the energy loss along one horizontal paddle is not constant, although the beam is the same and should produce the same energy loss.

Since it is only one paddle, an insufficient gain matching can not be responsible for this effect. It is an intrinsic effect of the paddle, and it also occurs at the larger TFW with less visibility. An explanation is, that the employed light-propagation model with the exponentially decreasing light intensity, is not fully realistic to cover all effects in the paddle, like multi reflections, delayed light emission, or coupling effects at the edges.

It is straight forward to correct this effect, however, the beam spot in the experiment is restricted to a small area on the detector. Thus, the "smiley" effect does not influence the data evaluation much and the correction, mentioned above, is already sufficient to
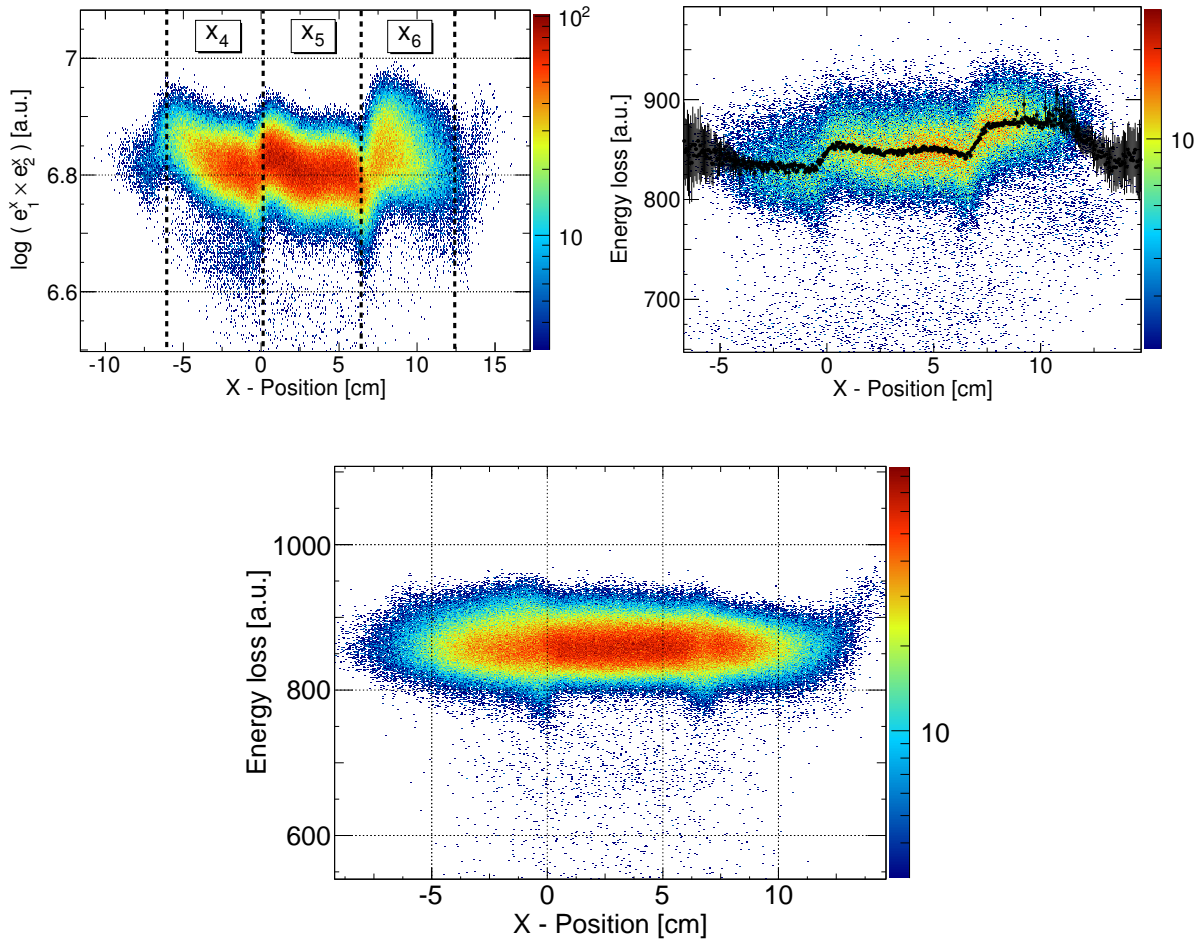
Figure 4.16: The energy loss in the NTF. The figures in the top show the energy loss distributed on three x-paddles. The x-position is calculated from a corresponding horizontal paddle. The distortions can clearly be seen. After applying a correction algorithm (top right), the energy loss is distributed smoothly, allowing to use elliptical cuts (figure below).

discriminate different isotopes.

NTF in combination with the DSSSDs

While the heavy residuals impinge on the DSSSDs without a disturbance on their way, different reactions take place on the way to the NTF. Several layers of matter are between the detectors, like vacuum windows and a thick layer of air, which induce reactions and produce several break-ups of the beam ingredients. In order to apply identification cuts, it is necessary to identify the break-up events to constrain the reaction channel. If the
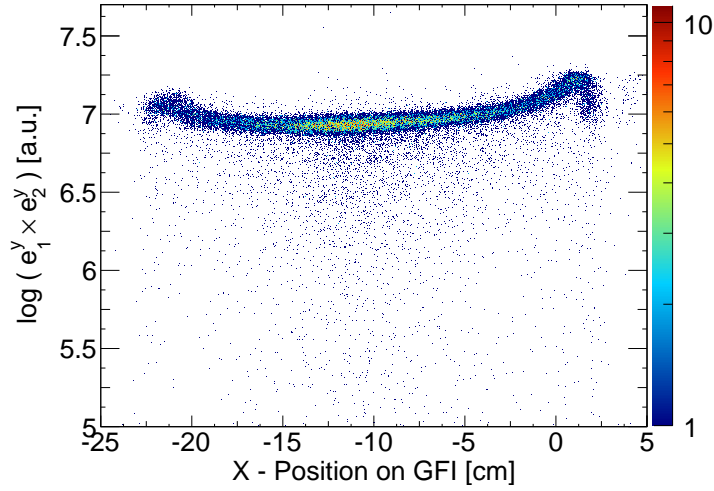
Figure 4.17: The "smiley" effect occurs during a sweep run, when a single paddle is illuminated from one end to the other. Effects of multi scattering, delayed light emission, or coupling effects are possible explanations.

unreacted beam is identified in the DSSSDs as particles, which have not reacted, it can happen, that this unreacted beam breaks up on the way to the NTF. Here, it would be identified as a real break-up event and would disturb the reaction channel. Therefore, it is very helpful to analyze an energy-loss correlation between the DSSSDs and the NTF. Before applying the correlation, the energy resolution of the DSSSDs is increased by combining the energy-loss information of both DSSSDs. Fig. 4.18 shows the correlation between the energy losses of the K-sides of both detectors.

Because of the response to heavy residuals, tails can be seen towards lower energies, which occur, if one DSSSD measures the correct energy and the other a lower energy. This translates into vertical and horizontal cuts along the correct energy loss in the correlation plot. The condition corresponds to a mathematical description via

$$\Delta E_{\mathrm{DSSSD}} = \max(\Delta E_1, \Delta E_2),$$

with ΔE_1 and ΔE_2 being the energy losses in the DSSSD1 and DSSSD2.

The introduction of the new variable by combining the energy information of both DSSSDs enables the correlation of the charge determined with the DSSSDs and with the one determined with the NTF. Fig. 4.19 shows the final two-dimensional correlation plot. The long tail to the left are break-up events of the unreacted beam between the DSSSDs and the NTF, since they have the correct energy at the DSSSD, but a different charge in the NTF. This correlation plot allows to separate different reaction channels very effectively, indicated with small arrows. Even a lack of events can be seen between the unreacted beam and the neighboring charge (Z - 1). This will be discussed in the results section in chapter 5 of this thesis.
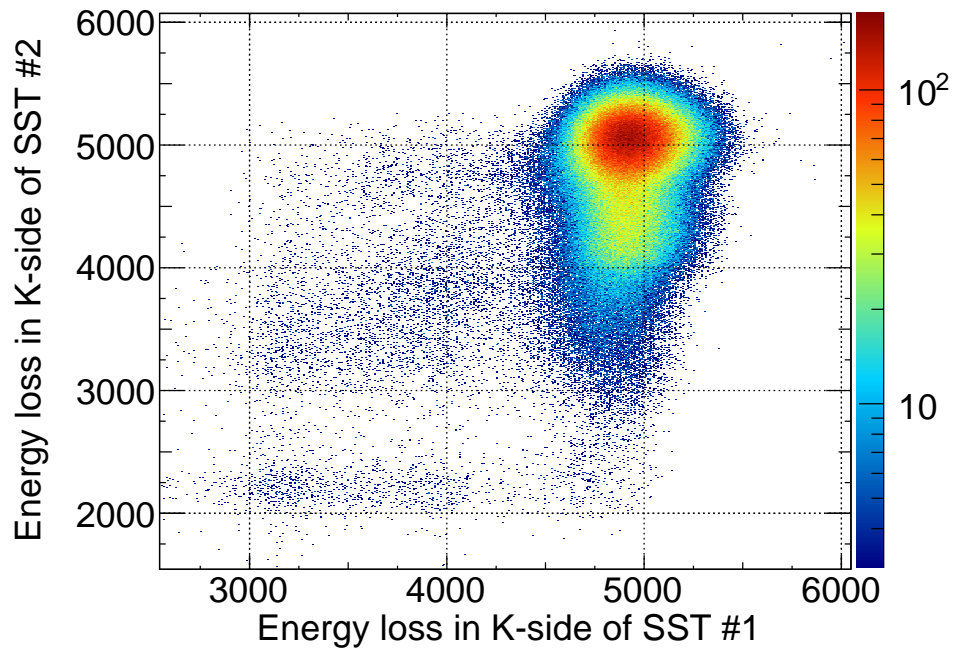
Figure 4.18: The correlation of both K-sides enables a merging of the energy-loss information, yield from both individual measurements. A new variable ΔE_{DSSSD} is introduced. Here, only the higher energy loss value from both K-side measurements is taken.
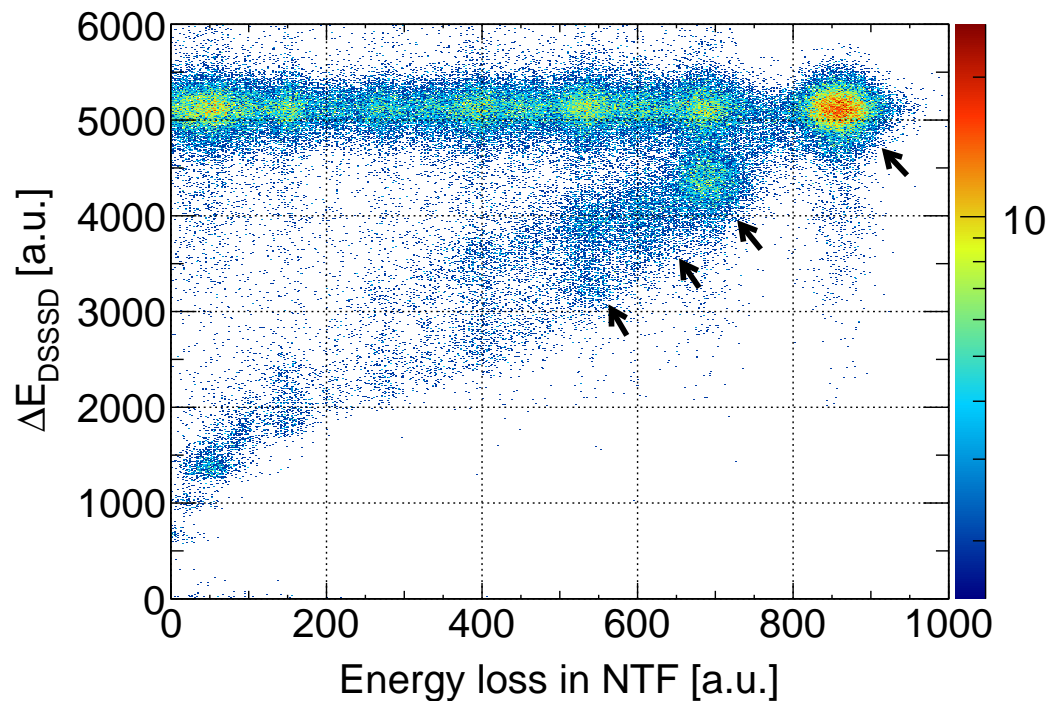
Figure 4.19: The final outgoing correlation plot for heavy residuals for an incoming ^{32}Ar beam. The energy-loss information of the DSSSDs (before the magnet) and the NTF (behind the magnet) allow a clean cut of the outgoing fragments. Different reaction products are indicated with arrows. The long tail in the NTF distribution stems from break-ups between the DSSSDs and the NTF. These events are discarded in the further analysis.

4.4.4 The proton branch

Similar to the fragment branch, a specialized proton branch is used at an angle of 31°. Basically, it comprises the same characteristics as the fragment branch. Two drift chambers are used to reconstruct the trajectory of the protons, whereas the last detector in the proton branch is used to extract the time of flight of the protons.

A proton has a mass-over-charge ratio of 1, which translates into

$$B\rho \propto \gamma\beta.$$

Therefore, a tracking for the purpose of mass determination is not required. However, a precise tracking of the trajectory is very useful to exclude background events and to reconstruct the four-momentum as precisely as possible.

PDC

The basic detection principle is the ionization of gas atoms along the trajectory of the proton. The produced electrons drift to the read-out wires, where they induce a small current, which is measured. The arrival time of the electron avalanche is used to determine the interaction position in the detector.

The basic calibration of the detector is the extraction of the relation between the arrival time of the avalanche electron pulse at the wire and the distance, corresponding to the hit position. This x(t)-curve is calculated based on physics data. The measured variable is the arrival time and the time over threshold, deduced from a leading edge and a falling edge of the detector signal being above a certain charge threshold.

The corresponding position of the hit can be determined from the arrival time of the electrons at the wires x_1 and x_2. The distance between two wires is approximately 0.7 cm and, if the arrival time at each of the wire is known, the actual position can be interpolated by

$$\text{position} = 0.5 \cdot (r_1 + (0.69282 - r_2)).$$

Therefore, the radii r_i with $i = 1, 2$ have to be known. During the calibration the relation between the arrival time and the radius is deduced with a simple algorithm. Under the assumption, that all hits will be equally distributed over the entire drift chamber and the hits are perpendicular to the PDC, the drift lengths follow a box-like distribution. This is not a fully realistic assumption, but can be used as a first-order approximation. By assuming a box-like drift length distribution and taking the measured arrival times into account, the mapping between x and t is defined and can be deduced.

Fig. 4.20 shows the distributions of the measured time and the final x(t)-curve, extracted from the experimental data.

TFW

The calibration procedure for the big time-of-flight wall is the same as for the NTF, since both detectors are using the same detector type, setup and detection mechanism.
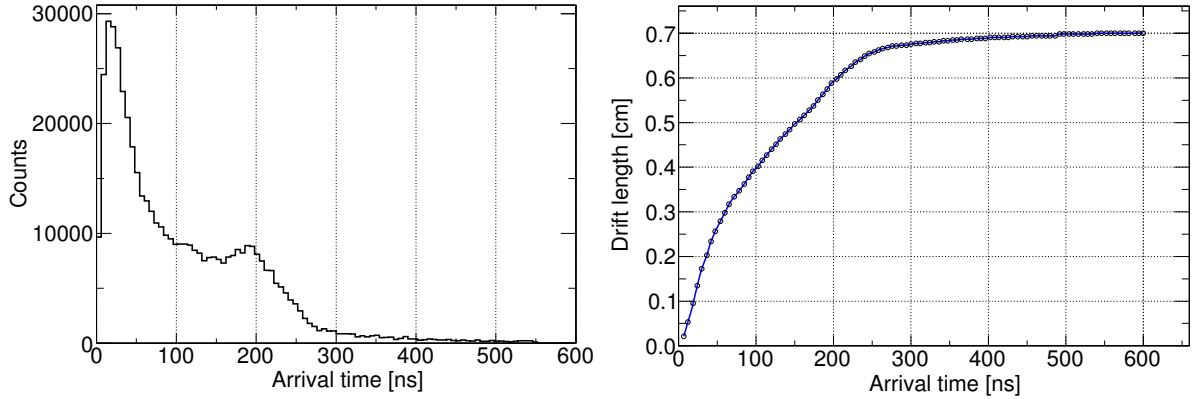
Figure 4.20: Left: By assuming a box-like distribution for the drift length (i.e. full illumination of the chamber with perpendicular hits), and by taking the measured arrival time into account, it is possible to calculate an x(t)-curve (right figure). This function relates the hit distance with the arrival time of the electron avalanche.

4.4.5 γ-ray detection

If the heavy residual is left in an excited state after the particle emission, the decay can proceed via γ-ray emission to a lower state. Then, it is necessary to detect the γ-rays emitted instantaneously in-flight, in order to reconstruct the full excitation energy of the incoming ion. The reconstruction comprises two steps:

(i) **Doppler correction:** Since the γ-rays are emitted in-flight at relativistic velocities, a basic Lorentz transformation between the lab system and the center-of-mass system has to be performed via

$$E_{cm} = E_{lab} \cdot \gamma \cdot (1 - \beta \cdot \cos \Theta),$$

with E_{lab} and Θ being the measured energy in the detector and the angle between the residual and the γ-ray.

(ii) **Add-back:** Depending on the reaction mechanism in the NaI crystal, the γ-ray could be scattered into a neighboring crystal, where it interacts again with the material and deposits energy. Therefore, a special algorithm needs to be applied, taking surrounding crystals into account, and combining the different energies into one final energy.

In the first step, the individual crystals have to be energy calibrated. This is performed with different calibration runs before, during and after the experiment, using the calibration sources ^{22}Na, ^{60}Co and ^{88}Y. For each single crystal, the mapping between QDC

channels and the energy is performed, resulting in a linear fit, which is subsequently used to calibrate the Crystal Ball. Fig. 4.21 shows the energy distribution exemplary for two sources (^{22}Na, ^{88}Y) and for one crystal. The corresponding linear fit is shown in the right side of the figure.
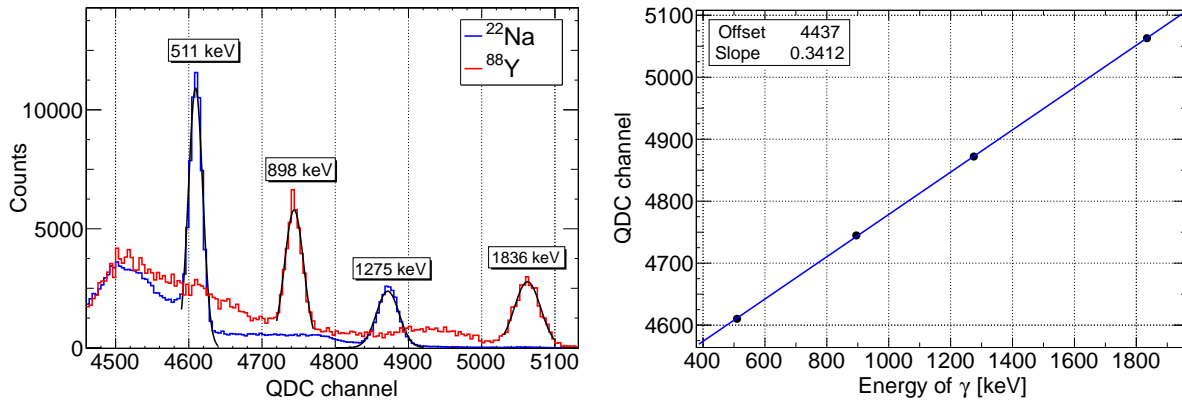
Figure 4.21: In order to calibrate the Crystal Ball, standard calibration sources are utilized. The combined energy spectrum of a single crystal is shown in the left figure. The linear correlation is used to find the calibration parameters for each individual crystal (right figure).

4.5 Tracking

A substantial part of the analysis of experiments performed at the ALADIN/LAND setup is dedicated to the tracking. In principal, tracking aims at combining single events on individual detectors to one physically possible particle trajectory with a certain mass, charge and energy. The tracking of fragments and protons through the complete setup is essential to extract the final results of the experiment.

The experimental setup allows to perform studies in complete kinematics. Basically, all kinematical properties of each individual ion can be reconstructed and used to extract information about the exotic systems. Therefore, the tracking algorithm matches theoretically calculated trajectories with the measured ones, yielding the momentum and the energy of the particles (and thus the four-momentum).

The following trajectories are being tracked separately

(a) **Incoming:** All incoming ions are tracked and identified.

(b) **Outgoing:**

    (i) *Emitted protons:* If the incoming ion is excited above the particle emission threshold, a proton is most likely evaporated. This proton is subsequently tracked and the momentum is reconstructed.
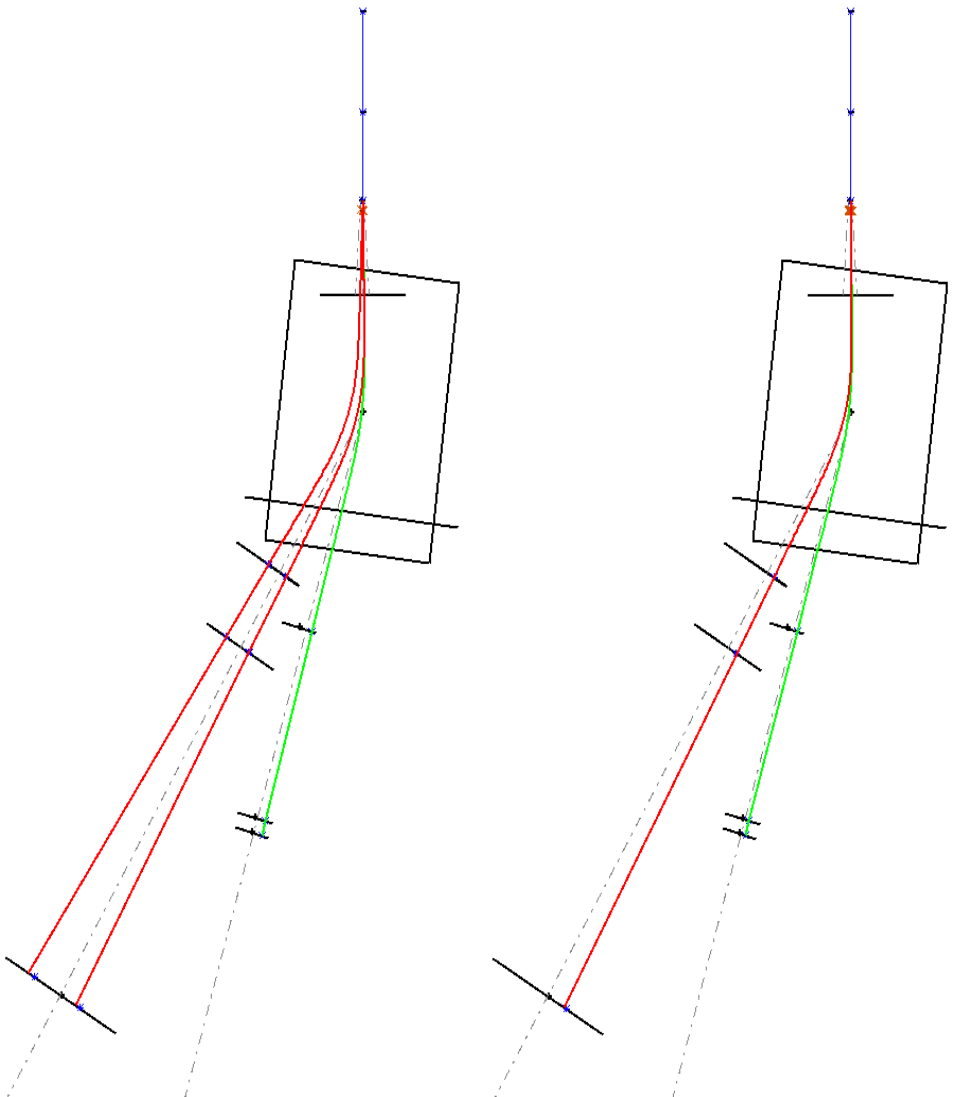
Figure 4.22: The tracking combines different single hits on individual detectors to a physically possible trajectory of the heavy residuals and the protons. For this, an algorithm tracks each ion step by step through the magnetic field. Positions are then compared to the real events on a detector. This is used to find the mass, the energy, and finally the four-momentum of each individual particle. The green lines show the fragment tracks, whereas the red lines indicate proton events.

86

(ii) *Heavy residual:* The left-over residual is tracked through the magnetic field and especially the mass and charge is reconstructed.

There are currently two tracking techniques available. Assuming the reaction point to be known from the incoming tracking, the main task remaining is the tracking of the outgoing particles. One of the approaches uses a standard trajectory through the magnetic field and calculates with ion-optical matrices the deviation from this reference track for each individual ion. Thus, it is possible to extract a $\Delta B\rho$, which is subsequently used to deduce a mass difference from the reference mass. This algorithm works very well for heavy ions, since the deviations are small and the reference track is close to the actual trajectory of the ion.

For lighter nuclei (e.g. with $A = 18$ used here), a different approach has to be used, which is based on step-by-step tracking of the particles through the magnetic field of ALADIN. The field is generally quite homogeneous, with small fringe fields at the entrance and the exit of the yoke, shown in Fig. 4.11. The following steps have to be performed during the tracking:

(1) Determine (x,y) and entrance angles before the magnet

(2) Guess a trajectory (according to the formula $B\rho$, A, β)

(3) Step-by-step tracking (probably 2 mm step size)

(4) Compare calculated and measured positions on the detector

(5) Repeat from (2) and correct the guessed value

Fig. 4.22 shows tracked events, where the figure in the top shows an one proton event and in the figure below, two protons are tracked. The corresponding fragment is also shown in the fragment branch and it can be clearly seen, that the calculated tracks match the real events in the detectors quite well, allowing the reproduction of the correct kinematical properties of the events.

Two different tracking directions could be considered: forward and backward tracking, i.e. moving with the direction of the beam, or start at the last detector and track backwards, respectively. It turned out, that the forward tracking delivers better mass resolution in this particular experiment.

Furthermore, to reach high resolution for the deduced kinematical variables, it is important to choose the correct β-value, especially for the fragment. This is depending on the reaction mechanism and the transferred longitudinal momentum. Since this experiment deals with the Coulomb excitation method, the reaction kinematics shows, that no longitudinal momentum should be transferred and therefore,

$$\beta_{\text{in}}^{\text{fragment}} \approx \beta_{\text{out}}^{\text{fragment}}.$$
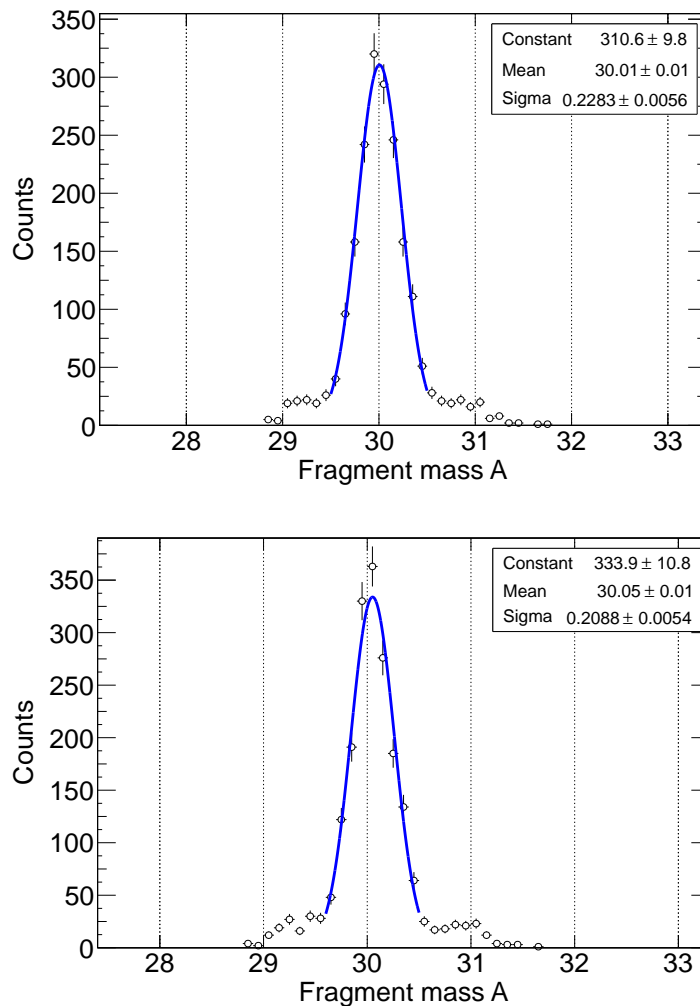
Figure 4.23: The mass distribution for the ^{30}S isotope. The figure in the top shows the mass tracked with the measured outgoing fragment velocity $\beta_{out}^{fragment}$, whereas the figure below displays the mass with the incoming velocity $\beta_{in}^{fragment}$ taken into account. The difference is small, but still, taking $\beta_{in}^{fragment}$ results in a better resolution. In general, the mass resolution is here around 0.7 %.

The time-of-flight resolution for the incoming ions is better, since they have a longer flight path from S8 to POS. Therefore, as shown in Fig. 4.23, the incoming velocity is used instead of the measured outgoing β. In conclusion, the achieved mass resolution within the tracker is extracted to be around 0.7 %.

Fig. 4.24 shows the resolution of the extracted momentum distributions of fragments and protons. The total momentum spread is calculated to be $\frac{dp}{p} = \delta p = 0.5$ %, enabling a good separation of individual masses. Furthermore, the figures below show the correlation between the deduced vertical position of the hit in the drift chamber PDC1 and the momentum of the proton. Two broken wires in the PDC1 can be identified, leaving "holes" in the projected momentum distribution in y-direction. Moreover, a cut of the momentum distribution can be seen, which is related to an acceptance cut in y-direction, due to the limited opening angle of the beam line behind the target. Thus, protons, which gained high momentum in y-direction in the reaction, are absorbed in the material of the beam line and cannot be measured behind the magnet anymore.

Both effects are corrected with the efficiency and acceptance correction for the proton arm, which will be described in the next section.
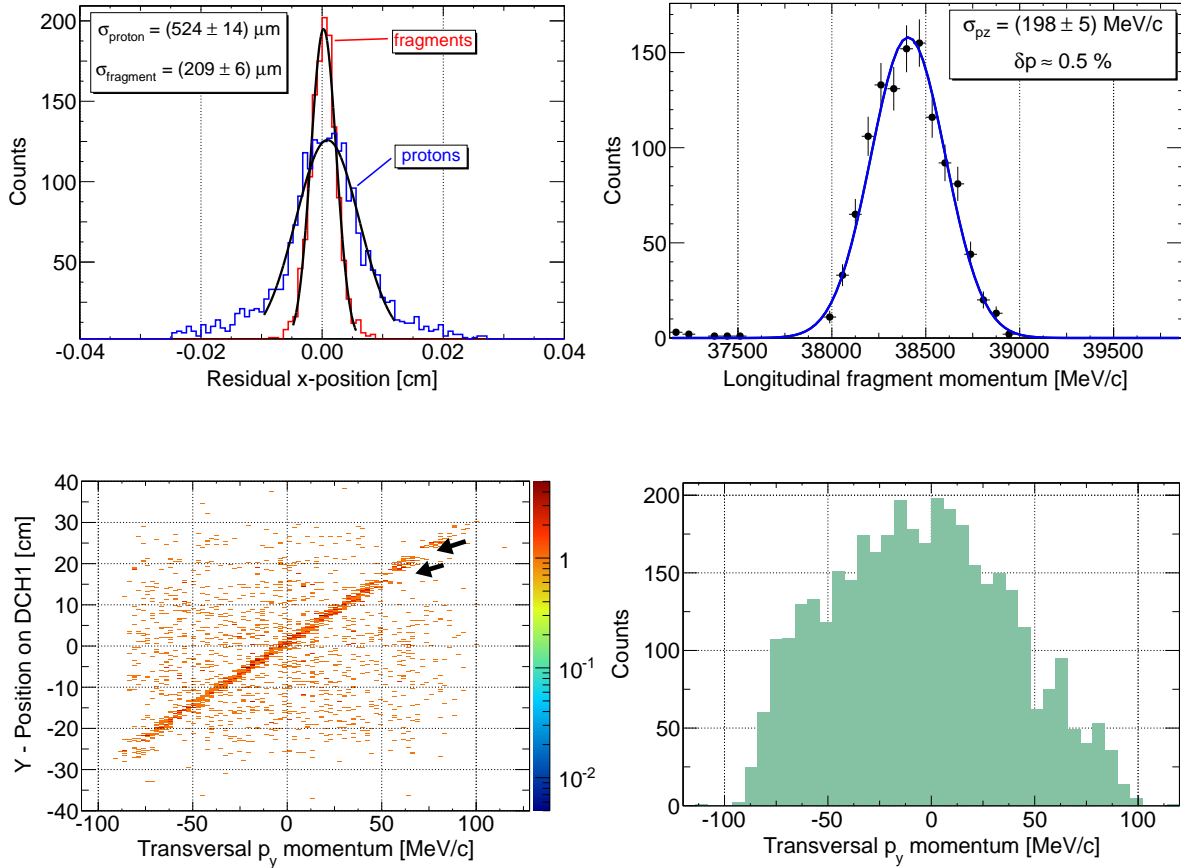
Figure 4.24: Top left: The position resolution of the first DSSSD in the tracking, displayed as a residual x-position. As expected, the fragment distribution is more localized, hence, resulting in a better resolution. The top right figure shows the longitudinal momentum distribution of the fragments. The momentum spread is $\delta p = 0.5$ %. Bottom left: The correlation of the transversal $p_y^\perp$ component with the y-position on the first PDC. Dead readout wires can be identified (arrows). The projection on the x-axis (bottom right) shows the acceptance cut of the protons in y-direction.

4.6 Efficiency and acceptance corrections for the proton branch

Each individual detector has a detection efficiency, which depends on the interaction mechanism, the quality of the material, the attached electronics, and other properties. This is especially important, if the total number of events, impinging on the detector, has to be considered, e.g. to calculate a cross section. Subsequently, it is an essential part, to deduce the detector efficiency.
Furthermore, as mentioned in the last section, there exist acceptance limitations in the setup. This also severely affects the total number of events and has to be corrected. The opening angle at the exit of the beam line in the Crystal Ball is restricted to 80 mrad, thus, at high excitation energies, the proton acceptance is reduced.

The geometrical acceptance for the proton branch can be simulated with the simulation package FAIRROOT. The sub-package R3BROOT contains the full geometrical information about the setup and can be used to simulate proton and fragment tracks. A simple event generator is utilized to produce proton and fragment events with conserving energy and momentum.
The simulation is purely geometrical and it does not consider any detector specific effects. A particle with certain momentum is generated and a test is performed, if the particle is detected in the drift chambers and the big time-of-flight wall. For a certain momentum the acceptance is then defined as

$$\text{acceptance}(\text{E}_x) = \frac{n_{\text{detected}}}{n_{\text{started}}},$$

for an excitation energy E_x and the number of detected and started events, denoted by n_{detected} and n_{started}.
The acceptance curve, as shown in Fig. 4.25, is valid for a particular reaction and a certain number of emerging particles. In this case, the simulation is done for $^{32}\text{Ar}(\gamma,\text{p})$ and $^{32}\text{Ar}(\gamma,2\text{p})$, and incorporates the specific reaction Q-values. Finally, it has to be multiplied with the excitation energy spectrum to yield an acceptance-corrected excitation function. In the case of two protons, there is a possible source of systematic errors. At low-excitation energies, the trajectories of the two protons can be so close to each other, that they can not be resolved as two protons anymore. In this case, the correction based on the acceptance curve would be wrong.
However, in order to study this possibility, the simulated data can be used. The distance of the two protons in one layer of one drift chamber can be expressed by

$$\Delta x = |x_1 - x_2|,$$

where x_i is the position in x-direction of the proton $i = 1, 2$. The same procedure can be applied for the y-direction. In the HIT level of land02, two protons can only be tracked, if the distances Δx and Δy are larger than 0.7 cm, which is the distance between two wires. If they can not be spatially resolved in one of the layers, the event will not be
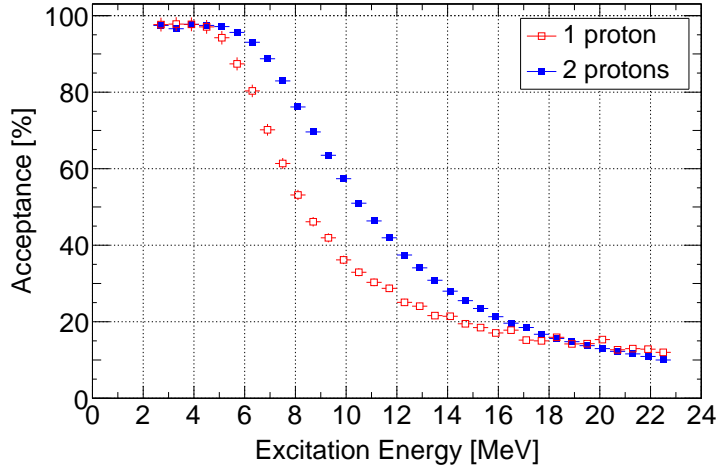
Figure 4.25: Acceptances for the proton branch, simulated with the FAIRROOT R3BROOT package. The red rectangles describe the case, when only one proton is emitted in the reaction. The blue filled rectangles show the two proton case. The curves are used to correct the excitation energy spectrum for the geometrical acceptance.

considered for the tracking.

However, this can be extracted with the acceptance simulation data, since the positions on the drift chambers are included in the code. The condition is set to be

$$\Delta x > 0.7 \ \&\& \ \Delta y > 0.7 \qquad \qquad \boxed{4.2}$$

for each plane. Only those events can be resolved and subsequently tracked. Table 4.2 shows the resulting numbers.

Table 4.2: Calculated systematical errors for unresolved two protons in the drift chambers at low-excitation energies, and if the protons are spatially not separated with a distance larger than 0.7 cm. The numbers are derived from the simulation.

Detector	Total events	Not resolved	Error
PDC1	919829	27930	3 %
PDC2	919829	31530	3.4 %

The efficiency of the proton branch includes the three individual detectors: drift chamber 1 and 2, and the TFW. The basic idea for the calculation itself is shown in the top part of Fig. 4.26. However, the TFW efficiency is not needed for the tracking algorithm, and is therefore skipped here. Basically, the tracking algorithm only checks for a proton hit (i.e. a proton trigger). The positions, and also the multiplicities (i.e. the number of registered events), are not used. Thus, the only efficiency for the TFW is the trigger efficiency, which is more than 95 % for one proton, and for two protons even more. In the following parts, the TFW efficiency is assumed to be 100 %.

For each detector, a number of proton events is extracted and then related to the total number of crossing protons. Furthermore, in order to avoid noise from single wires and scattered particles from the close GFI, the full calculation is performed layer-wise (x- and y-layers) in the DHIT level of land02. Here, a correlation between the drift chamber layers is required to check for noise and false events. Especially in the one-proton case, the background severely disturbs the efficiency calculation. The applied correlation is shown in the two figures in the bottom of Fig. 4.26.

Table 4.4 shows the different conditions used to extract the efficiency of the proton branch. The total number of events N_{total}, registered in all detectors, is calculated by setting conditions in all detectors and requiring the correlation of the events. In order to extract the efficiency of individual detector planes, the corresponding plane multiplicity must be zero, indicating a *missing event*. This procedure calculates an *inefficiency* of the detector plane by requiring a proton in the other detectors and explicitly no proton in the plane under examination. However, to exclude any random hits (which is more common in the one-proton case) or noise contributions, the above mentioned correlation between the planes is used as a further constraint. The usage of the correlation in the one-proton case is obvious, whereas the two-proton case needs more attention. Since the two protons are indistinguishable, an entry 0 in the PDC1 X - plane does not automatically belong to entry 0 in the PDC2 X - plane, and so on. This results in 2^n possibilities of mixing the entries. Therefore, the different multiplicity entries are indicated with a "[]" in table 4.4, whereas the planes are marked with a "?".

The efficiency ϵ is calculated with the relation

$$\epsilon_{DET} = 1 - \frac{N_{DET}}{N_{total}},$$

for the corresponding detector DET = {Pdx1, Pdy1, Pdx2, Pdy2}.

The results of this calculation are shown in Tab. 4.3. In principal, the efficiency correction also corrects for not resolved protons in the first drift chamber. Here, the assumption is, that the protons are separated in the second drift chamber, since it is geometrically placed a few meters behind the first drift chamber.
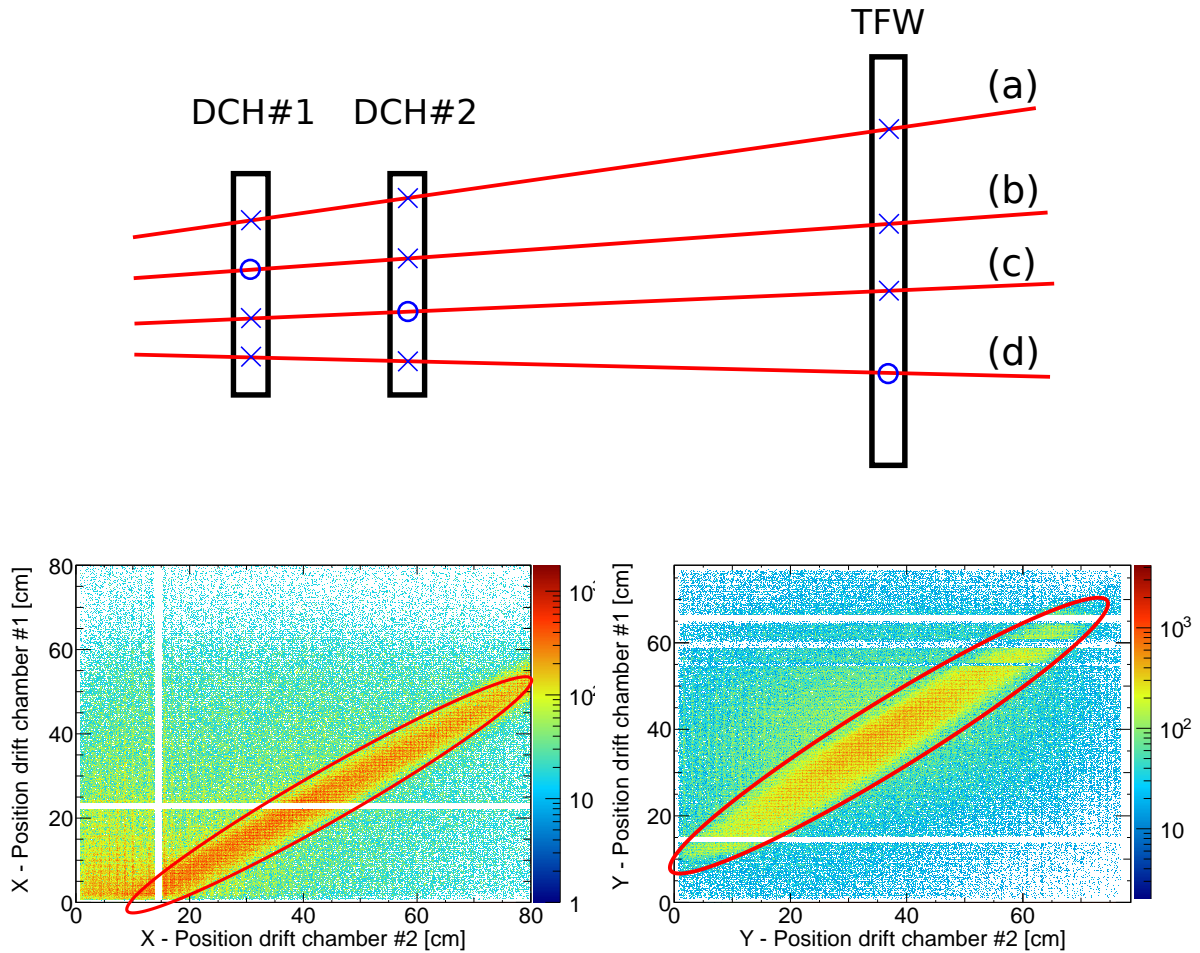
Figure 4.26: Top: The principle of the extraction of the efficiency for the proton branch. In case (a), the totally detected hits are counted, and used in the variable N_{total}. In the following cases, individual detector planes are required to *miss* an event, thus calculating an *inefficiency*. Note, that the calculation is performed in the DHIT level, where single detector planes are considered. Bottom: The required correlation between the first and the second drift chamber guarantees noise- and background-free events. This is especially crucial for the one-proton case, where noise is induced from the neighboring detectors.

Table 4.3: The resulting efficiencies for the drift chambers in the proton branch. All numbers are given in percent. The errors are statistical errors.

	Pdx1	**Pdy1**	**PDC 1**	**Pdx2**	**Pdy2**	**PDC 2**	**Total ϵ**
ϵ_{1p} (measured)	84(7)	85(7)	71(8)	93(8)	96(9)	89(11)	**63(8)**
ϵ_{2p} (from ϵ_{1p}^2)	71(12)	72(12)	51(12)	86(10)	92(12)	79(14)	**40(11)**
ϵ_{2p} (measured)	71(4)	64(3)	45(3)	88(7)	88(7)	77(8)	**35(4)**

Table 4.4: Combinations to extract the correct efficiency for the proton branch, including the two drift chambers. Multiplicities are marked with "[ ]". If x- and y-planes have to be considered, a "?" is used. See text for further explanations.

Variable	Pdx1	Pdy1	Pdx2	Pdy2	Tfxmul	Tfymul	Correlation
N_{total}	$== 1$	$== 1$	$== 1$	$== 1$	> 0	> 0	(Pdx1,Pdx2) (Pdy1,Pdy2)
N_{PDC-X1}	$== \mathbf{0}$	$== 1$	$== 1$	$== 1$	> 0	> 0	(Pdy1,Pdy2)
N_{PDC-Y1}	$== 1$	$== \mathbf{0}$	$== 1$	$== 1$	> 0	> 0	(Pdx1,Pdx2)
N_{PDC-X2}	$== 1$	$== 1$	$== \mathbf{0}$	$== 1$	> 0	> 0	(Pdy1,Pdy2)
N_{PDC-Y2}	$== 1$	$== 1$	$== 1$	$== \mathbf{0}$	> 0	> 0	(Pdx1,Pdx2)
N_{total}	$== 2$	$== 2$	$== 2$	$== 2$	> 1	> 1	(Pd?1[0],Pd?2[0]) (Pd?1[1],Pd?2[0]) (Pd?1[0],Pd?2[1]) (Pd?1[1],Pd?2[1])
N_{PDC-X1}	$< \mathbf{2}$	$== 2$	$== 2$	$== 2$	> 1	> 1	(Pdy1[0],Pdy2[0]) (Pdy1[1],Pdy2[0]) (Pdy1[0],Pdy2[1]) (Pdy1[1],Pdy2[1])
N_{PDC-Y1}	$== 2$	$< \mathbf{2}$	$== 2$	$== 2$	> 1	> 1	(Pdx1[0],Pdx2[0]) (Pdx1[1],Pdx2[0]) (Pdx1[0],Pdx2[1]) (Pdx1[1],Pdx2[1])
N_{PDC-X2}	$== 2$	$== 2$	$< \mathbf{2}$	$== 2$	> 1	> 1	(Pdy1[0],Pdy2[0]) (Pdy1[1],Pdy2[0]) (Pdy1[0],Pdy2[1]) (Pdy1[1],Pdy2[1])
N_{PDC-Y2}	$== 2$	$== 2$	$== 2$	$< \mathbf{2}$	> 1	> 1	(Pdx1[0],Pdx2[0]) (Pdx1[1],Pdx2[0]) (Pdx1[0],Pdx2[1]) (Pdx1[1],Pdx2[1])

Results and Discussion

In this chapter, the status and the results of the analysis are presented. It is organized in two parts. In the first section, the main focus is the ^{31}Cl isotope, which was one component of the mixed beam. In this case, the analysis is focused on the astrophysical impact, in particular the nucleosynthesis during the rp process.

In the second part, Coulomb dissociation cross sections of ^{32}Ar for the one proton and two proton emission channels are investigated.

5.1 The case of ^{31}Cl

One of the isotopes delivered in the mixed beam was the $^{31}_{17}$Cl$_{14}$ isotope. It has a half life of t$_{1/2}$= 150(23) ms, and decays dominantly via β^+-decay to ^{31}S [38].

The basic nuclear structure of this isotope is mostly unknown. However, ^{31}Cl is part of the $A = 31, \mathcal{T} = 3/2$ isospin quartet, with $\mathcal{T}_z$ projections of $-3/2 \leq \mathcal{T}_z \leq 3/2$. The corresponding nuclei are ^{31}Si ($\mathcal{T}_z = +3/2$), ^{31}P ($\mathcal{T}_z = +1/2$), ^{31}S ($\mathcal{T}_z = -1/2$), and ^{31}Cl ($\mathcal{T}_z = -3/2$), as shown in Fig. 5.1. It is a common technique to derive structural information of the nuclei by measurements of the isospin mirror nuclei, and their states with same isospin.

So far, only one measurement of the level structure of ^{31}Cl has been performed. The β^+-delayed proton decay of ^{31}Ar was used to extract different populated states in ^{31}Cl, see [39]. Of particular interest is the feeding of an $E_x = 0.75$ MeV level in ^{31}Cl, because a similar state at $E_x = 0.752$ MeV exists in the isospin mirror nucleus ^{31}Si with a spin-parity assignment of $J^\pi = 1/2^+$ [40]. This state is assumed to be the $\mathcal{T} = 3/2$ mirror state of the first excited state in ^{31}Cl.

It is important to collect detailed knowledge about the $\mathcal{T} = 3/2$ levels in each of the nuclei of the isospin quartet. For the $\mathcal{T}_z = \pm 3/2$ nuclei ^{31}Si and ^{31}Cl, the ground state mass excess and the mass excess of the first excited $\mathcal{T} = 3/2$ state needs to be known with high accuracy. In the $\mathcal{T}_z = \pm 1/2$ nuclei ^{31}P and ^{31}S, the mass excesses of the first and second excited $\mathcal{T} = 3/2$ states needs to be measured exactly, whereas the ground state is most probably a $\mathcal{T} =| \mathcal{T}_z |= 1/2$ state.

Assuming perfect isospin symmetry, the energies of the same isospin levels would be degenerate. Thus, exact knowledge about the energies of the levels in the isospin mirrors provided, it would be possible to derive the energy of the same isospin state in ^{31}Cl.
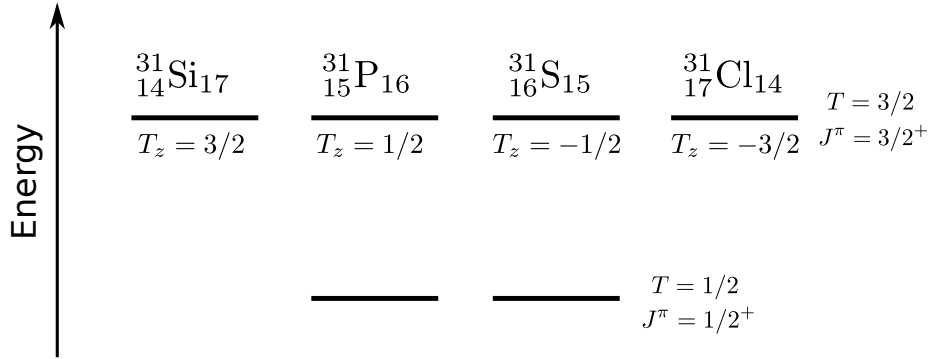
Figure 5.1: The $A = 31$, $\mathcal{T} = 3/2$ isospin quartet involves the $\mathcal{T}_z = \pm 1/2, \pm 3/2$ nuclei. Similar isospin mirror states are shown without the Coulomb displacement energy, which shifts the levels to different energies. If the strong interaction would be perfectly isospin symmetric, the levels would be degenerate, as indicated in the figure.

However, charge-dependent interactions affect the isospin symmetry.
Therefore, the Isobaric Multiplet Mass Equation (IMME, cf. [41], [42]) is an heuristic approach, which incorporates Coulomb interactions and charge-dependent displacement energies in the nuclear Hamiltonian. It can be used to derive mass excesses of similar isospin states, depending on the $\mathcal{T}_z$ projection of the isospin. The IMME for an isospin quartet is

$$\Delta(A, \mathcal{T}, \mathcal{T}_z) = a(A, \mathcal{T}, \mathcal{T}_z) + b(A, \mathcal{T}, \mathcal{T}_z) \cdot \mathcal{T}_z + c(A, \mathcal{T}, \mathcal{T}_z) \cdot \mathcal{T}_z^2, \qquad \boxed{5.1}$$

where Δ is the mass excess in keV, and a, b and c are parameters in keV, derived from corresponding fits to the isospin-dependent mass excesses of the isospin mirror states. It has been shown for many cases, that the IMME is valid for almost all isospin multiplets, and allows reliable predictions of the mass excess of the isospin mirror states.
In the case of ^{31}Cl, the known isospin $\mathcal{T} = 3/2$ in the multiplet states can be used to derive the excitation energy of the first excited state in ^{31}Cl. In a recent publication, the authors describe the extraction of the first excited $\mathcal{T} = 3/2$ state in ^{31}Cl by reevaluation of the newly measured mass excesses of the isospin mirror nuclei and their levels, see [43], and by using the IMME with a least-square fit. However, they point out, that the largest uncertainty arises from the mass excess of ^{31}S, for which information about the second excited $\mathcal{T} = 3/2$ state is still very poor. For the other isotopes of the $A = 31, \mathcal{T} = 3/2$ quartet, the masses are known with high accuracy.
In 2011, a new measurement of the mass and the half life of ^{31}S was performed by a group at the university of Jyväskylä, see [44]. They used β-delayed proton and γ decay from ^{31}Cl to derive precise values of the ground state, first and second excited $\mathcal{T} = 3/2$ state

mass excesses in ^{31}S. This extends the information about the masses, and the IMME calculation can be used to derive information about the first excited $\mathcal{T} = 3/2$ state in ^{31}Cl, as well as for the mass excess of the ground state.

Table 5.1: The isotopes of the $A = 31$, $\mathcal{T} = 3/2$ isospin quartet. Updated excitation energies E_x and mass excesses (ME) are used for the IMME input. The errors are taken from the indicated references.

Isobar	$\mathcal{T}_z$	Ground state ME [keV]	First E_x [keV]	Second E_x [keV]
^{31}Si	+3/2	-22949.01(4) [7]	-	752.43(10) [40]
^{31}P	+1/2	-24440.88(18) [7]	6380.8(17) [40]	7140.6(15) [40]
^{31}S	-1/2	-19042.55(24) [45]	6280.2(16) [44]	7033.5(13) [46]
^{31}Cl	-3/2	-7067(50) [7]	-	-

Tab. 5.1 shows the updated IMME input values, collected from different references. These values can be used to derive the mass excess of the first excited $\mathcal{T} = 3/2$ state in ^{31}Cl. This theoretical value can subsequently be compared to the measurement performed in this thesis. Tab. 5.2 and Fig. 5.2 shows the results of the fits to the data points of the IMME inputs.

The ground state mass excess for ^{31}Cl, resulting from the fit and the IMME, gives a small correction in comparison to the tabulated ground state mass excess from reference [7]. Furthermore, the mass excess of the first excited $\mathcal{T} = 3/2$ state can be calculated with formula 5.1 from the isobaric analogues in the multiplet. This corresponds to the first excited level in ^{31}Cl.

Table 5.2: The calculated IMME outputs for ^{31}Cl. All values are in keV.

	First quartet	Second quartet
a	-15462.3(19)	-14704.0(18)
b	-5297.7(11)	-5291.2(11)
c	204.3(12)	197.5(12)
Mass excess Δ	-7056.0(37)	-6322.8(36)

The resonance energy in the (^{30}S+p) system can be calculated by taking the mass difference of the proton, the ^{30}S ground state, and the results from the IMME calculation
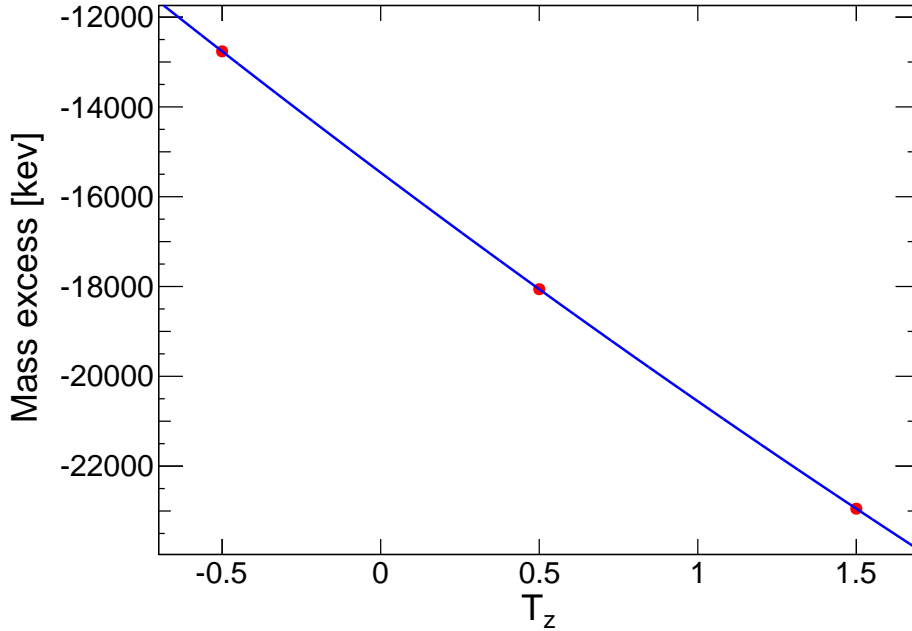
Figure 5.2: The updated mass excesses (red dots) are used in combination with the corresponding $\mathcal{T}_z$ values of the nuclei. The IMME equation is used for the fit to the data points for the first $\mathcal{T} = 3/2$ level in the isobars (blue line). The resulting parameters are listed in table 5.2.

by

$$E_r = \Delta(^{31}\mathrm{Cl},\ \mathrm{1st\ excited\ state}) - \Delta(^{30}\mathrm{S}) - \Delta(\mathrm{p}),$$

with $\Delta(\mathrm{p})$=7288.97 keV and $\Delta(^{30}\mathrm{S})$=-14062.5(30) keV (from [7]). This finally results in an energy of the first resonance in the (^{30}S+p) system of $E_r = 450.7(47)$ keV.

The ground state wave function of ^{31}Cl is composed of a $\nu[(s_{1/2})^2(1p_{3/2})^4(1p_{1/2})^2(1d_{5/2})^6]$ - $\pi[(s_{1/2})^2(1p_{3/2})^4(1p_{1/2})^2(1d_{5/2})^6(2s_{1/2})^2(1d_{3/2})]$ configuration, in which the single proton in the $l = 2$ orbital determines the spin and parity to be $J^\pi = 3/2^+$. Thus, in the single particle picture, a proton of the $\pi(2s_{1/2})^2$ shell is lifted up to the $(1d_{3/2})$ shell, leaving the first excited state with a single proton in the $(2s_{1/2})$ orbital.

However, only one experimental observation of the first excited state in ^{31}Cl exists so far and there is still structural information missing. In reference [43] the authors state, that "an observation of this level in the β^+-delayed proton decay of ^{31}Ar needs to be confirmed and acknowledged in an astrophysical context".

Reference [39] reports about an additional excited state in ^{31}Cl, measured by β-delayed proton decay at an excitation energy of $E_x = 1.749(5)$ MeV. The authors did not assign a spin or parity, because they did not identify a similar isospin mirror state in the iso-

bars. However, this state was later predicted from shell-model calculations in reference [47], and the excitation energy was assumed to be $E_x = 1.77$ MeV with a Q-value of 0.3 MeV for the ^{30}S$(p, \gamma)^{31}$Cl reaction. The authors assigned $l = 2$ ($J^\pi = 5/2^+$) to this resonance.

Tab. 5.3 summarizes the resonance parameters for the ^{30}S(p,γ)^{31}Cl reaction. The resonance strength $\omega\gamma$ is only dependent on the γ-width Γ_γ, because the proton partial Γ_p width is much bigger than Γ_γ, and $\omega\gamma \propto \Gamma_\gamma\Gamma_p/(\Gamma_p + \Gamma_\gamma)$. The values for the γ-widths are taken from reference [43]. The authors have adopted the values from life-time measurements of the corresponding analog states in the mirror nucleus ^{31}Si.

Table 5.3: Different resonance parameters for the ^{30}S(p,γ)^{31}Cl reaction. The references are given.

Energy [keV]	J^π (l)	Γ_γ [meV]	$\omega\gamma$ [meV]	Reference
461(15)	$1/2^+$ (0)	$0.86^{+0.60}_{-0.35}$	$0.86^{+0.60}_{-0.35}$	[43]
520	$1/2^+_1$ (0)	1.23	1.23	[47]
330(45)	$1/2^+_1$ (0)	0.48	0.46	[48]
451(5)	$1/2^+$ (0)	$0.86^{+0.60}_{-0.35}$	$0.86^{+0.60}_{-0.35}$	used in this work
1462(5)	$5/2^+$ (2)	$0.80^{+0.56}_{-0.33}$	$2.4^{+1.7}_{-1.0}$	[43], [39]
1109	$5/2^+_1$ (2)	0.4	1.2	[48]

There are different resonance parameters available, since a direct measurement of the excitation energies is not available so far. Especially, the deviation in reference [48] is interesting, because the authors also derived the excitation parameters from the IMME. The values do not agree within the 1σ uncertainties, which points to a major difference in the derivation of the values. A verification of the correct level energies and resonance parameters is therefore indicated.

The deduced updated mass excesses, shown in Tab. 5.2, can also be used to extract the reaction Q-value for the ^{30}S(p,γ)^{31}Cl reaction. So far, the recommended Q-value is 293(50) keV, see [7]. With the new adopted mass excesses and by usage of the IMME, a new Q-value can be derived to 283(3) keV, which is also close to the value of 284(7) keV quoted in [43].

5.1.1 Experimental results

The most direct approach to extract the energies of the excited states in the ^{31}Cl isotope is the investigation of the nucleus itself.

The first excited state of ^{31}Cl is of high interest, since it plays the dominant role in the proton-capture reaction ^{30}S(p,γ)^{31}Cl, which is important for the rapid proton-capture process (rp process). This process takes place on a matter accreting neutron star under very extreme conditions. The ^{30}S(p,γ)^{31}Cl reaction is believed to be of central interest in the low-mass region of the rp process, since it could serve as a bottleneck in the mass flow towards heavier elements. The reaction rate will be calculated in the following section of this chapter, and compared to previously calculated reaction rates.

The stellar reaction rate depends exponentially on the resonance energy, therefore it is important to know the resonance parameters with accuracy.

As already mentioned in the introduction of this thesis, the mixed beam consists of many different isotopes with similar A/Z ratio, thus, also the ^{31}Cl isotope was delivered with sufficient statistics.

Electromagnetic excitation

The incoming ^{31}Cl isotopes impinge on the high-Z target in the experimental setup and are excited in the highly-contracted Coulomb field of the lead target. Fig. 5.3 shows the energy distribution of the virtual photons for this particular case.
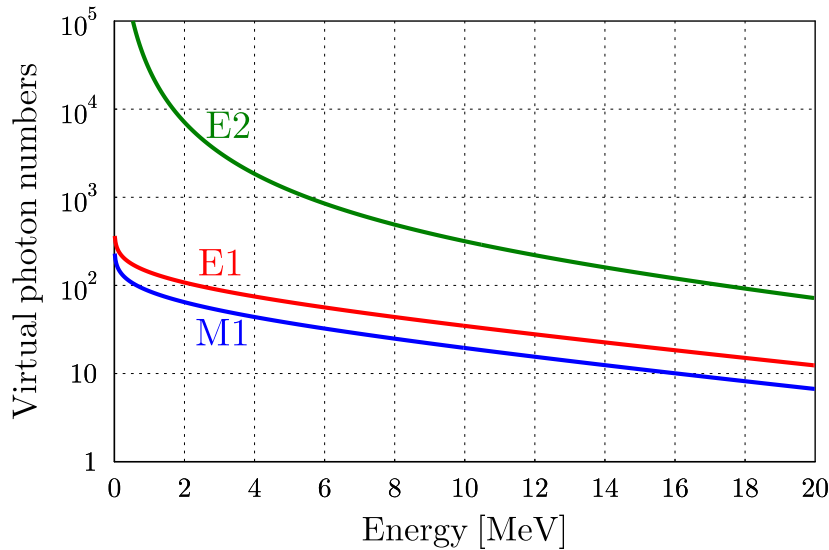
Figure 5.3: The virtual photon spectrum with different multipole contributions generated by the highly Lorentz-contracted field of a ^{208}Pb target, as seen by the incoming ^{31}Cl ions. The energy of the incoming ions is $E_{\text{beam}} = 630$ AMeV.

Especially at lower energies, a huge number of virtual photons exist to excite the nucleus. The dipole E1 and M1, and the quadrupole E2 virtual photons in the field couple to the ground state wave function of the incoming ions and excite them via allowed transitions

to different states. Since there are no bound states below the proton separation threshold ($S_p \approx 300$ keV) in ^{31}Cl, the decay will dominantly proceed via proton emission, leaving a ^{30}S ($t_{1/2} = 1.178(5)$ s, [38]) and a proton in the final state.

Both, fragment and proton momentum, can be measured and subsequently used to derive the excitation spectrum of ^{31}Cl. The tracker allows to calculate the momenta of the fragments and the protons, and the excitation energy E^* can be calculated on an event-by-event basis using the equation [49]

$$E^* = \sqrt{\sum_i m_i^2 + \sum_{i \neq j} \gamma_i \gamma_j m_i m_j (1 - \beta_i \beta_j \cos \Theta_{ij})} + E_\gamma - m_{projectile}, \qquad \boxed{5.2}$$

with the different particles i and j, the Lorentz factor γ_i and their velocities β_i, the corresponding angle of the trajectories Θ_{ij}, the masses m_i, and finally also the γ-ray energy E_γ.

The emission of a γ-ray occurs for instance, if an excited state in ^{30}S is populated after proton emission of ^{31}Cl. The first excited state known in this nucleus is a 2^+ level at an energy of 2.21 MeV above the ground state, see [38]. Assuming a population of the first two excited states in ^{31}Cl with the electromagnetic excitation with a total energy below the first excited state in ^{30}S, it is energetically not allowed to populate the 2^+ state.

Fig. 5.4 shows the measured γ-ray sum energy distribution in the Crystal Ball. It is a Doppler-corrected spectrum, with an add-back routine applied. The energy distribution follows the typical shape of an X-ray spectrum. These X-rays are produced by atomic interactions in the target material while the beam penetrates the target. However, this can be compared to the case, where no reaction takes place, and as can be seen in the figure, the normalized spectra have a similar shape. This proves the assumption, that the feeding of excited states and the subsequent transition to the ground state of ^{30}S is small, in fact below 5 % probability. Thus, the E_γ in the formula 5.2 can safely be neglected.

Another important aspect is the subtraction of contributions from nuclear reactions between projectile and target nuclei. As shown in the top part of Fig. 5.5, the nuclear background contribution is small compared to the pure electromagnetic excitation.

The bottom part of Fig. 5.5 shows the resulting excitation energy spectrum, calculated using formula 5.2 and measured in the experiment described in this thesis. A corresponding fit is also shown. This fit is composed of three Gaussian shapes. Two Gaussian fits are used to fit the peak structures at low-excitation energies below 2 MeV. The third Gaussian component describes the part above 2 MeV. This part reflects the direct capture component, where no resonance in the (^{30}S+p) system is populated. The direct capture is assumed to be of E1 nature.

The state at $E_x = 0.726(37)$ MeV is the $J^\pi = 1/2^+$ resonance, as discussed earlier in this section. The second resonance at an energy of $E_x = 1.731(82)$ MeV can be assigned to the $J^\pi = 5/2^+$ resonance, also found in the β-delayed proton decay measurement
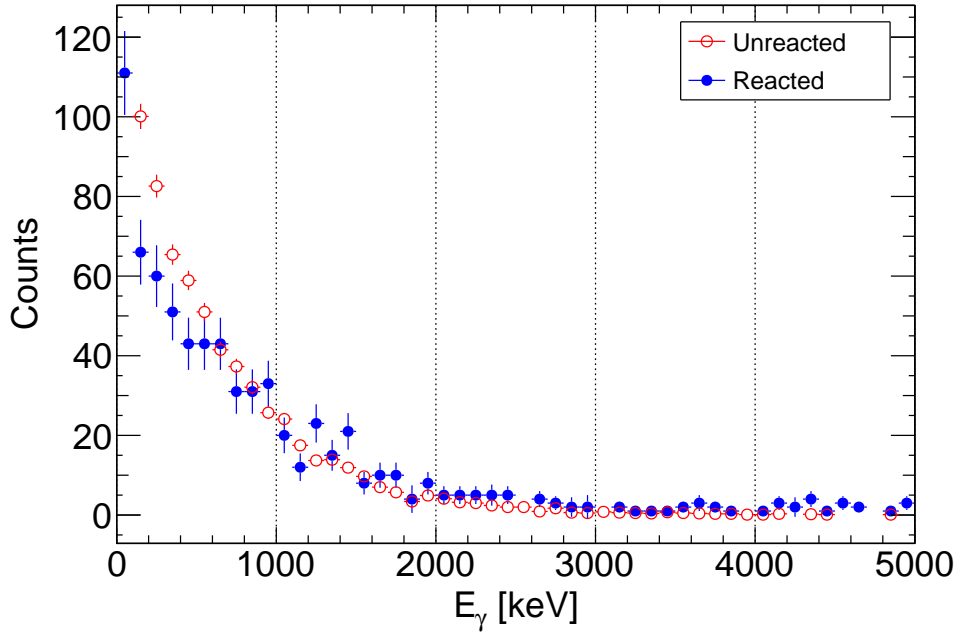
Figure 5.4: The γ-sum spectrum in the case of incoming ^{31}Cl, with a subsequent reaction to ^{30}S (red open dots). The background is taken from the unreacted beam on the same target, normalized to the same number of incoming ions (blue solid dots). The γ spectrum shows no significant contribution from any excited state fed in the ^{30}S ejectile nucleus.

[39]. The Gaussian widths of the fits are $\sigma = 220(50)$ keV and $\sigma = 275(80)$ keV, which reflects purely the known experimental resolution of the measurement.

Table 5.4: The excitation energies of ^{31}Cl extracted in this work, compared to the IMME calculations with updated masses, and from [43]. The ground state has a $J^{\pi} = 3/2^{+}$ configuration.

J^{π}	Energy [MeV]	Reference
$1/2^{+}$	0.726(37)	this work
$1/2^{+}$	0.733(6)	updated IMME calculation
$1/2^{+}$	0.745(16)	[43]
$5/2^{+}$	1.731(82)	this work
$5/2^{+}$	1.746(7)	[43]
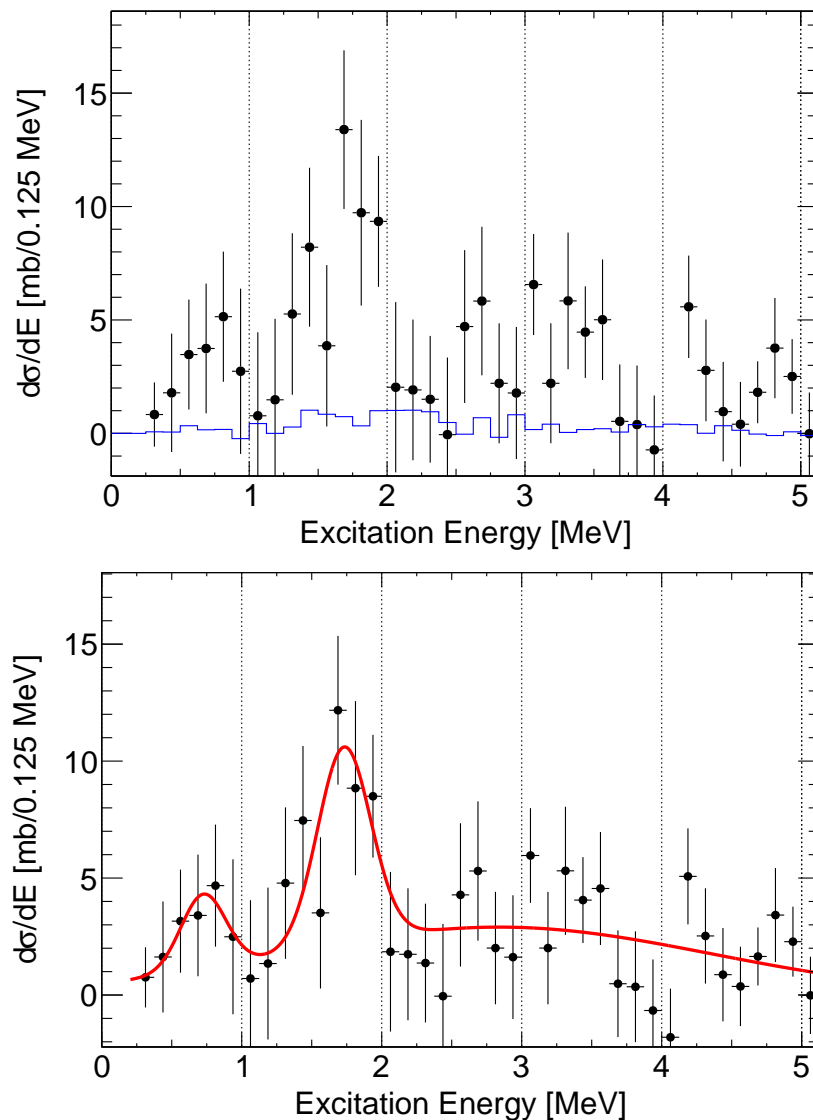
Figure 5.5: Top: The background subtracted excitation energy spectrum, extracted from the measurement on the lead target is presented together with the nuclear contributions, extracted from a measurement with a carbon target. Nuclear contributions are small compared to the electromagnetic excitation part. Bottom: The final excitation spectrum of ^{31}Cl. Two low-lying resonances can be seen, together with a large direct break-up part at higher excitation energies. A corresponding fit is shown, from which the parameters of the excited states can be derived. The error bars reflect the statistical uncertainties.

In a recent publication, the results of a Coulomb dissociation experiment performed at the RIKEN institute in Japan are reported, see [50]. The ^{31}Cl$(\gamma,$p$)^{30}$S reaction at lower beam energies ($E_{\text{beam}} = 58$ AMeV) was investigated. Two resonances and a direct capture E1 component were observed. The resonance energies in the (^{30}S+p) system, stated in [50], are $E_r = 0.45$ MeV and $E_r = 1.3$ MeV. Thus, they are in good agreement with the resonance energies deduced in this work.

Moreover, in the theory of electromagnetic excitation, the matrix elements couple to states with certain spin parity assignments, and subsequently, the selection rules can be used to determine the nature of the transition. In this case, since the ground state is composed of a $J^{\pi} = 3/2^+$ character, the dominant excitation modes are E2 and M1 transitions to the first excited state. Thus, another important step is to disentangle the separate contributions. This requires a detailed reaction model and can not be performed in the framework of this thesis. Furthermore, the angular correlations must be analyzed to finally decompose the M1 and E2 parts.

However, good agreement is also archived with the data from the IMME calculation. This agreement justifies the calculated and measured resonance energies and can thus be used to extract the reaction rate for the ^{30}S$($p$,\gamma)^{31}$Cl reaction. This will be done in the following chapter. Table 5.4 summarizes the results and compares them to the IMME calculation, performed in the previous section.

5.1.2 Partial cross sections

The energy-differential excitation spectrum is used to extract the break-up cross sections for the two different states in ^{31}Cl. The integral over the Gaussian fits yields the partial cross sections to the respective components. However, the partial cross sections consist of contributions from M1 and E2 excitations. In order to extract the amount of E2 and M1 parts contributing to the partial cross sections, a theoretical description of this particular Coulomb dissociation reaction needs to be employed. The partial cross sections are 15(6) mb for the first excited state, and 30(9) mb for the second excited state. Table 5.5 summarizes the resulting cross sections.

Table 5.5: The partial Coulomb dissociation cross sections for the two resonances in ^{31}Cl. The dominant error source is the low statistics. Systematical errors of about 10 % (see detailed discussion in the next chapter) can be neglected here.

J^{π}	Cross section [mb]
$\frac{1}{2}^+$	15(6)
$\frac{5}{2}^+$	30(9)

5.1.3 Reaction rate and X-ray bursts on neutron stars

The improved resonance energies can be used to better estimate the ^{30}S(p,γ)^{31}Cl reaction rate under stellar conditions. This is of special importance for the rapid proton-capture process, since it could serve as a bottleneck reaction in the mass flow towards heavier elements. So far, the calculated reaction rate was purely based on theoretical estimates, like shell-model based calculations in [47], or via including the mirror states in similar isospin nuclei, like in the IMME [43].

The stellar reaction rate calculations performed by Iliadis et al. in [48] show severe deviations from the calculated ones performed by other groups, and experimental justifications were still missing.

The ^{30}S(p,γ) reaction can be described by resonant capture into the two low-lying very narrow resonances in the (^{30}S+p) system to the ground state of ^{31}Cl. This process is described by

$$N_A \langle \sigma v \rangle = 1.54 \times 10^{11} (\mu T_9)^{-3/2} \sum_r (\omega\gamma)_r \times e^{-11.605 E_r / k_B T_9} \ [cm^3 s^{-1} mol^{-1}] \qquad \boxed{5.3}$$

with N_A being the Avogadro number, μ the reduced mass, T_9 the temperature in GK, k_B the Boltzmann constant, and E_r the resonance energy. Of special importance is the strength of the resonance, here denoted with $\omega\gamma$, which can be determined by a statistical factor and the width of the resonances via

$$\omega\gamma = \frac{(2J_r + 1)}{(2J_p + 1)(2J_S + 1)} \left(\frac{\Gamma_p \Gamma_\gamma}{\Gamma} \right). \qquad \boxed{5.4}$$

Here, J_p, J_r and J_S are the spins of the proton, the resonance and the reactants. Furthermore, the sum of the proton partial width Γ_p and the γ-decay partial width Γ_γ is the total width $\Gamma = \Gamma_p + \Gamma_\gamma$. Since $\Gamma_p \gg \Gamma_\gamma$ for a narrow resonance, the resonance strength is dominated by the γ-decay partial width.

Formula 5.3 allows to calculate the reaction rate for the two narrow resonances. The resonance strength parameters are taken from Tab. 5.3. The derived energies are used as E_r parameters in the calculation.

Furthermore, the direct capture component needs to be investigated. Since this process proceeds through a non-resonant capture of E1 type, the general formula for non-resonant capture can be used and adopted for proton captures to

$$N_A \langle \sigma v \rangle_{NR} = 7.83 \times 10^9 \left(\frac{Z}{\mu T_9^2} \right)^{1/3} S_{eff}(E_0) e^{-4.29 \left[\frac{Z^2 \mu}{T_9} \right]^{1/3}} \qquad \boxed{5.5}$$

from reference [47], where Z is the charge of the reactant. $S_{eff}(E_0)$ is used for the astrophysical S-factor, which varies only very little for non-resonant captures. Therefore, an expansion of $S_{eff}(E_0)$ is possible, yielding

$$S_{eff}(E_0) = S_0 [1 + \alpha_1 T^{1/3} + \alpha_2 T^{2/3} + ...] \qquad \boxed{5.6}$$
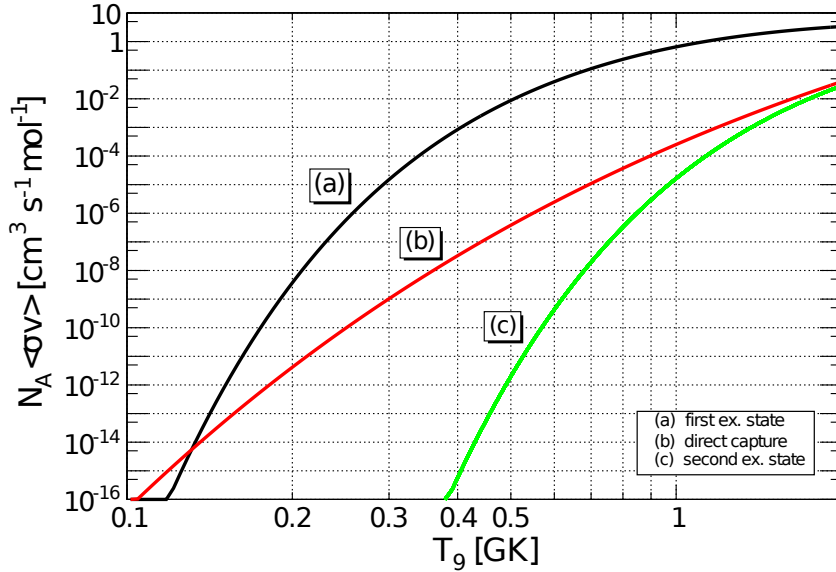
Figure 5.6: The reaction rate for the important ^{30}S(p,γ)^{31}Cl bottleneck reaction in the rp process. Shown is only the part for the relevant temperature range. Maximum peak temperatures in the rp process are typically around 2 GK. Three contributions can be seen, from (a) the low-lying resonance, (b) the direct capture, and (c) the second excited state in ^{31}Cl.

with corresponding α_i coefficients. Here, it is sufficient to consider only the leading terms $S_{eff}(E_0) \approx S_0 + S_0\,\alpha_1\,T^{1/3}$ and insert this into equation 5.5. S_0 is the Taylor-expanded S-factor for the energy E = 0, and is given in the unit of MeV b. For the calculation, S_0 is taken from reference [47] for this particular reaction, and is 5.14×10^{-3} MeV b. The factor α_1 is taken from the Taylor expansion and is $\alpha_1 = 9.81 \times 10^{-2}(Z^2\mu)^{-1/3}$. Finally, the total reaction rate is a sum of the three single components, with

$$N_A\langle\sigma v\rangle = N_A\langle\sigma v\rangle_1 + N_A\langle\sigma v\rangle_2 + N_A\langle\sigma v\rangle_{NR}. \qquad (5.7)$$

Fig. 5.6 shows the calculated reaction rate with its three components. The temperature range corresponds to the typical temperatures reached during an X-ray burst of type I. Clearly, the first resonance dominates the reaction rate, and even at temperatures of $T_9 \approx 2$ GK, the contributions from direct capture and capture to the second excited state is only on a level of 1 %. The rate can be compared to a reaction rate calculation performed by Wallace and Woosley in the year 1982, cf. [51], taking into account only one resonance in the (^{30}S+p) system at an energy of $E_r = 453$ keV with a partial γ-width of 9.1×10^{-4} eV.
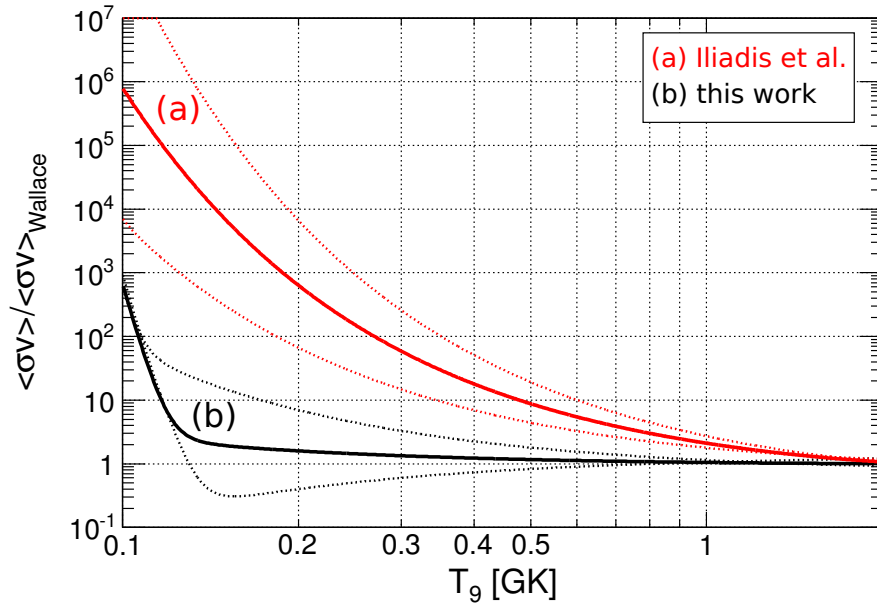
Figure 5.7: Comparison of the reaction rates derived in this work (black line) and Il-
iadis et al. (red line), relative to the reaction rate calculated by Wallace
and Woosley in the year 1982. Especially in the low-temperature region,
a deviation of up to 4 orders of magnitudes is observed. The uncertainty
bands (black dotted lines) for this work is the total uncertainty, including all
errors of the resonance parameters. The uncertainty bands for the rate from
Iliadis et al. (red dotted lines) are only determined from the uncertainty in
the energy of the first excited state, which dominates the total rate.

Furthermore, the rate can be compared to the rate given by Iliadis et al. in [48]. A
deviation is observed in the calculated relative reaction rate (relative to the rate from
Wallace and Woosley), especially at low temperatures. Fig. 5.7 shows the result of this
comparison. Above $T_9 = 0.2$, the rate from Wallace et al. and this work agrees within
a factor of 2.

5.2 The case of ^{32}Ar

^{32}Ar has a half life of $t_{1/2} = 100.5(3)$ ms, and a ground state configuration of $J^\pi = 0^+$ (see
[38]). The one proton separation energy is $S_p = 2.4$ MeV, and the two proton separation
energy is $S_{2p} = 2.7$ MeV. The separation energy for a neutron is $S_n = 21.75$ MeV. Since
there are no bound excited states in ^{31}Cl, a major part of the excited ^{32}Ar isotopes
decay via two proton emission to the (^{30}S+2p) system. However, a small amount of
direct decays to the ground state of ^{31}Cl is also expected. The 1p channel will be
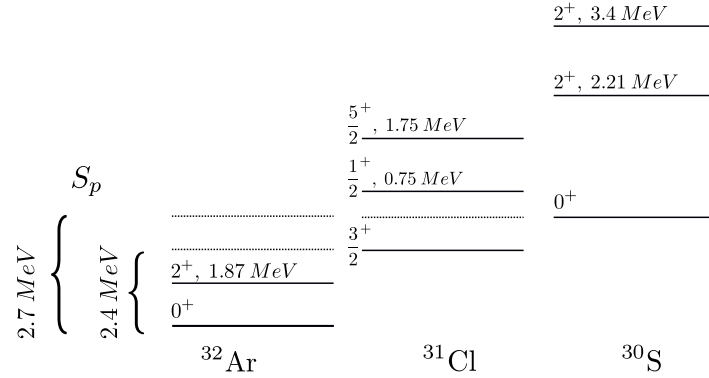
Figure 5.8: The energy relations between the different isotopes in the ^{32}Ar case. Since the separation energies are small, even higher proton evaporation channels can be reached. In this thesis, the one- and two-proton evaporation channels are analyzed.

investigated in the next section. Fig. 5.8 shows the energy relations and the known states of the different isotopes.

5.2.1 Two proton channel

Two dimensional cuts in Fig. 4.19 allows the selection of the desired reaction channel. The tracking algorithm is performed to disentangle products with same charge, but different masses.

The retrieved masses are used to extract an inclusive, integrated cross section σ by relating the reaction probability p, the target areal density d, the target molar mass M_m, and the Avogadro number N_A by

$$\sigma = p \cdot \frac{M_m}{d \cdot N_A}.$$
(5.8)

Here, p is calculated via

$$p = \frac{N_{reacted}}{N_{incoming}}.$$
(5.9)

However, background components from break-up in materials other than the target are still present to a certain extend. To subtract the background contribution properly, this break-up is measured in runs without an inserted target. In the analysis, it is important to apply the same conditions and cuts, as for the runs with target, involving the same efficiencies.

Moreover, there is another important effect arising from the nuclear contribution from

the reaction on the heavy lead target. For this reason, a run with a ^{12}C target is investigated. The nuclear contribution to the pure electromagnetic cross section is determined with this ^{12}C target. This is then, after scaling, subtracted from the cross section, which was extracted for the ^{208}Pb target. This results in the Coulomb dissociation (C.D.) cross section.

The subtraction of the nuclear contribution requires a proper scaling, which incorporates the different nuclear radii of the different target nuclei. In terms of the cross section, it is

$$\sigma_{Pb}^{\text{nuclear}} = \alpha_T \sigma_C, \tag{5.10}$$

with α_T being the nuclear scaling factor. In the simplest approach, α_T can be calculated by employing the black-disk model by

$$\alpha_T = \frac{A_{^{32}\text{Ar}}^{1/3} + A_{\text{Pb}}^{1/3}}{A_{^{32}\text{Ar}}^{1/3} + A_{\text{C}}^{1/3}}, \tag{5.11}$$

involving the nuclear mass A of the incoming ^{32}Ar isotopes, the lead target, and the carbon target. Inserting the masses results in a nuclear scaling factor of

$$\alpha_T = 1.67. \tag{5.12}$$

Of course, there are more acurate approaches to describe the problem of the nuclear contribution. A semi-classical model in [52] incorporates a density distribution of the target and the projectile by introducing a factor a in

$$\alpha_T = \frac{1 + a \cdot A_{Pb}^{1/3}}{1 + a \cdot A_C^{1/3}}. \tag{5.13}$$

However, there are several additional approaches to extract the factor α_T. In this thesis, the factor is deduced using the experimental data itself, and will be explained in the following section.

Finally, the resulting Coulomb dissociation cross section can be expressed by

$$\sigma_{C.D.} = p_{Pb} \left(\frac{M_m(Pb)}{d_{Pb} N_A} \right) - p_C \left(\alpha_T \frac{M_m(C)}{d_C N_A} \right) - p_{\text{empty}} \left(\frac{M_m(Pb)}{d_{Pb} N_A} - \alpha_T \frac{M_m(C)}{d_C N_A} \right). \tag{5.14}$$

Inclusive cross section

The isotope ^{32}Ar has a neutron separation threshold of $S_n = 21.75$ MeV, which is well above the adiabatic cutoff energy of the virtual photon spectra. Therefore, all contributions to the final mass spectrum involving neutron evaporation, are induced by nuclear reactions. Indeed, in the mass spectrum of isotopes in the final state of the
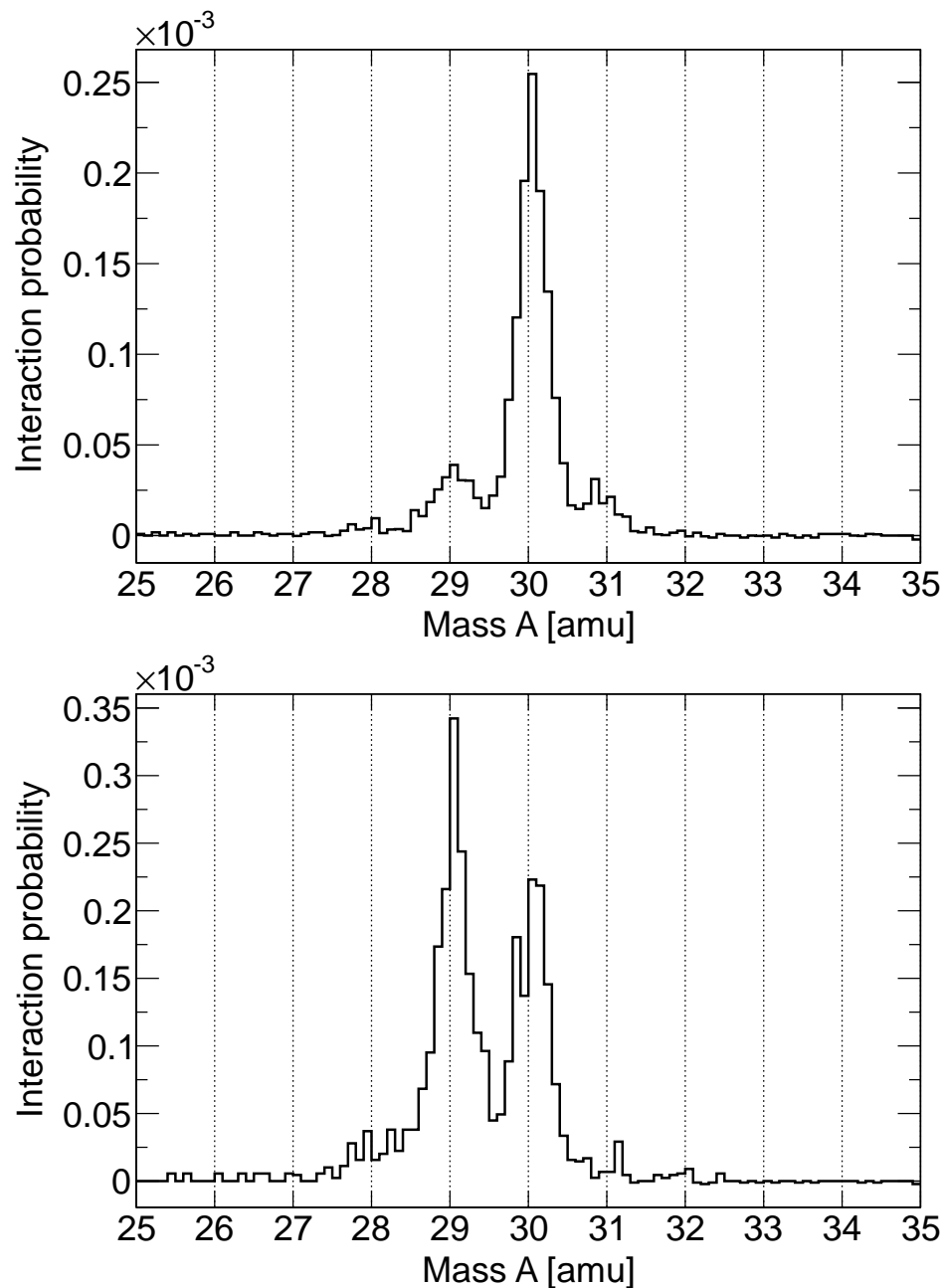
Figure 5.9: Top: Mass spectrum for the lead target. ^{30}S, produced in the two proton emission channel, is dominating. The peak at larger masses stems from contamination of the cut, and displays a wrongly tracked reaction channel. The ^{29}S contribution is produced from nuclear reactions, as described in the text. Bottom: The same mass spectrum measured with the carbon target.

^{32}Ar(γ,2p) reaction channel, a contribution from ^{29}S is visible, shown in the top part of Fig. 5.9 for the measurement with a lead target.

As already mentioned, this isotope can only be produced in nuclear reactions and is therefore a well-suited observable to extract the α_T factor from the experimental data. Here, the runs with a carbon target are used, assuming, that most interactions with ^{12}C will be nuclear reactions. Thus, the integral of the production cross section of ^{29}S in the carbon target and the lead target can be scaled to each other, yielding the α_T factor with equation 5.10.

After applying the correct α_T factor, the nuclear background contribution should vanish, if the mass spectra are properly scaled, and subsequently subtracted. Fig. 5.10 shows the result of the subtraction. As can be clearly seen, the contribution of ^{29}S vanished, yielding an α_T factor of

$$\alpha_T = 1.79(10), \tag{5.15}$$

which is in very good agreement with the calculated $\alpha_T = 1.67$, derived from the black-disk model described above.

An additional source of systematical uncertainties should be noted at this point, arising from the calculation of the α_T factor. As mentioned above, there are different possible models available to calculate the nuclear scaling factor. The derived value is in good agreement with the simple back-disk approach. More accurate models can be employed, yielding different values for α_T. However, the total contribution of the nuclear background to the integrated Coulomb dissociation cross section is around 15 %. The variation of α_T between the models is around 10 - 20 %, which means, the total systematical uncertainty is only approximately 1.5 - 3 % and can, therefore, be neglected.

In order to extract the inclusive Coulomb dissociation cross section of the ^{32}Ar(γ,2p)^{30}S reaction, the mass spectra, extracted from the lead and carbon target, with the derived α_T factor are scaled to target thicknesses and the incoming unreacted ions, and subsequently subtracted, according to equation 5.14. This is performed neglecting the entire proton branch to avoid any efficiency and acceptance effects of the proton branch. It is purely based on the tracking algorithm, and the reaction propability p can be expressed by

$$p = \frac{N_{reacted} \cdot \epsilon_1}{N_{incoming} \cdot \epsilon_2}, \tag{5.16}$$

with N being the number of reacted and incoming ions, and ϵ denotes the correspondingly involved detector efficiencies. An important task is the determination of the efficiencies. However, in this case, the graphical cuts, performed on the same detectors, have the same efficiencies for both components, and they cancel in equation 5.16.

Another important systematic uncertainty arises from the two-dimensional cut, used to isolate the reacted and unreacted ions. The contribution from other reactions to the
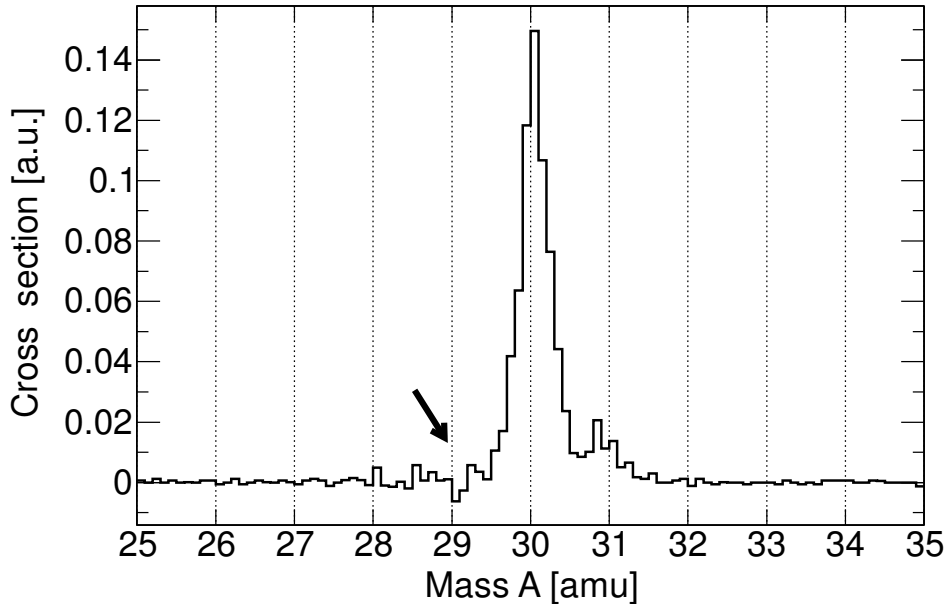
Figure 5.10: Mass spectrum with a subtracted and scaled carbon contribution. As expected, the nuclear contribution vanishes.

applied cuts was investigated. As can be seen in the mass distribution in the top part of Fig. 5.9, there is a small contamination from another reaction channel. In this case, the peak around 30.9 amu indicates, that the tracking algorithm tracks ($A_1 = 29$, $Z_1 = 15$) ions with a wrong charge $Z_2 = 16$, according to

$$A \;=\; \frac{Z_2}{Z_1} \cdot A_1 \tag{5.17}$$

$$A \;=\; \frac{16}{15} \cdot 29 = 30.9 \text{ amu.} \tag{5.18}$$

In the tracking algorithm, the charge Z is fixed. Moreover, the charge is clearly constrained with the cut on the energy-loss detectors, but, however, the tails from neighboring charges still contribute to a small amount to the two-dimensional cut. Considering the estimations above, the wrongly tracked ions can be used to extract these contaminations in the cut. Therefore, the overlap of the gaussian distribution of ^{30}S and the wrongly tracked isotopes within 2σ is taken, and the ratio is used to derive the extend of the contaminations. In this case, the contributions from contaminations are below 5 %. Furthermore, within 2σ, both distributions are still separated (95.4 % confidence level). This shows, that the contamination of the cut leads to a small systematical uncertainty and can be handled properly.

Using two-dimensional cuts in the analysis also conceals another source of systematical

errors. Besides the contamination part, the final cross section is assumed to be independent of the cut sizes. However, if a cut is too big, it also includes too much background and contamination from other reaction channels. Applying very small cuts usually lead to bigger statistical uncertainties. In this experiment, the cut sizes are chosen in the following way to avoid a significant systematical uncertainty. In general, the cut on the unreacted and reacted beam has the same size. This avoids different cut efficiencies, or at least, the systematical uncertainty gets so small, that it can be neglected. Moreover, the cut size is chosen according to the energy resolution of the detectors $\sigma_{\Delta E} \propto \sqrt{E}$ of the investigated charges. The cut on unreacted ^{32}Ar with Z = 18 is selected smaller than the cut on the outgoing ^{30}S with Z = 16, due to the resolution effects.

A study of different cut sizes was performed and a systematical uncertainty in the integral cross section of about 8 % is observed. The statistical errors play a dominant role, since for the down-scaled fragment trigger without any reaction trigger involved, the statistics drops down and introduces an error of around 14 %.

Another systematic uncertainty is related to the error in the areal density of the target (lead and carbon), which is below 2 %, and thus negligible, see [53].
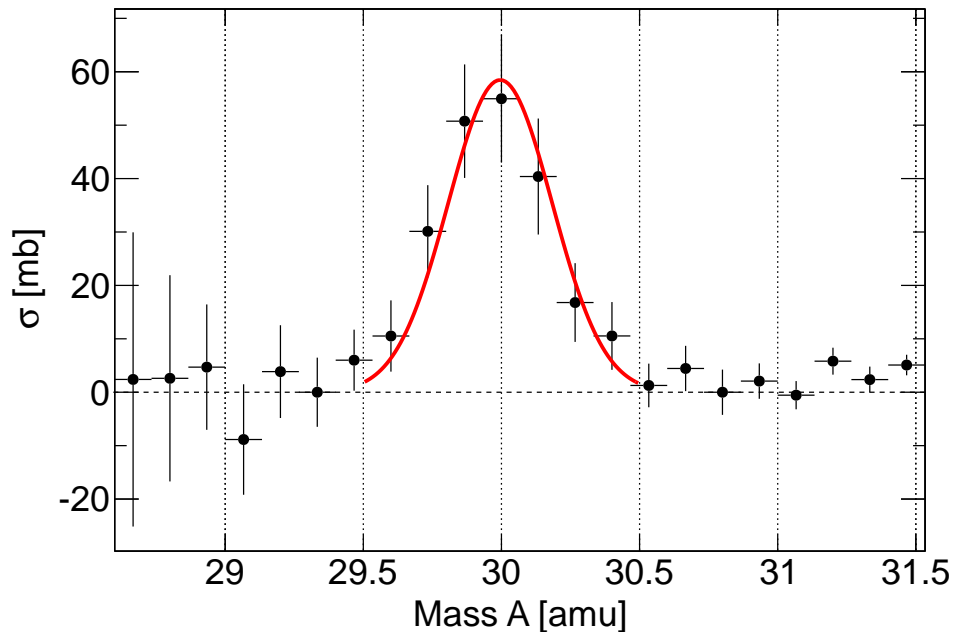
Figure 5.11: The mass spectrum for the ^{32}Ar(γ,2p)^{30}S reaction from Coulomb excitation. The spectrum is normalized to the numbers of incoming ions. Background and nuclear contributions are properly scaled and subtracted. The Coulomb cross section spectrum is derived. The ^{30}S peak is well described with a Gaussian fit.

Fig. 5.11 shows the final mass distribution after subtracting the background and the nuclear contributions. A Gaussian fit is applied (red line in Fig. 5.11). The error bars reflect purely the statistical errors of the measurement. The integrated Coulomb dissociation cross section can be derived by integration of the distribution. The integration results in a cross section of

$$\sigma_{C.D.} = 214(29^{\text{stat}})(20^{\text{sys}}) \text{ mb}.$$

Table 5.6: Different error sources for the inclusive cross section measurement. The statistical uncertainty dominates the total uncertainty.

Total C.D. cross section	214 mb	Inclusive measurement
Δ_{stat}	14 %	
Δ_1^{sys}	1.5 %	α_T factor
Δ_2^{sys}	< 5 %	cut contamination
Δ_3^{sys}	8 %	cut variation
Δ_{total}^{sys}	9.6 %	total

Exclusive measurement

The setup is able to perform exclusive measurements and from this, the excitation energy spectrum can be reconstructed. In the case of ^{32}Ar(γ,2p), the reconstruction is more difficult than in the ^{31}Cl(γ,p) case, since two protons need to be measured and the trajectories extracted.

However, the two protons are measured in the proton branch, and thus, different corrections need to be considered. As already mentioned in the analysis chapter of this thesis, an efficiency correction needs to be applied to the excitation spectrum, stemming from a detection inefficiency of the proton branch. Moreover, because of geometrical constraints, there is also an acceptance correction for the protons necessary. This is especially important for higher excitation energies, since the momenta are higher and thus, the protons could be cut.
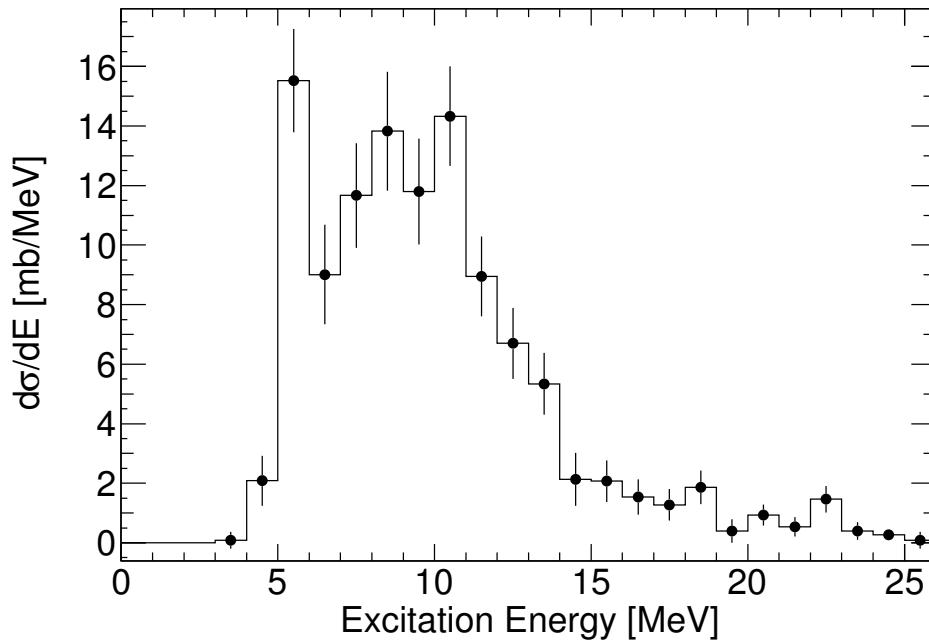
Figure 5.12: The background subtracted excitation spectrum of ^{32}Ar, derived from the two proton evaporation channel. No acceptance correction is applied and the contributions from γ-rays are not taken into account.

Fig. 5.12 shows the excitation energy spectrum derived from equation 5.2 before the acceptance correction. The efficiency for detecting two protons is 35(4) % (see chapter 4). The performance of the Crystall Ball can be evaluated with a Monte-Carlo type simulation of the X-ray background, produced in the target by molecular and atomic reactions, while the beam traverses the target. Therefore, a special X-ray event generator, based

on the simulated atomic interactions in the lead target, is used, cf. [54]. The event generator is subsequently incorporated into the R3BROOT frame work, in which the full setup of the Crystal Ball is included.

As can be seen from Fig. 5.13, the experimental data and the simulation agrees very well. The deviations can be explained by missing material (like cables, DSSSDs), so far not included in the simulation. However, the general distribution is nicely reproduced, proving, that the X-ray background is understood.

Fig. 5.14 shows the measured γ-sum spectrum for ^{30}S. In the spectrum, the X-ray background from the unreacted beam is also shown, scaled, and compared to the measured γ-ray sum energy for the reacted beam. Indicated is the transition from the 2^+ state to the 0^+ ground state in the heavy residual ^{30}S with an energy of 2.2 MeV. However, the transition is not very strong, only approximately 0.5 % of the decays proceed via this transition to the ground state of ^{30}S.

Fig. 5.15 shows the excitation energy spectrum, derived from ^{32}Ar$(\gamma,2\text{p})^{30}$S. All corrections are applied, and the γ-sum energy is added. Applying

$$\sigma_{C.D} = \int \frac{d\sigma}{dE} dE, \qquad (5.19)$$

the integrated cross section can be derived and yields

$$\sigma_{C.D.} = 226(14^{\text{stat}})(23^{\text{sys}}) \text{ mb}, \qquad (5.20)$$

which is in very good agreement with the cross section extracted from the inclusive mass measurement discussed in the previous section. This proofs, that the corrections are reliable and can be applied for other reaction channels as well.

The statistical errors are smaller when extracting the cross section from the exclusive measurement, because the evaluation involves data taken with the reaction triggers, which are not downscaled. In general, the cuts are similar as in the case of the inclusive data analysis. Systematical errors, introduced by mistracked protons, are very small. For less than 1 % of all tracked protons, the proton trajectories were falsely identified by the tracker. This effect can be neglected.

The systematical uncertainty arises dominantly from the errors of the detection efficiency for two protons. The probability, that two protons are identified as only one proton, is small (see chapter 4). Even for the lowest excitation energies, less than 4 % of the events are misidentified.

Tab. 5.7 shows the different identified error sources for the exclusive measurement. Within the errors, the derived cross sections from the two different methods are in excellent agreement.

5.2.2 One proton channel

Because of the small difference in the binding energy for the 1p and the 2p removal channel, only small cross section contributions from the ^{32}Ar$(\gamma,\text{p})^{31}$Cl reaction is expected.
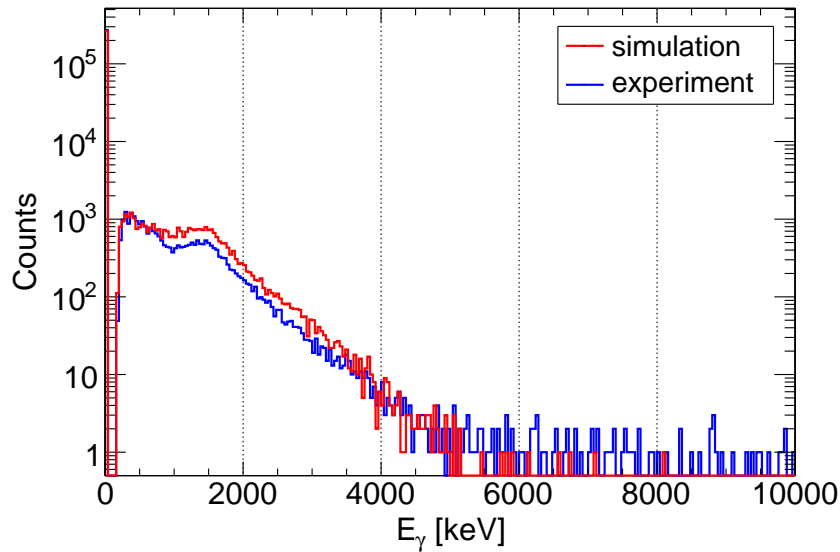
Figure 5.13: The simulated (red) and measured (blue) X-ray background in the γ-sum spectrum from the Crystal Ball in the case of an incoming ^{32}Ar isotope, passing through a lead target. The shape of the distributions is in good agreement, however, it can be seen, that the measured distribution is lower, which is attributed to a missing efficiency effect of the simulation. In the simulation less material is incorporated, which leads to less absorption.
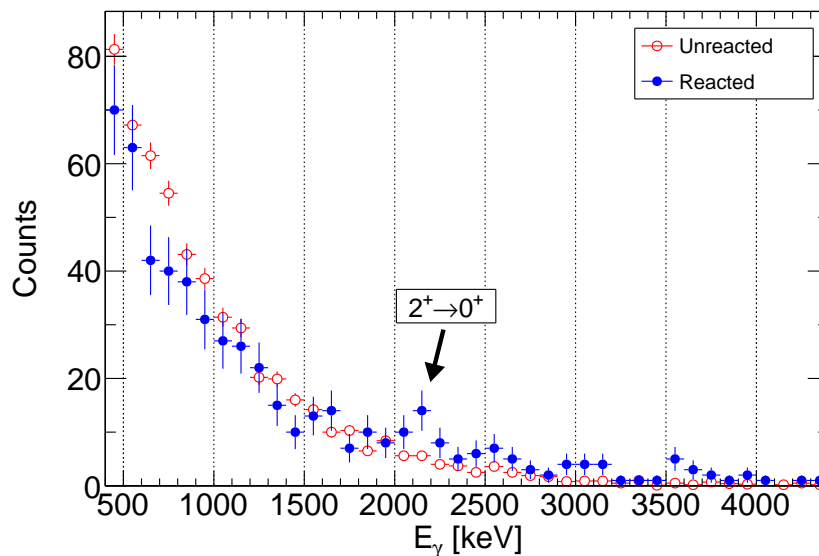
Figure 5.14: The γ-sum spectrum shows the $2^+ \to 0^+$ transition in ^{30}S. The background is extracted from unreacted beam and scaled to the number of incoming ions. In general, the spectrum derived with reacted beam follows the background contribution very well, showing no other considerable γ-transitions.
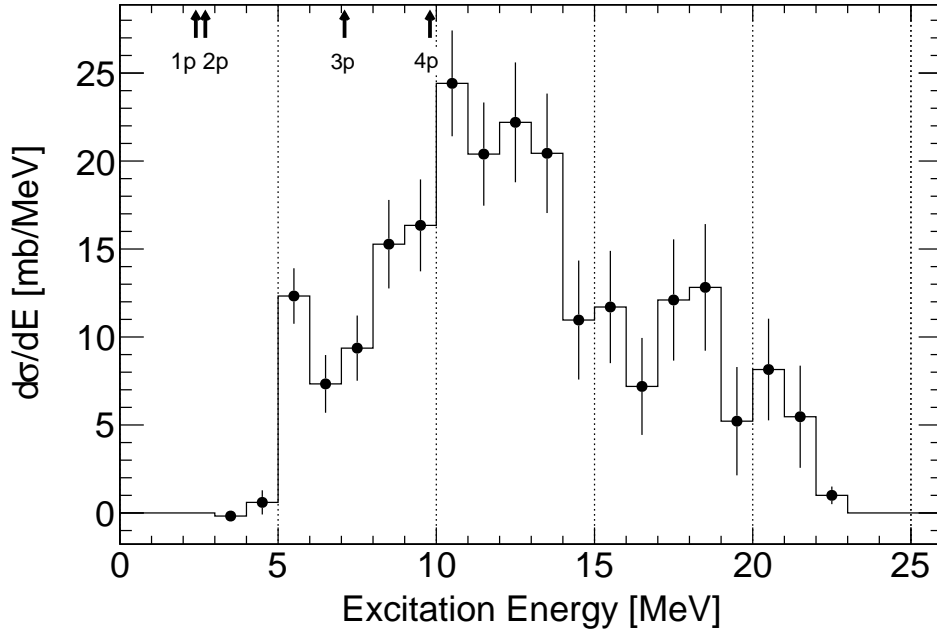
Figure 5.15: The excitation spectrum of ^{32}Ar, derived from the ^{32}Ar(γ,2p) reaction. All corrections are applied, and the γ-sum energy is added. The arrows indicate the different proton separation thresholds.

Table 5.7: Different identified error sources for the exclusive Coulomb dissociation cross section.

Total C.D. cross section	226 mb	Exclusive measurement
Δ_{stat}	6.2 %	
Δ_1^{syst}	< 1 %	Trigger inefficiency
Δ_2^{syst}	10 %	Efficiency correction
Δ_{total}^{sys}	10 %	total

The derived excitation spectrum from the 2p channel, see Fig. 5.15 does not open at the corresponding 2p separation energy of $S_{2p} = 2.7$ MeV, but around 4 MeV. Due to the Coulomb barrier, the strength is still found in the 1p channel, although the excitation energy exceeds the 2p binding energy.

By applying a proper cut on the expected ^{31}Cl events in Fig. 4.19, and selecting the data with only one tracked proton, some events can be identified and related to the 1p reaction channel. In order to extract the Coulomb dissociation cross section for this

channel, the exclusive procedure as in the 2p case is used. However, the statistics is low, and the usage of a down-scaled trigger (like the fragment trigger), followed by a reconstruction of the mass spectra is not possible.

In this case, the determination of the Coulomb dissociation cross section is performed using the exclusive measurement only. It is proven for the 2p channel, that the two measurements deliver consistent results. Moreover, the applied corrections for the proton branch, like the acceptance and efficiency correction, are working reliable, as also proven in the 2p case.
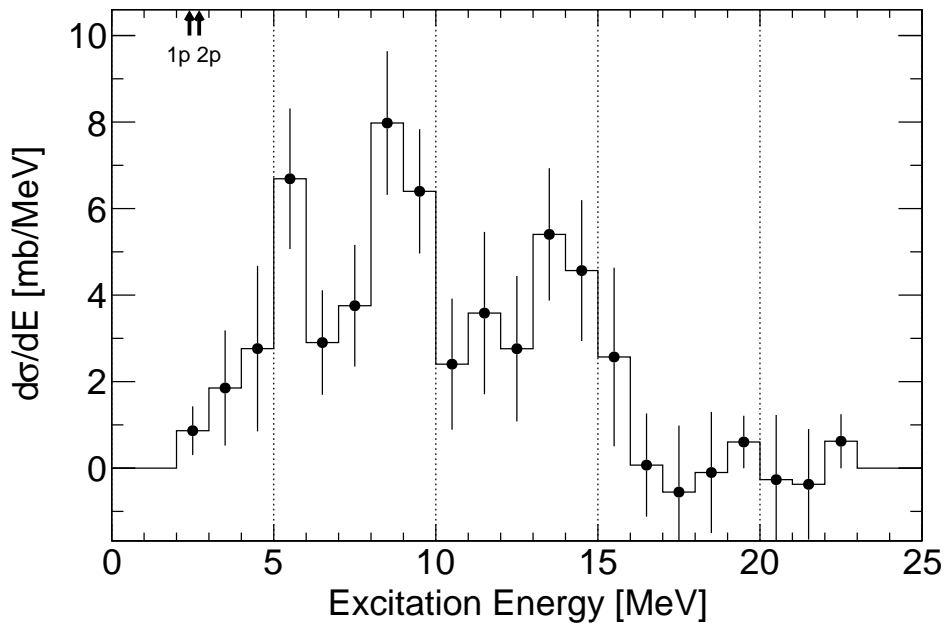
Figure 5.16: The background subtracted Coulomb excitation energy spectrum for ^{32}Ar, derived from the 1p channel. Efficiency and acceptance corrections are applied. Statistical errors are displayed.

The one-proton separation energy in ^{32}Ar is $S_p = 2.4$ MeV. The protons overcome the Coulomb barrier, since there are no competing decay channels present at this low energy. The excitation energy spectrum opens at the separation threshold, as displayed in Fig. 5.16. The γ-sum energy is not added in this case. The number of events with measured γ-rays is below 5 % of all data, and, therefore, is neglected for the final analysis. The total Coulomb dissociation cross section is obtained from integration of the Coulomb excitation spectrum. The value is

$$\sigma_{C.D.}^{1p} = 54(8^{\mathrm{stat}})(6^{\mathrm{sys}})\,\mathrm{mb}.$$

Here, the statistical error is larger than the systematical uncertainty, which was taken from the previous section, derived in the same way. As expected, the Coulomb dissoci-

ation cross section is smaller for the 1p channel than for the 2p channel.

Fig. 5.17 shows the added Coulomb excitation spectrum for ^{32}Ar, derived from both reaction channels. A considerable amount of strength can be found in the region of 10 MeV excitation energy.

Table 5.8 summarizes the ^{32}Ar Coulomb dissociation cross sections measured in this thesis.

Table 5.8: The measured Coulomb dissociation cross sections of ^{32}Ar derived from the analysis described in this thesis. Corresponding error sources are described in the text.

	Inclusive measurement	Exclusive measurement
^{32}Ar$(\gamma,\text{p})^{31}$Cl	-	$54(8^{stat})(6^{sys})$ mb
^{32}Ar$(\gamma,2\text{p})^{30}$S	$214(29^{stat})(20^{sys})$ mb	$226(14^{stat})(23^{sys})$ mb
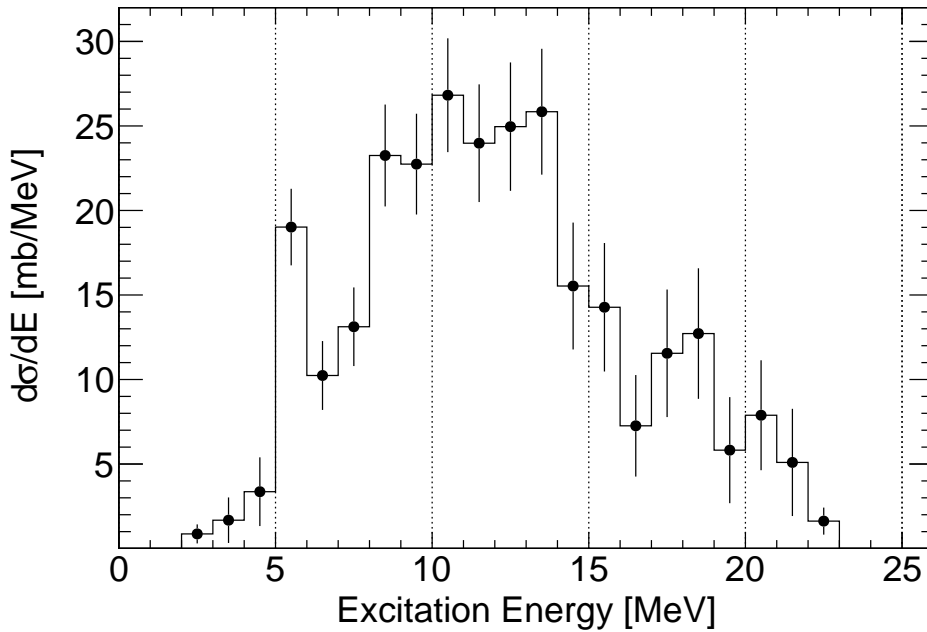
Figure 5.17: The energy-differential Coulomb dissociation cross section including the 1p and 2p channel. All corrections are applied, the γ-sum energy is added in the 2p case.

6
Summary and Outlook

The subject of this thesis is enclosed in the general framework of the upcoming R^{3}B experiment at the FAIR facility at GSI, Darmstadt, and its successfully running predecessor, the ALADIN/LAND setup. It consists of two parts. In the first part, a Coulomb excitation experiment, which was performed in August 2008, is described in detail. The experiment is a continuation of the successfully performed series of Coulomb excitation experiments at the ALADIN/LAND setup. The second part of this thesis is devoted to a detector instrumentation. The detector, called LENA (Low Energy Neutron detector Array) will be used in (p,n)-type reactions in upcoming R^{3}B experiments.

The electromagnetic excitation process allows to study γ-induced reactions in inverse kinematics and can therefore be applied to radioactive nuclei. Besides spectroscopic information about single-particle features, also collective modes, and radiative cross sections can be deduced. Deployed in reactions in inverse kinematics, even highly asymmetric nuclei can be studied, situated in the most exotic regions of the nuclear landscape close to the driplines. In the experiment described in this thesis, a beam consisting of isotopes with similar A/Z ratio, situated around the even-even nucleus ^{32}Ar (A/Z = 1.777), was directed onto a ^{208}Pb target with subsequent electromagnetic excitation and dissociation. These isotopes are of special interest for the astrophysical rapid proton-capture process (rp process). While moving towards heavier elements, the region around ^{32}Ar is on the path, and possibly conceals a waiting point: the ^{30}S(p,γ)^{31}Cl reaction.

The mixed beam also contained ^{31}Cl, and the nuclear structure properties could be studied via the invariant mass method, and the reconstruction of the excitation energy spectrum. In a first step, updated mass measurements were used to derive input parameters for the isobaric multiplet mass equation (IMME), which relates the mass excess to the isospin projection of an isospin multiplet. In this case, the $A = 31$, $\mathcal{T} = 3/2$ isotopes form an isospin quartet. Using the ground state, the first, and second $\mathcal{T} = 3/2$ excited state mass excesses, it is possible to calculate the mass excess of the first excited state of ^{31}Cl. It is at $E_x = 733(6)$ keV ($J^\pi = 1/2^+$). A second excited state is at $E_x = 1746(7)$ keV with $J^\pi = 5/2^+$. However, there exists only one measurement of the excited states performed with β-delayed proton decay.

By extracting the excitation spectrum in this experiment, two resonances can be identified below 2 MeV excitation energy. A first state (which is the first excited state

with $J^\pi = 1/2^+$) is observed at $E_x = 726(37)$ keV, whereas the second state is at $E_x = 1731(82)$ keV. This nicely confirms the IMME calculation. It was possible to extract the partial Coulomb dissociation cross sections for the individual components. For the first excited state, the partial cross section is 15(6) mb. For the second state, it is 30(9) mb.

Subsequently, the measured parameters are used to constrain the astrophysical important ^{30}S(p,γ)^{31}Cl reaction. Mainly the low Q-value of below 300 keV favors this reaction to be a possible candidate for a bottleneck in the rp-process flow. The derived stellar reaction rate is dominated by the resonant capture into the first excited state. The second state, and also a direct capture component is also considered. Finally, the resulting reaction rate is compared to its first calculation done by Woosley and Wallace, and a calculation performed by Iliadis et al., showing severe deviations for temperatures below 0.2 GK.

The next step, which is outside the frame of this thesis, is to incorporate the deduced reaction rate into a full rp-process network calculation, in order to constrain the mass flow of the rp process in this mass region. Moreover, realistic models could be used to investigate, if there is a waiting point established by the ^{30}S(p,γ)^{31}Cl reaction.

For the IMME calculation, significant progress could be achieved by using more than one data set of updated mass measurements, and by incorporating a weighted average for the input parameters.

A measurement with higher statistics and mainly focused on ^{31}Cl could help to minimize the statistical uncertainties, which enter exponentially into the stellar reaction rate. Furthermore, in order to disentangle the M1/E2 contributions to the Coulomb dissociation cross section of the first excited state of ^{31}Cl, the angular distributions of the outgoing particles need to be investigated. The extraction of the contributions from M1/E2 excitation could subsequently be used to calculate the radiative cross section $\sigma_{(p,\gamma)}$, and to derive the corresponding resonance strength, which could be compared to the resonance strengths used here. The M1 component is dominant for the mirror transition in ^{31}Si, and thus, the decomposition could also be used to constrain the appropriate γ-decay width Γ_γ(M1) in ^{31}Cl.

In the next analysis step, the Coulomb dissociation cross section for the ^{32}Ar(γ,2p)^{30}S reaction is extracted with two methods. First, the full proton branch of the setup is discarded. The outgoing particle mass spectra are derived with a special tracking algorithm. A scaling of the pure nuclear contribution to the cross section is extracted. The final mass spectrum exhibit a peak at ^{30}S, which can be used to extract the Coulomb dissociation cross section of 214(29$^{\text{stat}}$)(20$^{\text{sys}}$) mb.

Since the setup is capable of performing exclusive measurements of all outgoing particles, the excitation energy spectrum of ^{32}Ar is reconstructed from the 2p channel. Significant strength is found with a peak around $E_x \approx 10 - 11$ MeV. Integration of the energy-differential spectrum yields a total cross section of 226(14$^{\text{stat}}$)(23$^{\text{sys}}$) mb. This value is in very good agreement with the inclusive measurement, validating the usage of efficiency

and acceptance corrections applied for the proton branch.

The Coulomb dissociation cross section for the 1p channel was also extracted. Therefore, the exclusive measurement was used in a similar way as for the 2p channel. The integrated Coulomb dissociation cross section for the $^{32}\mathrm{Ar}(\gamma,\mathrm{p})^{30}\mathrm{S}$ reaction is $54(8^{\mathrm{stat}})(6^{\mathrm{sys}})$ mb. In order to interpret the energy-differential cross section distributions with respect to the appearance of low-lying dipole strength and the giant-dipole resonance in proton-rich nuclei, a reaction model with an incorporated de-excitation mechanism needs to be employed. Furthermore, the Coulomb dissociation cross sections could be used to investigate a possible circumvention of the waiting point at $^{30}\mathrm{S}$ by 2p captures on $^{30}\mathrm{S}$ via $^{30}\mathrm{S}(2\mathrm{p},\gamma)^{32}\mathrm{Ar}$.

The second part of this thesis is dedicated to the development of the Low Energy Neutron detector Array (LENA), which will be used in (p,n)-type reactions in upcoming R^{3}B experiments. The detector is made of organic solid scintillation material, with two fast photomultiplier tubes optically coupled to both ends. In a first step, basic properties are derived from measurements performed with γ- and X-ray sources. Furthermore, GEANT3 simulations are employed to reproduce the results. They show excellent agreement with the experimental data. In order to study the detector response to neutrons, and moreover, the neutron detection efficiency, an experiment was performed at the Los Alamos National Laboratory. Again, the simulations show good agreement with the experimental data, and, therefore, the simulations could be used to derive the detection efficiency for different thresholds.

A first measurement with a prototype of the detector was performed at the existing ALADIN/LAND setup in October 2011. It could be used to demonstrate the general feasibility of detection of low-energy neutrons with the LENA detector for upcoming experiments at the R^{3}B setup.

7
Zusammenfassung

Das Ziel dieser Arbeit war es, die komplexen Prozesse während eines Röntgenausbruchs auf Neutronensternen besser zu verstehen. Neutronensterne können vor allem wasserstoff- und heliumreiches Material von einem nahen Stern erhalten. Als Folge sehr hohen Gravitationspotentials kommt es dabei zur extremen Erhitzung des Materials. Ab einer gewissen Temperatur setzen Fusionsreaktionen von Protonen und den α Teilchen ein. Je nach Szenario kann dabei der schnelle Protoneneinfangsprozess (rp-Prozess) stattfinden, der Elemente in schnellen Einfangsreaktionen innerhalb von 10 bis 100 Sekunden bis in den Bereich von Tellurium synthetisiert. Im optisch sehr dichten Material der äußeren Schicht des Neutronensterns, wird während dieses Prozesses Röntgenstrahlung erzeugt, die hier auf der Erde mithilfe von Satelliten beobachtet werden kann.

Auf dem Pfad des schnellen Protoneneinfangsprozesses liegen Isotope, deren Kerneigenschaften dazu führen, dass sich der Reaktionsfluss kurze Zeit staut, was sich in der modellierten Lichtkurve widerspiegelt. Diese radioaktiven Isotope haben eine geringe Wechselwirkungswahrscheinlichkeit, was dazu führt, dass sie sich stark anhäufen. Sie sind deshalb Wartepunkte und liegen weit außerhalb des Stabilitätstals, was sie experimentell schwer zugänglich macht.

Ein Wartepunkt im mittleren Massenbereich des Prozesses wird bei der Protoneneinfangsreaktion ^{30}S(p,γ)^{31}Cl erwartet. Diese Reaktion ist durch die nukleare Struktur des ^{31}Cl Isotopes bestimmt, worüber bisher nahezu keine experimentellen Daten vorliegen. Vor allem der geringe Q-Wert der Reaktion von 300 keV und das relativ langlebige ^{30}S Isotop mit einer Halbwertszeit von mehr als einer Sekunde führen zu einem $(p,\gamma) \leftrightarrow (\gamma,p)$ - Gleichgewicht, das in einer erhöhten Häufigkeit von ^{30}S resultiert. Aus diesem Grund ist es von großer Wichtigkeit, diesen Bereich der protonenreichen Kerne genauer zu untersuchen und die Kernstruktur experimentell zu bestimmen.

Die GSI Helmholtzzentrum für Schwerionenforschung GmbH in Darmstadt bietet hervorragende Experimentbedingungen, um die Struktur, Masse, Lebensdauer und Reaktionsquerschnitte der zuvor beschriebenen exotischen Kerne zu untersuchen.

Am ALADIN/LAND-Aufbau werden kinematisch vollständige Experimente in inverser Kinematik durchgeführt. Es können dabei verschiedene Techniken angewendet werden, die unterschiedliche Untersuchungen der Eigenschaften der exotischen Kerne ermöglichen. Von besonderer Bedeutung sind elektromagnetische Anregungsreaktionen, die zu den in-

elastischen Reaktionen gezählt werden. Das Coulombfeld eines schweren Atomkerns, z.B. eines Bleikerns, wird bei relativistischen Energien stark kontrahiert und ein virtueller Photonenaustausch zwischen Kern und Projektil bei genügend großem Stoßparameter induziert. Durch die Theorie der elektromagnetischen Anregung können dann spektroskopische Informationen aus den gemessenen differenziellen Anregungsenergiespektren oder Winkelverteilungen gewonnen werden.

Die vorliegende Arbeit beschäftigt sich in ihrem Hauptteil mit einem Coulombanregungsexperiment, welches im August 2008 am ALADIN/LAND-Experiment durchgeführt wurde. Untersucht wurden dabei protonenreiche, exotische Argonisotope. Hierfür wurde ^{36}Ar auf etwa 825 AMeV beschleunigt und im Fragmentseparator in einer Berylliumfolie fragmentiert. Aus der Vielfalt produzierter Isotope wurden daraufhin die gewünschten exotischen ^{32}Ar und ^{31}Cl Kerne selektiert und zum Experimentierplatz transportiert. Bei einer verbleibenden Strahlenergie von etwa 650 AMeV wurden die radioaktiven Isotope mittels des elektromagnetischen Feldes der Bleikerne im Reaktionsort des Experiments angeregt und alle Zerfallsprodukte im Aufbau detektiert. Mit der Methode der invarianten Masse und der Rekonstruktion des Viererimpulses jedes Teilchens ist es möglich, das differenzielle Anregungsspektrum des einfallenden Teilchens zu bestimmen. Ein-Teilchen-Zustände, wie auch kollektive Moden, können identifiziert und davon entsprechende Parameter abgeleitet werden. Durch Vergleiche mit theoretischen Vorhersagen ist es möglich, Modelle zu verifizieren und zu verbessern.

Experimentell werden hierzu alle Impulse und Teilchenarten anhand der Flugzeiten und Energiedepositionen der Teilchen in einzelnen Detektoren gemessen. Die vollständige Messung in inverser Kinematik erfordert daher einen Aufbau, der sich aus hochauflösenden Detektoren zusammensetzt. Da die einzelnen Detektoren unterschiedliche Anforderungen erfüllen müssen, werden variable Detektortypen eingesetzt. Plastikszintillatoren mit optisch gekoppelten Photoelektronenvervielfachern messen die Flugzeiten, den Energieverlust und die Auftreffposition jedes Teilchens. Da für jede Reaktion alle Trajektorien entlang des Aufbaus rekonstruiert werden, benutzt man neben den Plastikszintillatoren vor allem hochauflösende Siliziumstreifendetektoren und Elektronendriftkammern. Ein 4π γ-Detektor, der um den Reaktionsort herum aufgebaut war, wurde eingesetzt, da die Abregung des Zwischenkerns auch über verschiedene, höher liegende Zustände des Ejektils ablaufen kann.

Um die Coulombaufbruchquerschnitte zu bestimmen, wurde neben einer Bleifolie auch eine Kohlenstoffscheibe im Reaktionspunkt eingesetzt, um die nuklearen Anteile der gemessenen Rate genau zu bestimmen. Der Querschnitt von Coulombanregungsreaktionen ist quadratisch abhängig von der Ladung des Kerns, an dem die Reaktion induziert wird. Da die Kohlenstoffkerne signifikant kleinere Ladung haben als die Bleikerne, kann der Coulombaufbruch am Kohlenstoffkern vernachlässigt werden. Eine Skalierung auf die Querschnittsfläche der Kerne im Tröpfchenmodell erlaubt es, den Anteil des nuklearen Wirkungsquerschnitts mit Blei aus den Messungen mit der Kohlenstoffscheibe zu berechnen. Die aufeinander skalierten Messungen können dann voneinander abgezogen

werden.

Um den Anteil der reagierten Teilchen in verschiedenen Materialen außerhalb des Reaktionspunkts zu bestimmen, wurden entsprechende Untergrundmessungen durchgeführt.

Ein spezieller Algorithmus erlaubt es im weiteren Verlauf der Analyse, die Teilchentrajektorien zu bestimmen. Hierüber ist es möglich, die Viererimpulse und die Massen der produzierten Isotope zu berechnen. Dies erlaubt eine eindeutige Identifikation der einfallenden und reagierten Teilchen, womit der Reaktionskanal vollständig beschrieben werden kann. Die Massenspektren können dann benutzt werden, um den integralen Coulombaufbruchquerschnitt inklusiv zu bestimmen. Die Rekonstruktion der Viererimpulse der Protonen und der schweren Reaktionsprodukte ermöglicht die Erzeugung von energieabhängigen Anregungsspektren.

Unter der Annahme der Isospinsymmetrie in Atomkernen ist es möglich, Spiegelkerne und deren angeregte Zustände zu benutzen, um erste Informationen über mögliche Parameter in ^{31}Cl zu erhalten. Die isobare Massenformel (*Isobaric Multiplet Mass Equation* IMME) mit kürzlich gemessenen Massendaten erlaubt die Bestimmung der Parameter für den ersten angeregten Zustand in ^{31}Cl. Der Grundzustand besteht dabei aus einer $J^\pi = 3/2^+$ Konfiguration, während der erste angeregte Zustand mit $J^\pi = 1/2^+$ und einer Anregungsenergie von 733(6) keV aus der IMME bestimmt wurde. Ein weiterer Zustand bei einer Anregungsenergie von 1746(7) keV mit $J^\pi = 5/2^+$ ist bereits in einem früheren Experiment identifiziert worden.

Mithilfe der Viererimpulse war es auch hier möglich, das Anregungsspektrum von ^{31}Cl zu messen. Hierfür wird der Reaktionskanal ^{31}Cl$(\gamma,p)^{30}$S betrachtet und es werden alle einfallenden und ausgehenden Teilchen bestimmt. Das Anregungsspektrum lässt sich durch eine Superposition von drei einzelnen Gaußschen Glockenkurven sehr gut beschreiben. Zwei Gaußfunktionen beschreiben dabei die zwei tief liegenden Zustände bei 726(37) keV und 1731(82) keV. Dies ist in exzellenter Übereinstimmung mit den theoretisch vorhergesagten Zuständen und stellt deren erste direkte Messung dar. Die Beschreibung des Spektrums erfordert eine weitere Komponente, die den direkten, nicht-resonanten Einfang repräsentiert. Die partiellen Wirkungsquerschnitte für die einzelnen Resonanzen wurden zu 15(6) mb für den ersten und zu 30(9) mb für den zweiten Zustand bestimmt. Der Wirkungsquerschnitt beinhaltet Dipol- und Quadrupolanteile der Anregung im virtuellen Photonenfeld des Bleikerns, da M1 und E2 Übergänge für beide Resonanzen quantenmechanisch erlaubt sind. Aus diesem Grund sollten in einem zukünftigen Schritt die jeweiligen Anteile mithilfe eines Reaktionsmodells berechnet werden. Dementsprechend können dann die M1 und E2 Anteile aus den Wirkungsquerschnitten abgeleitet werden, um z.B. die Resonanzparamter wie die Partialbreite des Gammazerfalls im Kern zu berechnen.

Im nächsten Schritt kann die stellare Reaktionsrate für die Reaktion ^{30}S$(p,\gamma)^{31}$Cl für die typischen rp-Prozesstemperaturen mit den neu bestimmten Parametern berechnet werden. Diese Rate ist dominiert durch den Einfang in den ersten resonanten Zustand

im (^{30}S+p)-System. Anschließend kann diese Rate mit der ersten theoretischen Berechnung von Wallace und Woosley im Jahr 1982 verglichen werden. Es zeigt sich, dass die im Rahmen dieser Arbeit bestimmten Rate gut mit der theoretischen Beschreibung übereinstimmt. Ein Vergleich zu einer aktuelleren Vorhersage von Iliadis et al. aus dem Jahr 2001 weist Abweichungen von bis zu 4 Größenordnungen auf. Dies ist vor allem auf die zu niedrig angenommene Resonanzenergie des ersten angeregten Zustands in ^{31}Cl zurückzuführen, welche die Autoren benutzt haben.

An ^{32}Ar wurden ebenfalls Coulombanregungsreaktionen gemessen. In diesem Fall liegen die Ein- und Zweiprotonenseparationsenergien sehr dicht zusammen ($S_{1p} = 2.4$ MeV und $S_{2p} = 2.7$ MeV). Dies führt zu einer stärkeren Bevölkerung des Emissionskanals mit zwei Protonen. In einem ersten Schritt wird das Massenspektrum der ^{32}Ar(γ,2p)^{30}S Reaktion bestimmt. Es können auch ^{29}S Isotope nachgewiesen werden, die nur durch nukleare Reaktionen an der Bleiprobe entstanden sein können, da die Neutronenseparationsenergie von $S_n \approx 21$ MeV überhalb der im Feld existierenden maximalen virtuellen Photonenenergie liegt. Dieser Anteil kann dazu genutzt werden, den Skalierungsfaktor α_T für den nuklearen Anteil zu ermitteln. Der Vergleich mit einem einfachen radiusskalierten Reaktionsmodell (*black-disk model*) zeigt gute Übereinstimmung von $\alpha_T^{exp} = 1.79(10)$ und $\alpha_T^{theo} = 1.67$. Nach Abzug des mit Kohlenstoff bestimmten nuklearen Untergrunds kann der inklusive Coulombwirkungsquerschnitt berechnet werden. Dabei sind die emittierten Protonen der Reaktion nicht miteinbezogen, um Effizienz- und Akzeptanzeffekte nicht berücksichtigen zu müssen. Als Ergebnis der inklusiven Messung ergibt sich ein Coulombaufbruchquerschnitt von 214(29$^{\text{stat}}$)(20$^{\text{sys}}$) mb. Dabei stammt der größte systematische Fehler in der inklusiven Messung von der Selektionseffizienz für das zu untersuchende Isotop.

Da auch in diesem Fall eine exklusive Messung vorgenommen wurde, kann das Anregungsspektrum von ^{32}Ar aus dem 2p Kanal gewonnen werden. Ein schwacher γ-Übergang in ^{30}S wurde beobachtet und ist entsprechend in den Daten berücksichtigt. Da für die Rekonstruktion auch der Protonenarm des Experimentaufbaus miteinbezogen wird, müssen Detektoreffizienzen und geometrische Akzeptanzen berücksichtigt werden. Der resultierende Coulombwirkungsquerschnitt berechnet sich zu 226(14$^{\text{stat}}$)(23$^{\text{sys}}$) mb. In diesem Fall tragen die Effizienz- und Akzeptanzkorrektur der Protonendetektoren am stärksten zum systematischen Fehler bei. Durch diese Messung wurde gezeigt, dass beide Wirkungsquerschnitte, die durch unterschiedliche Methoden bestimmt wurden, sehr gut innerhalb der Fehler übereinstimmen.

Im Einprotonenemissionskanal von ^{32}Ar kann der Coulombwirkungsquerschnitt lediglich durch die exklusive Messung der Reaktion ^{32}Ar(γ,p)^{31}Cl berechnet werden und ergibt sich zu 54(8$^{\text{stat}}$)(6$^{\text{sys}}$) mb.

Der Ausbau der existierenden GSI Anlage zum internationalen FAIR Beschleunigerkomplex beinhaltet auch eine Erweiterung des ALADIN/LAND Experiments. Das neue Experiment baut auf den gleichen Messprinzipien auf, jedoch werden höhere Statistik,

exotischere Isotope, sowie höhere Strahlenergien erwartet. Das R^{3}B-Experiment (*Reactions with Relativistic Radioactive Beams*) ermöglicht Studien zum Spin-Isospin-Verhalten von radioaktiven Isotopen. Besonders Fermi- und Gamow-Teller-Übergänge sind hierbei wichtig für die nukleare Astrophysik, da die Matrixelemente für die entsprechenden β-Zerfälle berechnet und somit die Halbwertszeiten unter stellaren Bedingungen bestimmt werden können. Zusätzlich werden Spin-Isospin-Resonanzen angeregt, die für die Kernstruktur von wichtiger Bedeutung sind. Die entsprechende Reaktion ist die Ladungstransferreaktion vom Typ (p,n), d.h. es findet ein Austausch von Pionen im Mesonenfeld der nuklearen Wechselwirkung bei größeren Stoßparametern statt. Die gemessenen Wirkungsquerschnitte der (p,n)-Reaktionen sind wiederum proportional zu den entsprechenden Matrixelementen.

In der Reaktion werden bei geringem Impulsübertrag langsame Neutronen im Energiebereich von 0.1 MeV bis 5 MeV emittiert. Die Laborwinkel relativ zum Strahl sind dabei im Bereich von 60° bis 90°. Dies erlaubt die Benutzung von Plastikszintillatoren mit den Dimensionen $1000 \times 45 \times 10$ mm^3, die an beiden Enden mit Photoelektronenverfielfachern ausgestattet sind. Das Szintillationslicht wird dabei von Protonen erzeugt, an welchen das einfallende Neutron elastisch gestreut wurde. Die Neutronenenergie kann durch die Flugzeit des Neutrons vom Reaktionspunkt zum Detektor bestimmt werden. Im Rahmen dieser Arbeit ist die Entwicklung des Neutronendetektorsystems LENA beschrieben. An einem Prototyp des Detektors wurden die grundlegenden Größen wie Lichtgeschwindigkeit im Material, die Dämpfungskonstante, sowie die energieabhängige Nachweiswahrscheinlichkeit gemessen. Weiterhin zeigen detaillierte GEANT3 Simulationen sehr gute Übereinstimmung mit experimentellen Daten.

Die Detektoreffizienz wurde in einem Experiment am Los Alamos National Laboratory mithilfe eines weißen Neutronenspektrums gemessen. In einer ^{235}U Folie wurden dabei Spaltneutronen erzeugt, deren Energiespektrum sehr genau bekannt ist, und die im Abstand von 1 Meter gemessen werden konnten. Die so gewonnene integrale Ansprechwahrscheinlichkeit wird zunächst mithilfe der GEANT3 Simulationen reproduziert. Anschließend ist dann, basierend auf weiteren Simulationen, die Entfaltung und somit die Bestimmung der Effizienz des Detektors für monoenergetische Neutronen möglich.

Die energieabhängige Effizienzkurve wurde dabei für zwei mögliche Detektorpositionierungen simuliert. In einem Fall wurde, innerhalb der Simulation, die schmale Seite des Detektors in Richtung des Reaktionspunkts gedreht, um die Winkelauflösung zu erhöhen. Jedoch wird hierbei die Raumwinkelabdeckung verringert. Im zweiten Fall zeigt die breite Detektorseite in die Richtung des Reaktionspunkts.

Gerade im Bereich von Energien unterhalb von 1 MeV können Neutronen dabei mit guter Nachweiswahrscheinlichkeit detektiert werden. Im Weiteren sollen die eingesetzten Simulationen dafür verwendet werden, um den genauen Aufbau der kombinierten Detektormodule zu bestimmen. Besonderes Augenmerk liegt hier auf der Möglichkeit, dass die Neutronen innerhalb des Detektors in den verschiedenen Detektormodulen gestreut werden. Aus diesem Grund soll ein Gestell aus Aluminium eingesetzt werden, in dem die Detektoren dann je nach Experiment nochmal verfeinert ausgerichtet werden können.

Bibliography

[1] Available online at `http://www.redorbit.com/education/reference_library/space_1/universe/2574798/xray_binaries/`
Last visited on May 4, 2012.

[2] Schatz, H. and Rehm, K. *Nuclear Physics A* **777**(0), 601 – 622 (2006). Special Issue on Nuclear Astrophysics.

[3] Schatz, H., Aprahamian, A., Barnard, V., Bildsten, L., Cumming, A., Ouellette, M., Rauscher, T., Thielemann, F.-K., and Wiescher, M. *Nuclear Physics A* **688**(1–2), 150 – 153 (2001). Nuclei in the Cosmos.

[4] Schatz, H., Aprahamian, A., Barnard, V., Bildsten, L., Cumming, A., Ouellette, M., Rauscher, T., Thielemann, F.-K., and Wiescher, M. *Phys. Rev. Lett.* **86**, 3471–3474 Apr (2001).

[5] Fisker, J. L., Thielemann, F.-K., and Wiescher, M. *The Astrophysical Journal Letters* **608**(1), L61 (2004).

[6] Schatz, H. *Progress in Particle and Nuclear Physics* **66**(2), 277 – 282 (2011). Particle and Nuclear Astrophysics, International Workshop on Nuclear Physics, 32nd Course.

[7] Wapstra, A., Audi, G., and Thibault, C. *Nuclear Physics A* **729**(1), 129 – 336 (2003). The 2003 NUBASE and Atomic Mass Evaluations.

[8] Weizsaecker, C. F. v. *Zeitschrift fuer Physik A Hadrons and Nuclei* **88**, 612–625 (1934). 10.1007/BF01333110.

[9] Williams, E. J. *Phys. Rev.* **45**, 729–730 May (1934).

[10] Fermi, E. *Zeitschrift fuer Physik A Hadrons and Nuclei* **29**, 315–327 (1924). 10.1007/BF03184853.

[11] Bertulani, C. A. and Baur, G. *Physics Reports* **163**(5–6), 299 – 408 (1988).

[12] Baur, G., Bertulani, C., and Rebel, H. *Nuclear Physics A* **458**(1), 188 – 204 (1986).

[13] Available online at `http://www.gsi.de/`
Last visited on May 4, 2012.

[14] Available online at `http://www-inj.gsi.de/`
Last visited on May 4, 2012.

Bibliography

[15] Geissel, H., Armbruster, P., Behr, K., Brünle, A., Burkard, K., Chen, M., Folger, H., Franczak, B., Keller, H., Klepper, O., Langenbeck, B., Nickel, F., Pfeng, E., Pfützner, M., Roeckl, E., Rykaczewski, K., Schall, I., Schardt, D., Scheidenberger, C., Schmidt, K.-H., Schröter, A., Schwab, T., Sümmerer, K., Weber, M., Münzenberg, G., Brohm, T., Clerc, H.-G., Fauerbach, M., Gaimard, J.-J., Grewe, A., Hanelt, E., Knödler, B., Steiner, M., Voss, B., Weckenmann, J., Ziegler, C., Magel, A., Wollnik, H., Dufour, J., Fujita, Y., Vieira, D., and Sherrill, B. *Nuclear Instruments and Methods in Physics Research Section B: Beam Interactions with Materials and Atoms* **70**(1-4), 286 – 297 (1992).

[16] Sümmerer, K. and Blank, B. *Phys. Rev. C* **61**, 034607 Feb (2000).

[17] Available online at `http://www.detectors.saint-gobain.com/uploadedFiles/SGdetectors/Documents/Product_Data_Sheets/BC418-420-422-Data-Sheet.pdf` Last visited on May 4, 2012.

[18] Håkan T. Johansson. *The DAQ always runs.* PhD thesis, Chalmers University of Technology, (2009).

[19] Available online at `http://www-linux.gsi.de/~rplag/land02/` Last visited on May 4, 2012.

[20] Metag, V., Habs, D., Helmer, K., v. Helmolt, U., Heyng, H., Kolb, B., Pelte, D., Schwalm, D., Hennerici, W., Hennrich, H., Himmele, G., Jaeschke, E., Repnow, R., Wahl, W., Simon, R., and Albrecht, R. In *Detectors in Heavy-Ion Reactions*, volume 178 of *Lecture Notes in Physics*, 163–178. Springer Berlin / Heidelberg (1983).

[21] Available online at `http://garfield.web.cern.ch/garfield/` Last visited on May 4, 2012.

[22] Christine Wimmer. Private communication.

[23] Available online at `http://www.srim.org/` Last visited on May 4, 2012.

[24] Cub, J., Stengel, G., Grünschloß, A., Boretzky, K., Aumann, T., Dostal, W., Eberlein, B., Elze, T., Emling, H., Ickert, G., Holeczek, J., Holzmann, R., Kratz, J., Kulessa, R., Leifels, Y., Simon, H., Stelzer, K., Stroth, J., Surowiec, A., and Wajda, E. *Nuclear Instruments and Methods in Physics Research Section A: Accelerators, Spectrometers, Detectors and Associated Equipment* **402**(1), 67 – 74 (1998).

[25] Langer, C., Algora, A., Couture, A., Csatlós, M., Gulyás, J., Heil, M., Krasznahorkay, A., O'Donnell, J., Plag, R., Reifarth, R., Stuhl, L., Sonnabend, K., Tornyi, T., and Tovesson, F. *Nuclear Instruments and Methods in Physics Research Section A: Accelerators, Spectrometers, Detectors and Associated Equipment* **659**(1), 411 – 418 (2011).

[26] Available online at `http://www.gsi.de/forschung/fair_experiments/superfrs/index_e.html`
Last visited on May 4, 2012.

[27] Available online at `http://www.gsi.de/forschung/kp/kr/R3B_e.html`
Last visited on May 4, 2012.

[28] Sasano, M., Perdikakis, G., Zegers, R. G. T., Austin, S. M., Bazin, D., Brown, B. A., Caesar, C., Cole, A. L., Deaven, J. M., Ferrante, N., Guess, C. J., Hitt, G. W., Meharchand, R., Montes, F., Palardy, J., Prinke, A., Riley, L. A., Sakai, H., Scott, M., Stolz, A., Valdez, L., and Yako, K. *Phys. Rev. Lett.* **107**, 202501 Nov (2011).

[29] Available online at `http://www.electrontubes.com/pdf/XP2262.pdf`
Last visited on May 4, 2012.

[30] Available online at `http://sales.hamamatsu.com/en/products/electron-tube-division/detectors/photomultiplier-tubes/part-r2059.php`
Last visited on May 4, 2012.

[31] Available online at `www.eljentechnology.com`
Last visited on May 4, 2012.

[32] Apostolakis, J. Technical report, CERN, GEANT library, (1993). http://wwwinfo.cern.ch/asd/geant/.

[33] Zeitnitz, C. and Gabriel, T. *Nucl. Instr. Meth. A* **349**, 106 (1994).

[34] Cecil, R., Anderson, B., and Madey, R. *Nuclear Instruments and Methods* **161**(3), 439 – 447 (1979).

[35] Available online at `http://lansce.lanl.gov/lujan/images/Lujan_fltpaths.jpg`
Last visited on May 4, 2012.

[36] ENDF-LIBRARY. Technical report, National Nuclear Data Center, On-Line Access: www.nndc.bnl.gov/nndc/endf/; Brookhaven National Laboratory, (2001).

[37] Weick, H., Sørensen, A., Geissel, H., Scheidenberger, C., Attallah, F., Chichkine, V., Elisseev, S., Hausmann, M., Irnich, H., Litvinov, Y., Lommel, B., Maier, M., Matoš, M., Münzenberg, G., Nankov, N., Nickel, F., Schwab, W., Stöhlker, T., Sümmerer, K., and Voss, B. *Nuclear Instruments and Methods in Physics Research Section B: Beam Interactions with Materials and Atoms* **193**(1–4), 1 – 7 (2002).

[38] Available online at `http://www.nndc.bnl.gov/`
Last visited on May 4, 2012.

Bibliography

[39] Axelsson, L., Aysto, J., Borge, M., Fraile, L., Fynbo, H., Honkanen, A., Hornshøj, P., Jokinen, A., Jonson, B., Lipas, P., Martel, I., Mukha, I., Nilsson, T., Nyman, G., Petersen, B., Riisager, K., Smedberg, M., and Tengblad, O. *Nuclear Physics A* **634**(4), 475 – 496 (1998).

[40] P.M. and Endt. *Nuclear Physics A* **521**(0), 1 – 400 (1990).

[41] Milligan, W. *E.P. Wigner in Proceedings of the Robert A. Welch Foundation Conference on Chemical Research, Houston.* s.n., (1957).

[42] Weinberg, S. and Treiman, S. B. *Phys. Rev.* **116**, 465–468 Oct (1959).

[43] Wrede, C., Caggiano, J. A., Clark, J. A., Deibel, C. M., Parikh, A., and Parker, P. D. *Phys. Rev. C* **79**, 045808 Apr (2009).

[44] Antti Saastamoinen. *Studies of $T_z = -\frac{3}{2}$ Nuclei of Astrophysical Interest.* PhD thesis, University of Jyväskylä, (2011).

[45] Kankainen, A., Eronen, T., Gorelov, D., Hakala, J., Jokinen, A., Kolhinen, V. S., Reponen, M., Rissanen, J., Saastamoinen, A., Sonnenschein, V., and Äystö, J. *Phys. Rev. C* **82**, 052501 Nov (2010).

[46] Parikh, A., Wimmer, K., Faestermann, T., Hertenberger, R., José, J., Longland, R., Wirth, H.-F., Bildstein, V., Bishop, S., Chen, A. A., Clark, J. A., Deibel, C. M., Herlitzius, C., Krücken, R., Seiler, D., Straub, K., and Wrede, C. *Phys. Rev. C* **83**, 045806 Apr (2011).

[47] Herndl, H., Görres, J., Wiescher, M., Brown, B. A., and Van Wormer, L. *Phys. Rev. C* **52**, 1078–1094 Aug (1995).

[48] Iliadis, C., D'Auria, J. M., Starrfield, S., Thompson, W. J., and Wiescher, M. *The Astrophysical Journal Supplement Series* **134**(1), 151 (2001).

[49] Dominic M. Rossi. *Investigation of the Dipole Response of Nickel Isotopes in the Presence of a High-Frequency Electromagnetic Field.* PhD thesis, Johannes Gutenberg-Universität Mainz, Germany, (2010).

[50] Y. Togano et al. *Proceedings of "Nuclei in the Cosmos XI (Heidelberg)", 19-23 July 2010, PoS(NIC XI)228* .

[51] Wallace, R. K. and Woosley, S. E. *Astrophysical Journal Supplement Series* **45**, 389–420 February (1981).

[52] Konstanze Boretzky. *Systematische Untersuchungen zur Coulombanregung der Zwei-Phononen-Dipolriesenresonanz in ^{208}Pb.* PhD thesis, Universität Frankfurt am Main, Germany, (1995).

136

[53] Birgit Kindler. Private communication, (2012).

[54] Dominic Rossi and Heiko Scheit. Private communication, (2011).

List of Figures

List of Tables

Acknowledgements

Curriculum Vitae

Personal info

Name:	Christoph Langer
Date of birth:	July 28th, 1981
Place of birth:	Darmstadt, Germany
Citizenship:	German
Marital status:	married to Natascha Langer

Education

1992 - 2001	Edith-Stein-Schule, Darmstadt
2001	Abitur
2001 - 2002	Civilian service at ASB Darmstadt
10/2002 - 06/2007	Ruprecht-Karls-University Heidelberg, Undergraduate student of Physics and Philosophy
06/2007 - 06/2008	Diploma thesis (Grade: very good): *Untersuchungen an ^{6}He und Verbesserungen am ALADiN-LAND Setup* Supervisors: Prof. Dr. Thomas Stöhlker, Dr. Haik Simon, Prof. Dr. Hans Emling
08/2008 - present	PhD student at the Institute of Applied Physics, Goethe-Universität Frankfurt am Main and GSI, Darmstadt Supervisor: Prof. Dr. Rene Reifarth